

AD 663848

AD

**USAAVLABS TECHNICAL REPORT 66-80**

**AN EXPERIMENTAL INVESTIGATION OF THE  
LONGITUDINAL DYNAMIC STABILITY CHARACTERISTICS  
OF A FOUR-PROPELLER TILT-WING VTOL MODEL**

**By**

**H. C. Curtiss, Jr.**

**W. F. Putman**

**J. V. Lebacqz**

**September 1967**

**U. S. ARMY AVIATION MATERIEL LABORATORIES  
FORT EUSTIS, VIRGINIA**

**CONTRACT DA 44-177-AMC-8(T)**

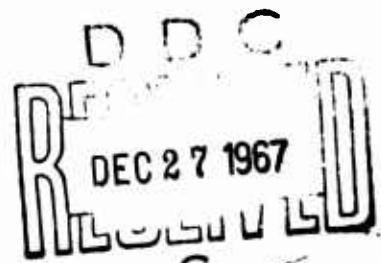
**PRINCETON UNIVERSITY**

**PRINCETON, NEW JERSEY**

*Distribution of this  
document is unlimited*



**CLEARINGHOUSE**  
The text below the clearinghouse logo is small and mostly illegible, but appears to include the words 'The text below the clearinghouse logo is small and mostly illegible, but appears to include the words'.



124

### Disclaimers

When Government drawings, specifications, or other data are used for any purpose other than in connection with a definitely related Government procurement operation, the United States Government thereby incurs no responsibility nor any obligation whatsoever; and the fact that the Government may have formulated, furnished, or in any way supplied the said drawings, specifications, or other data is not to be regarded by implication or otherwise as in any manner licensing the holder or any other person or corporation, or conveying any rights or permission, to manufacture, use, or sell any patented invention that may in any way be related thereto.

Trade names cited in this report do not constitute an official endorsement or approval of the use of such commercial hardware or software.

### Disposition Instructions

Destroy this report when no longer needed. Do not return it to originator.

ADDITIONAL BY	
OPIN	WHITE SECTION <input checked="" type="checkbox"/>
DOO	DIFF SECTION <input type="checkbox"/>
REMARKS	<input type="checkbox"/>
JUSTIFICATION	
BY	
DISTRIBUTION/AVAILABILITY CODES	
DISC.	AVAIL. AND IN SPECIAL
/	



DEPARTMENT OF THE ARMY  
U. S. ARMY AVIATION MATERIEL LABORATORIES  
FORT EUSTIS, VIRGINIA 23604

This report has been reviewed by this Command and is considered to be technically sound. This work, which was performed under Contract DA 44-177-AMC-8(T), was undertaken to determine experimentally the longitudinal dynamic stability characteristics of a four-propeller tilt-wing VTOL transport model tested on the Princeton Dynamic Model Track.

The report is published for the exchange of information and the stimulation of ideas.

Task 1P125901A14233  
Contract DA 44-177-AMC-8(T)  
USAAVLABS Technical Report 66-80  
**September 1967**

AN EXPERIMENTAL INVESTIGATION OF THE  
LONGITUDINAL DYNAMIC STABILITY CHARACTERISTICS  
OF A FOUR-PROPELLER TILT-WING VTOL MODEL

Report No. 774

by

H. C. Curtiss, Jr., W. F. Putman and J. V. Lebacqz

Prepared by

Princeton University  
Department of Aerospace and Mechanical Sciences  
Princeton, New Jersey

for

U. S. ARMY AVIATION MATERIEL LABORATORIES  
FORT EUSTIS, VIRGINIA

Distribution of this  
document is unlimited.

## SUMMARY

The results of experiments conducted to evaluate the longitudinal stability characteristics of a dynamically similar model are presented and discussed. The model simulated a four-propeller tilt-wing VTOL transport at one-tenth scale. The Princeton Dynamic Model Track was used to measure the static stability derivatives and the transient response characteristics of the model in various degrees of freedom. Wing incidences from  $90^\circ$  to  $40^\circ$  were investigated. The results are interpreted in terms of corresponding full-scale aircraft characteristics. Note that all data are presented for a center-of-gravity position of 9-percent MAC which is ahead of the most forward C.G. position of the aircraft (15-percent MAC) and that the horizontal tail and flap program differ from those presently used on the aircraft as shown in Figure 6.

The transient motions at wing incidences between  $90^\circ$  and  $70^\circ$  were similar and were dominated by a high speed stability and a low angular damping, resulting in an unstable oscillation of approximately a 9-second period for the full-scale aircraft. The dynamic motions at wing incidences below  $70^\circ$  were more complex in detail, due to a rapid decrease in the speed stability from a large positive value at wing incidences above  $70^\circ$  to a negative value at  $60^\circ$ . The values of the speed stability  $M_u$  for the aircraft, determined by a detailed analysis of the static and dynamic data in the neighborhood of  $60^\circ$  wing incidence, differ from those obtained from a preliminary analysis of the data by the LTV Aerospace Corporation. Typically, at wing incidences between  $60^\circ$  and  $40^\circ$  the linearized static stability derivatives  $M_u$  and  $M_{\dot{\alpha}}$  were small, and nonlinearities were evident. The small amplitude linearized motion in this wing incidence range was dominated by a divergence. At  $40^\circ$  wing incidence, there were indications that the dynamic motions were tending to become stable.

The general nature of the motions is typical of this type of aircraft at slow flight speeds, since the primary contributions to the stability derivatives arise from wing-slipstream interaction.

## FOREWORD

This research was performed by the Department of Aerospace and Mechanical Sciences, Princeton University, under the sponsorship of the United States Army Aviation Materiel Laboratories Contract DA 44-177-AMC-8(T), with financial support from the United States Navy, Bureau of Weapons, and the Air Force Flight Dynamics Laboratory. The research was monitored by Mr. Richard L. Scharpf of the United States Army Aviation Materiel Laboratories.

The research was conducted by Assistant Professor H. C. Curtiss, Jr., W. F. Putman and J. V. Lebacqz of Princeton University.

**BLANK PAGE**

## CONTENTS

	<u>Page</u>
SUMMARY	iii
FOREWORD	v
LIST OF FIGURES	viii
LIST OF SYMBOLS	xiii
INTRODUCTION	1
DESCRIPTION OF APPARATUS AND EXPERIMENTS	4
EXPERIMENTAL RESULTS	7
DYNAMICS OF THE FULL-SCALE AIRCRAFT	17
CONCLUSIONS	23
RECOMMENDATIONS	24
REFERENCES	25
APPENDIXES	27
I. Analysis of Data	27
II. Notes on Method of Conducting Experiments and Scaling of Data	37
III. Conversion to Full Scale	42
IV. Effect on Center-of-Gravity Position on Static Stability Derivatives	44
DISTRIBUTION	108



## LIST OF FIGURES

<u>Figure</u>		<u>Page</u>
1	Princeton Dynamic Model Track Longitudinal Mount With One-Tenth Scale Dynamically Similar Model	51
2	General Arrangement, One-Tenth Scale XC-142 Model	52
3a	Flap Arrangement	53
3b	Spanwise Location of Krüger Flaps	54
4	Propeller Blade Characteristics, Four Blades	55
5	Propeller Static Thrust Characteristics	56
6	Model and Full-Scale Flap Deflection and Tail Incidence Versus Wing Incidence	57
7a	Static Longitudinal Test Data	58
7b	Static Longitudinal Test Data	59
7c	Static Longitudinal Test Data	60
7d	Static Longitudinal Test Data	61
7e	Static Longitudinal Test Data	62
7f	Static Longitudinal Test Data	63
7g	Static Longitudinal Test Data	64
7h	Static Longitudinal Test Data	65
7i	Static Longitudinal Test Data	66
7j	Static Longitudinal Test Data	67
7k	Static Longitudinal Test Data	68
7l	Static Longitudinal Test Data	69
7m	Static Longitudinal Test Data	70
7n	Static Longitudinal Test Data	71

<u>Figure</u>		<u>Page</u>
7o	Static Longitudinal Test Data	72
7p	Static Longitudinal Test Data	73
7q	Static Longitudinal Test Data	74
8a	Comparison of Scaled Model Trim Conditions With Full-Scale Aircraft	75
8b	Model Trim Conditions From Static Data ( $\theta_f = 0$ , $\alpha_f = 0$ , 9-Percent C.G., Tail Rotor Off, $\delta_f$ and $i_t$ Shown in Figure 6)	76
8c	Unbalanced Model Pitching Moment From Static Data ( $\theta_f = 0$ , $\alpha_f = 0$ , 9-Percent C.G., Tail Rotor Off, $\delta_f$ and $i_t$ Shown in Figure 6)	77
9a	Variation of Horizontal Force With Angle of Attack (Tail Rotor Off, $\beta_{MR} = 17.5^\circ$ , $\Omega_{MR} = 4,000$ RPM, $\delta_f$ and $i_t$ Shown in Figure 6)	78
9b	Variation of Model in Vertical Force With Angle of Attack of Propeller Shaft Near Trim Conditions (Tail Rotor Off, $\beta_{MR} = 17.5^\circ$ , $\Omega_{MR} = 4,000$ RPM, $i_t$ Shown in Figure 6)	79
9c	Variation of Model Pitching Moment With Angle of Attack of Propeller Shaft Near Trim Conditions From Static Data (Tail Rotor Off, $\beta_{MR} = 17.5^\circ$ , $\Omega_{MR} = 4,000$ RPM, $i_t$ Shown in Figure 6)	80
10a	Rate of Change of Forces and Pitching Moment With Fuselage Pitch Angle ( $\sim$ Angle of Attack) From Static Data (Tail Rotor Off, $\beta_{MR} = 17.5^\circ$ , $\Omega_{MR} = 4,000$ RPM, $\delta_f$ and $i_t$ Shown in Figure 6)	81
10b	Rate of Change of Vertical Force With Horizontal Velocity Versus Horizontal Velocity From Static Data (Tail Rotor Off, $\beta_{MR} = 17.5^\circ$ , $\Omega_{MR} = 4,000$ RPM, $\delta_f$ and $i_t$ Shown in Figure 6)	82

<u>Figure</u>		<u>Page</u>
10c	Rate of Change of Horizontal Force With Horizontal Velocity Versus Horizontal Velocity From Static Data (Tail Rotor Off, $\beta_{MR} = 17.5^\circ$ , $\Omega_{MR} = 4,000$ RPM, $\delta_f$ and $i_t$ Shown in Figure 6)	83
10d	Rate of Change of Pitching Moment With Horizontal Velocity Versus Horizontal Velocity From Static Data (Tail Rotor Off, $\beta_{MR} = 17.5^\circ$ , $\Omega_{MR} = 4,000$ RPM, $\delta_f$ and $i_t$ Shown in Figure 6)	84
11	General Nature of Static Stability Derivatives	85
12	Model Transient Self-Excited Response, $i_w = 89^\circ$ , Two Degrees of Freedom ( $\Omega_{MR} = 4,000$ RPM, $\beta_{MR} = 17.4^\circ$ , $i_t = 45^\circ$ , $\delta_f = 0^\circ$ , 9-Percent C.G.)	86
13	Model Transient Self-Excited Response, $i_w = 80^\circ$ , Two Degrees of Freedom ( $\Omega_{MR} = 4,000$ RPM, $\beta_{MR} = 17.4^\circ$ , $i_t = 50^\circ$ , $\delta_f = 0^\circ$ , 9-Percent C.G.)	87
14a	Model Transient Self-Excited Response, $i_w = 70^\circ$ , Two Degrees of Freedom ( $\Omega_{MR} = 4,000$ RPM, $\beta_{MR} = 17.4^\circ$ , $i_t = 50^\circ$ , $\delta_f = 15^\circ$ , 9-Percent C.G.)	88
14b	Model Transient Self-Excited Response, $i_w = 70^\circ$ , Two Degrees of Freedom ( $\Omega_{MR} = 4,000$ RPM, $\beta_{MR} = 17.4^\circ$ , $i_t = 50^\circ$ , $\delta_f = 15^\circ$ , 9-Percent C.G.)	89
15a	Model Transient Self-Excited Response, $i_w = 60^\circ$ , Two Degrees of Freedom ( $\Omega_{MR} = 4,000$ RPM, $\beta_{MR} = 17.4^\circ$ , $i_t = 30^\circ$ , $\delta_f = 32.5^\circ$ , 9-Percent C.G.)	90
15b	Model Transient Self-Excited Response, $i_w = 60^\circ$ , Two Degrees of Freedom ( $\Omega_{MR} = 4,000$ RPM, $\beta_{MR} = 17.4^\circ$ , $i_t = 30^\circ$ , $\delta_f = 32.5^\circ$ , 9-Percent C.G.)	91

<u>Figure</u>		<u>Page</u>
16a	Model Transient Self-Excited Response, $i_w = 50^\circ$ Two Degrees of Freedom, Small Amplitude Motion ( $\Omega_{MR} = 4,000$ RPM, $\beta_{MR} = 14.8^\circ$ , $i_t = 0^\circ$ , $\delta_f = 50^\circ$ , 9-Percent C.G.)	92
16b	Model Transient Self-Excited Response, $i_w = 50^\circ$ , Three Degrees of Freedom ( $\Omega_{MR} = 4,000$ RPM, $\beta_{MR} = 14.8^\circ$ , $i_t = 0^\circ$ , $\delta_f = 50^\circ$ , 9-Percent C.G.)	93
16c	Model Transient Self-Excited Response, $i_w = 50^\circ$ , Two Degrees of Freedom, Large Amplitude Motion ( $\Omega_{MR} = 4,000$ RPM, $\beta_{MR} = 14.8^\circ$ , $i_t = 0^\circ$ , $\delta_f = 50^\circ$ , 9-Percent C.G.)	94
17a	Model Transient Self-Excited Response, $i_w = 40^\circ$ , Two Degrees of Freedom ( $\Omega_{MR} = 4,000$ RPM, $\beta_{MR} = 14.3^\circ$ , $i_t = 0^\circ$ , $\delta_f = 55^\circ$ , 9-Percent C.G.)	95
17b	Model Transient Self-Excited Response, $i_w = 40^\circ$ , Two Degrees of Freedom ( $\Omega_{MR} = 4,000$ RPM, $\beta_{MR} = 14.3^\circ$ , $i_t = 0^\circ$ , $\delta_f = 55^\circ$ , 9-Percent C.G.)	96
17c	Model Transient Self-Excited Response, $i_w = 40^\circ$ , One Degree of Freedom, $V_o = 29$ fps ( $\Omega_{MR} = 4,000$ RPM, $\beta_{MR} = 14.3^\circ$ , $i_t = 0^\circ$ , $\delta_f = 55^\circ$ , 9-Percent C.G.)	97
18	Model Single-Degree-of-Freedom Runs With Springs (9-Percent C.G., $\delta_f$ and $i_t$ Shown in Figure 6)	98
19a	Comparison of Model Static and Analog-Matching Data ( $\Omega_{MR} = 4,000$ RPM, 9-Percent C.G., $\delta_f$ and $i_t$ Shown in Figure 6)	99
19b	Comparison of Model Single-Degree-of-Freedom and Analog-Matching Data ( $\Omega_{MR} = 4,000$ RPM, 9-Percent C.G., $\delta_f$ and $i_t$ Shown in Figure 6)	100
20	Axis Systems	101

<u>Figure</u>		<u>Page</u>
21a	Full-Scale Stability Derivatives for Altitude/Gross Weight Correspondence Given in Figure 22 (9-Percent C.G., $k_y = 10.3$ ft, $\delta_f$ and $i_t$ Shown in Figure 6, See Table III for Scaling)	102
21b	Full-Scale Stability Derivatives for Altitude/Gross Weight Correspondence Given in Figure 22 (9-Percent C.G., $k_y = 10.3$ ft, $\delta_f$ and $i_t$ Shown in Figure 6, See Table III for Scaling)	103
21c	Full-Scale Stability Derivatives for Altitude/Gross Weight Correspondence Given in Figure 22 (9-Percent C.G., $k_y = 10.3$ ft, $\delta_f$ and $i_t$ Shown in Figure 6, See Table III for Scaling)	104
21d	Full-Scale Stability Derivatives for Altitude/Gross Weight Correspondence Given in Figure 22 (9-Percent C.G., $k_y = 10.3$ ft, $\delta_f$ and $i_t$ Shown in Figure 6, See Table III for Scaling)	105
22	Density Altitude/Gross Weight Correspondence for Stability Derivatives	106
23	Space-Fixed Axis System	107

# LIST OF SYMBOLS

A	propeller disc area, square feet
A <sub>n</sub>	amplitude of peak of nth cycle of oscillation
c	propeller blade chord, feet
C <sub>T</sub>	propeller thrust coefficient, $\frac{T}{\rho \pi R^2 (\Omega R)^2}$
C <sub>T,s</sub>	propeller thrust coefficient based on slipstream velocity, $\frac{\frac{T}{\pi R^2}}{q + \frac{T}{\pi R^2}}$
C <sub>x</sub> , C <sub>z</sub> , C' <sub>x</sub> , C' <sub>z</sub>	aerodynamic force coefficients defined in Appendix II
g	acceleration of gravity, feet per second squared
GW	gross weight of aircraft, pounds
i <sub>t</sub>	tail incidence angle, degrees
i <sub>w</sub>	wing incidence from fuselage reference, degrees
I <sub>y</sub>	moment of inertia in pitch, slug-feet squared
k <sub>y</sub>	radius of gyration, feet (10.3 feet, full scale)
K <sub>θ</sub>	mechanical spring constant, foot-pounds per radian
l	distance of model center of gravity above model pivot point, inches
M	pitching moment, positive nose up, foot-pounds (aerodynamic data presented about 9-percent MAC)
MAC	mean aerodynamic chord of wing, feet (8.08 feet, full scale)
m <sub>1</sub> , m <sub>2</sub>	model mount linkage masses, slugs

P	period of oscillation, seconds
q	free-stream dynamic pressure, pounds per square foot
R	propeller radius, feet
Re	Reynolds number
S	wing area, square feet (534 square feet, full scale)
s	root of characteristic equation, per second
T	propeller thrust, pounds
t	propeller blade thickness, feet
u	horizontal velocity perturbation, feet per second, positive forward
V	horizontal velocity, feet per second
w	vertical velocity perturbation, feet per second, positive downward
X	horizontal force, positive forward, parallel to free stream at forward speed and to horizon in hover, pounds
$X_u, Z_u,$ $M_u, M_\alpha,$ $M_\theta, M_\alpha$	stability derivatives, rate of change of force or moment with variable indicated in subscript divided by mass or moment of inertia
Z	vertical force, positive downward, perpendicular to free stream at forward speed and to horizon in hover, pounds
$\alpha_f$	angle of attack of fuselage, positive nose up, radians
$\beta$	propeller blade angle, degrees or radians
$\delta_f$	flap deflection, degrees
$\theta$	pitch angle of fuselage, positive nose up, radians
$\lambda_L$	linear scale factor = $\frac{\text{full-scale linear dimension}}{\text{model linear dimension}}$
$\lambda_v$	velocity scale factor = $\frac{\text{velocity of full-scale aircraft}}{\text{velocity of model}}$

$\mu$	propeller advance ratio, $\frac{V}{\Omega R}$
$\rho$	air density, slugs per cubic foot
$\sigma$	air density ratio
$\Lambda_w$	gross weight scale factor = $\frac{\text{desired gross weight}}{\text{gross weight determined on basis of dynamic scaling}}$
$\Omega$	propeller rotational speed, radians per second unless otherwise specified
$\frac{\partial X}{\partial u}, \frac{\partial Z}{\partial w}$	
$\frac{\partial X}{\partial w}, \frac{\partial Z}{\partial u}$	stability derivatives, rate of change of force or moment with variable indicated in subscript
$\frac{\partial M}{\partial w}, \frac{\partial M}{\partial u}$	
$(\dot{\phantom{x}})$	differentiation with respect to time
$(\phantom{x})_c$	full-scale parameter determined by dynamic scaling laws
$(\phantom{x})_D$	full-scale parameter at selected gross weight
$(\phantom{x})_r$	with respect to space-fixed axis
$(\phantom{x})_{rs}$	full-scale parameter
$(\phantom{x})_M$	model parameter
$(\phantom{x})_{MR}$	main rotor
$(\phantom{x})_0$	trim or initial value
$(\phantom{x})_s$	with respect to propeller shaft



**BLANK PAGE**

## INTRODUCTION

A series of experiments to determine the dynamic stability characteristics of a four-propeller tilt-wing transport aircraft were conducted in the Princeton Dynamic Model Track using a one-tenth scale model. This report pertains to the longitudinal dynamics at high wing incidence.

Lateral-directional studies of this configuration are reported in Reference 1, and the theoretical prediction of the characteristics of approximately the same aircraft is given in Reference 2. A comparison of the stability derivatives of this vehicle with two other tilt-wing aircraft may be found in Reference 3. Additional experimental data on the same vehicle are presented in References 4 and 5. Static stability derivatives at lower wing incidences are contained in Reference 5, and some qualitative measurements of the transient response are given in Reference 4.

The experiments conducted to evaluate the stability characteristics of a model using the Princeton Dynamic Model Track fall into two categories. The first is similar to wind tunnel testing, and the data that result are referred to in the following as static data. Total forces and moments acting on the model as a function of flight condition were measured. Since the primary aim of the experiments was to obtain information on the stability of the vehicle, emphasis was placed on the force and moment variations about level, unaccelerated flight. The second category consisted of direct measurements of the transient response of the model by using a servo controlled tracking carriage. The model employed in this study was dynamically similar to a full-scale vehicle. The carriage permits semifree flight of the model in selected degrees of freedom and is described in detail in References 6 and 7. The data resulting from the latter experiments are referred to as dynamic data and are similar in nature to flight test data.

The nature of the linearized small perturbation motions of the vehicle is considered to be of primary interest. In measuring the transient response of a system that is dynamically unstable for small amplitude motions, the occurrence of large amplitude motions is inevitable, and consequently nonlinear phenomena may arise. It is believed, however, that the linear, small perturbation motion is directly concerned with both the piloting task and the design of stabilization equipment, and therefore most of the discussion in the following is related to the small amplitude motion. Nonetheless, further consideration of the nonlinearities is considered necessary.

Nonlinearities are evident in some of the flight conditions of interest here because the important linear terms are very small. This is probably typical of tilt-wing aircraft at intermediate wing incidences. For example, it has been shown previously (Reference 8) that the angle-of-attack stability tends to be positive at low speeds and then becomes zero and

negative as wing incidence is reduced. In the region where the linear variation of pitching moment with angle of attack is near zero, nonlinearities become more prominent.

To verify the equations of motion assumed, and to correlate the static and dynamic data, an analog matching technique was used. That is, the statically measured stability derivatives and the angular damping measured from single-degree-of-freedom experiments were placed in linearized small perturbation equations. The resulting computer solution was compared to the measured transient response. Usually only small adjustments were necessary to make the solutions agree, thus verifying that the important stability derivatives had been measured properly and that the small amplitude motions of the model were approximately linear. These results are discussed in Appendix I.

The four-propeller tilt-wing transport model is a one-tenth scale dynamic model of the LTV XC-142, based on full-scale aircraft characteristics given in Reference 17. The general arrangement of the model is shown in Figure 2. Details of the flap geometry are given in Figure 3, and the propeller blade characteristics are shown in Figure 4. The model differs in the following respects from the present configuration of the XC-142A described in Reference 18.

- a. Krüger flaps, as shown in Figure 3, were installed on the model. The leading edge slats presently in use were not installed on the model.
- b. All experiments were conducted at a center-of-gravity position of 9-percent MAC, ahead of the most forward center-of-gravity position of the aircraft (15-percent MAC).
- c. The inboard and outboard propeller thrust lines are parallel on the model. The inboard thrust line of the XC-142A is located at a negative incidence of  $2^{\circ}6'$  with respect to the outboard thrust line.
- d. The wing airfoil section of the XC-142A is a NASA 63-318 with a modified trailing edge. The model airfoil section is an unmodified NASA 63-318.
- e. The horizontal tail incidence and flap deflection with wing incidence differ from that presently in use on the aircraft, as shown in Figure 6.

These differences originate from the fact that model design and construction was concurrent with that of the full-scale aircraft.

Only limited comparison of model data with flight test is possible at this time. A wing incidence versus trim speed comparison is shown in Figure 8a. The model exhibits somewhat higher equivalent full-scale trim speeds than

the aircraft. The primary model configuration difference of those described above, that may influence the trim speed, is the absence of leading edge slats. Leading edge slats will promote improved flow conditions over the wing at low speeds, and therefore, would be expected to reduce the model trim speeds. With respect to this comparison, it should also be noted that the airspeed measuring system on the full-scale aircraft has not been calibrated at low speeds (Reference 19).

Two assumptions made in the analysis and interpretation of data that follows should be noted. The first is that the dynamic motions of the model may be analyzed on a linearized basis. In certain flight conditions, specifically at wing incidences of  $60^\circ$  and  $40^\circ$ , to predict the motions of the model at any appreciable amplitudes, it is necessary to consider non-linear aspects of the motions. The second assumption is related to interpretation of model data in terms of full-scale aircraft characteristics. All data are presented in dimensional form. In addition to assuming the absence of scale effects, to interpret the model data in terms of a specific gross weight full-scale aircraft at sea level, it is necessary to assume that propeller blade angle and RPM are interchangeable, as discussed in Appendix II. This assumption is not necessary if the data are interpreted in terms of a density altitude corresponding to the gross weight of interest for each model test condition, as shown in Figure 22.

## DESCRIPTION OF APPARATUS AND EXPERIMENTS

### TEST FACILITY

The Princeton University Dynamic Model Track is a facility designed expressly for the study of the dynamic motions of helicopter and VTOL models at equivalent flight speeds of up to 60 knots (for a one-tenth scale model). Basic components of the facility include a servo-driven carriage riding on a track 750 feet long, located in a building of cross section 30 by 30 feet; the carriage has an acceleration potential of 0.6g and a maximum speed of 40 feet per second. A detailed description of the facility and the testing techniques employed may be found in References 6, 7, and 9.

A model may be attached to the carriage by one of several booms. The mount used to conduct longitudinal investigations is shown in Figure 1. This mount permits relative displacements of the model with respect to the carriage in horizontal and vertical directions, as well as allows it to rotate in the plane determined by these two directions. Horizontal relative motion of the model with respect to the carriage is sensed and used to command the carriage to follow the model in a closed-loop fashion. Similarly, vertical displacement of the model with respect to the carriage commands the boom to move vertically. This servo operation of the carriage allows the model to fly "free", with no restraints on the dynamic motions being investigated. This method of testing may be considered similar to dynamic flight testing, but considerably more control over the experiment is possible.

The dynamic tests conducted for this program were for the most part two-degree-of-freedom motions. The pitch angle and the horizontal velocity of the model were allowed to vary, but vertical motion was restrained. That is, the flight path angle was constrained to be zero throughout the motion. This restriction to two-degree-of-freedom motions was necessary since there was not sufficient installed power to produce a vertical aerodynamic force equal to the weight of the model at wing incidences above  $50^\circ$ . This two-degree-of-freedom motion represents the significant coupling at low speeds. The resulting motion can be analyzed to predict the complete longitudinal three-degree-of-freedom motion of the aircraft.

In addition to the dynamic testing as described above, testing to determine the static stability derivatives is conducted by programming carriage movement in accordance with pre-selected velocity profiles at constant angles of attack. Programmed angle-of-attack changes at constant velocity are also possible. The model is rigidly mounted on the carriage, and forces and moments acting on the model are measured with strain gauges. Although this type of testing is similar to wind tunnel testing, this facility offers a 30-by-30-foot test section with a uniform air velocity, free from turbulence. Precise speed control over a range of speeds from backward flight through hover to forward flight is available. This

technique is called quasi-steady state testing.

### MODEL

A three-view drawing of the model constructed for these experiments is shown in Figure 2, and its pertinent dimensions are given in Table I. The model was based on the full-scale aircraft configuration given in Reference 17.

The fuselage is constructed of an inner and outer Fiberglas skin, vacuum molded and bonded to a Styrofoam core. An aluminum box spar is the main structural member of the wing. Mahogany ribs and a vacuum-molded Fiberglas wing surface form the external airfoil shape. The double-slotted flaps are constructed of low density Styrofoam with a Fiberglas covering.

The model drive motor is a 200-volt, 400-cycle, 3-phase electric motor, rated at 5 horsepower, mounted on a bulkhead in the fuselage. Power for the four propellers is transmitted to a central transmission and from thence to right-angle gearboxes located in the wing by flexible shafting. A separate power takeoff is used to drive the tail rotor. Propeller gearboxes and housings are mounted directly on the wing spar. The propeller blades were constructed of Fiberglas by the Hamilton Standard Division of the United Aircraft Corporation. The geometric characteristics of the propellers are shown in Figure 4. The static thrust characteristics of the propellers are given in Figure 5.

Model control positions are set from a control console on the carriage. The model incorporates electrically controllable blade angles on each of the four propellers. The blade angle of the tail rotor is also variable to provide pitching moment trim. Wing incidence, flaps, ailerons, and the horizontal tail are also power operated so that transition runs may be with selected programming of all required controls. All of these systems are closed-loop position controls.

The complexity of the model, due to the components required for control and such details as double-slotted flaps, made meeting the scaling requirements on model weight difficult. A comparison of scaled model characteristics with desired full-scale values is shown in Table I. The corrections necessary to account for these differences on the full-scale vehicle are discussed in later sections. Dynamic model scaling relationships may be found in References 7 and 9, and the resulting model/full-scale relationships are given in Table II.

### DATA RECORDING

All data are transmitted via a telemetering system from the moving carriage to a ground station located in a control room near the track. Data transducers provide signals to a telemeter transmitter mounted on the carriage. The telemetering system provides 20 samples of data per channel per second, with a maximum of 43 channels available. Real time monitoring of all data

quantities is provided by a monitor scope in the telemeter ground station; the data are presented on multi-channel Sanborn recorders and/or X-Y plotters and are simultaneously recorded on an Ampex model 309 tape recorder.

#### ANALOG COMPUTER

Matching of the dynamic model data was conducted on a Goodyear Aircraft Corporation Geda GN215-L3 electronic analog computer. The output of the computer was recorded on a Sanborn multi-channel recorder.

## EXPERIMENTAL RESULTS

This section contains a discussion of the experimental data and the general nature of the results. The techniques used to analyze and interpret the data and the results of the analysis are considered in detail in Appendix I. To minimize the presence of various conversion factors, all discussion in this section is given in terms of model parameters. Then, in the following section, corresponding full-scale results are presented on the basis of scaling laws described in Appendix II.

### STATIC DATA

Measurements of vertical force (perpendicular to the free stream), horizontal force (parallel to the free stream), and pitching moment acting on the model near trim conditions ( $X = 0$ ) were made to determine the static stability derivatives of this vehicle at various wing incidences. The flap deflection and tail incidence setting are given as functions of wing incidence in Figure 6.

The data in this section are presented in dimensional form in terms of forces and moments measured on the model at model velocities. Dimensional presentation of the data was selected for reasons discussed in Appendix II.

The measurements for the static stability derivatives were made as discussed previously. Fuselage angle of attack, propeller blade angle, and propeller RPM were held constant, and the carriage was programmed for a very small acceleration ( $\approx 0.01g$ ) such that the velocity of the model was varied about a trim condition ( $X = 0$ ). This velocity program was conducted at three fuselage angles of attack ( $\alpha = 0$ ,  $\alpha \approx +15^\circ$ ,  $\alpha \approx -15^\circ$ ), one propeller rotational speed (4000 RPM), and one blade angle ( $17.5^\circ$ ) setting. At a wing incidence of  $40^\circ$ , some data were taken at two other blade angle settings.

Although, in principle, the velocity of the model should be steady for each datum point around the trim condition to determine the static stability derivatives, previous experience has shown that the technique of quasi-steady state testing - that is, programming the carriage for very small accelerations - yields data that are identical to those obtained with point-by-point measurements at constant velocity. The quasi-steady technique results in a considerable reduction in testing time, and is valid as long as the carriage accelerations involved are small.

Evaluation of the variation of forces and moments with velocity to determine the stability derivatives  $X_u$ ,  $Z_u$ , and  $M_u$  was emphasized in the static measurements, since they are of major importance at low speeds. There are little published data on these derivatives at low speeds. The other three static derivatives are presented as angle-of-attack derivatives, rather than vertical velocity derivatives, since this corresponds to



the manner in which the experiments were conducted. The angle-of-attack derivatives can be converted to vertical velocity derivatives by dividing by the forward velocity. An indication of the value of the vertical velocity derivatives in hovering may be obtained by noting the rate of change of the angle-of-attack derivatives with forward speed near hover. That is,

$$\frac{\partial(\quad)}{\partial w} = \lim_{V \rightarrow 0} \frac{d}{du} \left( \frac{\partial(\quad)}{\partial \alpha} \right).$$

The static data are presented in Figure 7. The trim characteristics of the model are shown in Figure 8. Cross-plots of the data at trim conditions, to determine the variation of the forces and pitching moment with angle of attack, are shown in Figure 9.

It is assumed that the static stability derivatives are relatively unaffected by the aerodynamic device employed to trim the pitching moment of the aircraft. In general, this assumption must be verified by experimental results since the aerodynamic characteristics of the trimming device may influence the stability derivatives of the vehicle. For example, the speed stability,  $M_u$ , is dependent upon the variation with forward velocity of control-device lift, and since this variation for the tail rotor will, in general, be different from that for the horizontal tail as it will be a function of the trim lift coefficient of each device, the speed stability will depend on which of these devices is being used for trim. However, as discussed below, the experimental data indicates that this assumption is valid for this configuration.

The static measurements were conducted without the tail rotor operating. Any variations in the stability derivatives due to tail rotor thrust would appear when comparing the static derivatives with those obtained from the analysis of the dynamic data. Since there was good agreement between the statically measured derivatives with the tail rotor not operating and the derivatives obtained from a match of the dynamic data in which the tail rotor was used to trim the pitching moment, indications are that the tail rotor contributions are small.

The stability derivatives, found by measuring slopes from these data, are given in Figures 9 and 10. Trim level flight values are indicated by darkened points. When the derivative was reasonably constant, i.e., the variation of the force or moment was approximately linear with the variable of interest, a single point is indicated. When there were significant variations in slope over the range investigated, the variation is shown by a dotted line on the figures.

It should be noted that the velocity derivatives ( $X_u$ ,  $Z_u$ ,  $M_u$ ) are functions of angle of attack. In particular, the rate of change of vertical force with velocity was quite nonlinear and very sensitive to angle of attack. The rate of change of pitching moment and horizontal force with velocity were somewhat less sensitive to angle of attack. These latter

two derivatives also exhibit a nonlinearity at a wing incidence of  $70^\circ$ , decreasing markedly with increasing velocity.

For the angle-of-attack derivatives, the range of slopes, in the case of severe nonlinearities, is indicated by nose-up and nose-down points. The horizontal force varied in an approximately linear fashion with angle of attack. The pitching moment variation with angle of attack was small and linear at the higher wing incidences and quite nonlinear at a wing incidence of  $40^\circ$ . The vertical force variation with angle of attack was, in general, nonlinear, probably due to the presence of separated flow over the wing at high angle of attack.

The most unusual phenomenon appearing in the data was the large hysteresis loop in the force and moment measurements near hover (Figure 7). Motion pictures taken of tufts located on the upper surface of the wing indicated that this hysteresis arises from random flow separation and reattachment over the upper surface of the wing and is mainly concentrated on the section of the wing between the fuselage and the inboard nacelle. The magnitude of the hysteresis loop decreased with forward speed and is not noticeable at wing incidences below  $70^\circ$ . If forces and moments are measured at constant velocities in this speed range, a slow "wandering" of the forces and moments will occur between the limits indicated by the hysteresis loop measured from quasi-steady state testing. This aerodynamic behavior is very similar to phenomena discussed in Reference 10 with respect to the forces acting on a wing above the angle of attack at which stall occurs. It is difficult to estimate how this phenomenon might appear on the full-scale aircraft due to the difference in Reynolds number.

No direct comparison with the static data presented in Reference 4 has been made, as the majority of the data presented there are at lower wing incidences. The data presented on the angle-of-attack stability at high thrust coefficients are similar to those measured here. Note that the moment center for the measurements presented in Reference 5 is at 24.5-percent MAC, and the thrust axis location is slightly different than that of the model in Reference 4 and the model considered in this report.

#### GENERAL NATURE OF PITCHING MOMENT DERIVATIVES

The major contributions to the forces and moments acting on the aircraft are due to the propeller-wing combination, and the fuselage and tail effects are small at the low forward speeds under consideration due to the comparative magnitudes of the dynamic pressures. With the wing at a high angle of incidence, the wing aerodynamic center is above the center of gravity of the vehicle. The change in effective angle of attack of the wing arising from an increase in forward speed produces an increase in the resultant force on the wing, which results in an increase in the horizontal force and a nose-up moment if the wing is not stalled.

As the wing incidence is decreased, the same increment in forward speed will result in a correspondingly smaller effective angle-of-attack change, and thus a smaller horizontal force variation with speed. In addition, the moment arm of the aerodynamic center above the center of gravity will be reduced. Both these effects reduce the pitching moment variation with speed, which will be as shown in Figure 11. As the speed is increased further and the thrust is reduced (the slipstream dynamic pressure is reduced), the effective angle of attack increases and the wing eventually stalls, resulting in a reversal in the pitching moment variation with speed. Deflecting a flap does not affect the slope of the pitching moment, if the wing is not stalled, and primarily shifts the pitching moment curves. Deflecting the flap delays the stall, and the change in the slope of the pitching moment with velocity occurs at a higher free-stream velocity (i.e., higher wing effective angle of attack).

These trends then imply that at forward speeds, below wing stall, the wing immersed in the slipstream contributes to a positive speed stability ( $M_u$ ) and an instability with angle of attack ( $M_\alpha > 0$ ). At forward speeds where the effective angle of attack becomes large enough such that the wing is stalled, the trends reverse, implying a negative speed stability and a nonlinear or possibly stable variation of pitching moment with angle of attack ( $M_\alpha < 0$ ).

It is interesting to note how the values of the two static derivatives are linked together. A favorable trend (in a static sense) in one is linked to an unfavorable trend in the other. It has been assumed that the primary contribution to the shape of the pitching moment curves originates from the resultant force acting on the wing at the aerodynamic center of the wing. In this case, when the wing is not stalled, both  $M_u$  and  $M_\alpha$  will be positive, and when the wing is stalled,  $M_\alpha$  and  $M_u$  will tend to be negative.

At the lower wing incidences and higher speeds, the lift on the horizontal tail becomes important. If the tail incidence and downwash angle are such that the tail produces an upward lift, then the reversal trend of these curves will be accentuated, resulting in a greater negative value of the speed stability. Also, an increase in the static stability with angle of attack is contributed by the horizontal tail, independent of tail incidence, and the two derivatives become somewhat independent.

Indicated on Figure 11 is the region in which each of the wing incidences investigated falls. For clarity, this sketch is shown for no flap deflection.

#### DYNAMIC RESPONSE DATA

Using the carriage in the servo following mode, transient response measurements were made of the model at various wing incidences and flap settings.

As discussed previously, installed power was insufficient at the highest wing incidence settings, so only two-degree-of-freedom experiments ( $\theta = \alpha$ ) were conducted at wing incidences above  $50^\circ$ . However, these two-degree-of-freedom data can be analyzed to determine the stability derivatives of the vehicle and to predict the resulting three-degree-of-freedom motion of the full-scale vehicle. As shown later, in this speed range, there are comparatively small differences in the unstable mode in two and three degrees of freedom at low speeds.

Typical model responses at various wing incidences are shown in Figures 12 through 17.

For the transient measurements, no predetermined input was applied, and the model was allowed to excite itself. The response typically commences within 2 seconds after release of the model. Since the model was unstable, many of these responses exhibit rather large amplitude motions, and some nonlinear behavior is evident.

In addition to these two- and three-degree-of-freedom runs, single-degree-of-freedom motions were measured ( $u = 0, \theta_f = \alpha_f$ ) to determine the

angular damping of the vehicle. Because of the fact that the model had a small and usually positive angle-of-attack stability, and since it is difficult to determine to any degree of accuracy the parameters of a response that is nonoscillatory, mechanical springs were added to provide a restoring moment such that an oscillatory motion would occur in one degree of freedom. Typical runs to determine angular damping are shown in Figure 18. In all cases, as may be noted from these data, the angular damping is small. Precisely, the damping of this motion is determined by the sum of the two stability derivatives  $M_{\dot{\theta}}$  and  $M_{\dot{\alpha}}$ . In this series of experiments it was not possible to separate these two derivatives, so it is assumed that  $M_{\dot{\alpha}} = 0$ . Generally, the sum of these two derivatives was small, so this assumption should not have a significant effect on the results.

Qualitatively, the following dynamic behavior of the model was noted from the transient response data. Recall that all data are presented in model scale, so the time scale should be multiplied by the square root of 10 to estimate the corresponding full-scale motion.

$i_w = 89^\circ, 80^\circ$ . Typical self-excited transient responses at these two wing incidences are shown in Figures 12 and 13. The transient motion of the model is approximately the same at both of these flight conditions and is dominated by an unstable oscillation similar to that characteristic of a helicopter near hovering flight (Reference 11). The speed stability ( $M_u$ ) is large, and the angular damping ( $M_{\dot{\theta}}$ ) is small, so that the period of the unstable motion is considerably shorter than would be expected for a helicopter of similar size. The static data and character of the transient

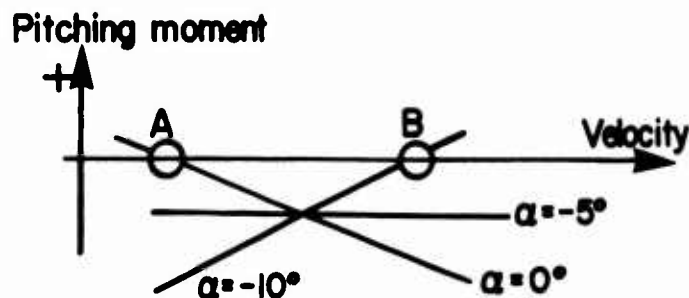
motions indicated that a linearized description of the motions should be valid. The hysteresis loop in the force and moment measurements (Figure 7) did not appear to have any important effect on the transient motion, although it may be the reason for the difference between  $M_u$  measured by strain gauges and the value required to match the transient data (see Appendix I). The reasonably large linear variation of pitching moment with horizontal velocity apparently masks any nonlinear effects and produces an unstable oscillation characteristic of propeller- and rotor-driven vehicles near hovering.

$i_w = 70^\circ$ . At a wing incidence of  $70^\circ$ , there was a difference in the character of the transient motion of the model, depending upon whether the initial angular motion was nose up or nose down (Figure 14). For initial nose-up rotation, an unstable oscillation similar to that at  $80^\circ$  and  $89^\circ$  incidence occurred (Figure 14a). As a result of initial nose-down rotation, the transient motion is essentially divergent (Figure 14b). This nonlinear behavior is due to the stability derivatives  $M_u$  and  $X_u$  decreasing markedly with increasing velocity (see dotted lines in Figure 10). In fact, as the velocity is increased sufficiently from trim,  $M_u$  decreases to zero and changes sign, becoming negative. The model response following initial nose-up motion generally occurs at an average velocity below trim, resulting in a roughly constant value of  $M_u$ , while nose-down motion takes place at velocities above trim, causing a decrease and eventually a change in sign of  $M_u$ .

$i_w = 60^\circ$ . At a wing incidence of  $60^\circ$ , the initial small amplitude motion was divergent (Figure 15). When the initial motion was nose up, the model diverged to its angular limits (Figure 15a). However, when the initial disturbance was nose down, the resulting speed increase due to nose-down motion caused a considerable change in the static stability derivatives. The transient motion becomes a lightly damped oscillation occurring about a nose-down attitude at considerably increased flight velocity (Figure 15b). Nonlinearities become more evident in this flight condition because of the small magnitudes of the linearized static derivatives at the trim condition. In addition, the small amplitude instability produces large amplitude motions.

The behavior of the large amplitude motion that appears as a result of initial nose-down motion may be explained physically on a piecewise linear basis. When nonlinearities are present in the pitching moment curves, multiple equilibrium conditions are possible. That is, moment equilibrium for the model occurs at the initial trim condition ( $\theta_f = 0$ ,  $V_0 = 20$  fps) and also at a nose-down attitude and increased speed ( $\theta_f = -10^\circ$ ,  $V_0 = 28$  fps). A simple explanation of the existence of multiple equilibrium points can be obtained by assuming that the derivative  $M_u$  is a function of angle of attack, tending to become more positive as the angle

of attack is decreased, and that the derivative  $M_\alpha$  is a function of velocity, tending to become negative as the speed is increased. These are the tendencies shown by the static data (as discussed earlier) when the wing is partially stalled. Or, in other words, the nonlinear response can be explained by the existence of one second-order derivative,  $\frac{\partial^2 M}{\partial \alpha \partial u}$ , which would be negative for the trends indicated. The pitching moment curves in this region, which may be obtained by extrapolation of the static data (Figure 7), would appear as follows:



Points A and B on this sketch are the two moment equilibrium points. Point A corresponds to initial trim in which the model is dynamically unstable in a linearized sense, and point B corresponds to another equilibrium condition in which the model is dynamically stable in a linearized sense. The existence of point B as a trimmed flight condition also requires that the horizontal force be zero at this point. Force measurements indicate that at this nose-down attitude and increased speed, the horizontal force would be zero, as it is in level attitude trim at point A.

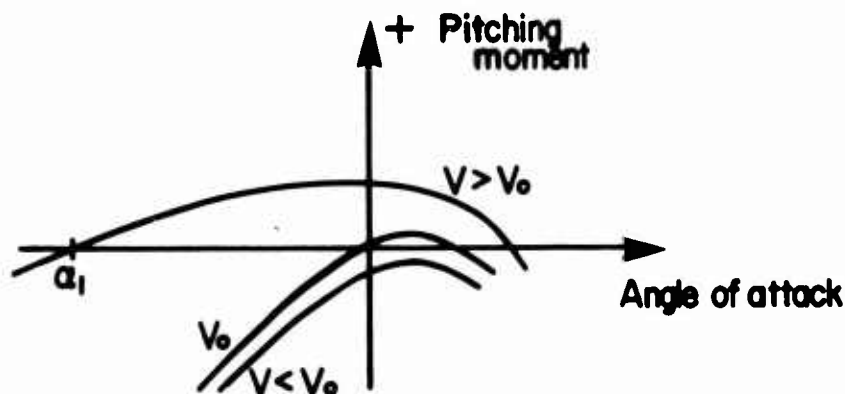
Thus, the divergent motion of the model about point A, with a resulting horizontal velocity increase, causes a motion that eventually oscillates about point B. In Appendix I, the linearized solutions near points A and B are investigated in detail.

$i_w = 50^\circ$ . At a wing incidence of  $50^\circ$ , the small disturbance motion of the model is a slightly unstable oscillation, as shown in Figure 16a. If the initial perturbation is small, the model oscillates about the level attitude trim velocity of 23 fps (model scale) in a slightly unstable manner. If the perturbation is larger, the model drifts away until a new "trim" velocity of approximately 27 fps (model scale) is reached, at which point the oscillation, although not changing period, becomes stable and appears somewhat like that present at  $i_w = 60^\circ$  after the model increased speed (Figure 16c). Although no static measurements were made at this trim condition, it would be expected that the pitching moment curves would be like those at  $i_w = 60^\circ$ , with a similar nonlinear behavior present. The

ultimate velocity about which the oscillation occurs is approximately the same as at  $60^\circ$ . Three-degree-of-freedom motions were also measured, and a neutral or slightly unstable oscillation similar to the two-degree-of-freedom motions was present (Figure 16b).

$i_w = 40^\circ$ . Transient responses at  $40^\circ$  wing incidence exhibited the most pronounced nonlinear characteristics. Experimentally, it was not possible to obtain any small amplitude motions of the model at this wing incidence. Typical runs are shown in Figure 17. Initial nose-up motion (Figure 17a) indicates a tendency to oscillate; however, as a nose-down attitude develops while the model slows down, this oscillation becomes a rapid divergence. The small amplitude nose-down motion is divergent, as may be seen from Figure 17b. Again, as in the  $60^\circ$  case, as the forward speed increases, the derivatives vary sufficiently such that the motion becomes a slightly damped and somewhat "lopsided" oscillation. Figure 17c shows the transient response in pitching only, at trim velocity. A lightly damped oscillation about a nose-up attitude occurs, indicating that at trim the pitching moment variation with angle of attack is as shown below.

The pitching moment curves determined by the static data, and verified by this single-degree-of-freedom oscillation, are as shown in the sketch below.



An initial nose-up motion brings the model into a region in which the vehicle is statically stable with angle of attack ( $M_Q < 0$ ) with single-degree-of-freedom motions, as shown in Figure 17c. As the motion proceeds and the angle of attack becomes negative, the vehicle becomes statically unstable ( $M_Q > 0$ ). The eventual motion is divergent, since the horizontal velocity has decreased. Conversely, if the initial motion is nose down, a divergent tendency exists because of the instability with angle of attack. However, as the speed increases, there will be a change in the pitching moment characteristics as shown above; i.e., the speed stability is larger at negative angles of attack, and the angle-of-attack stability is effectively negative for angles of attack greater than  $\alpha_1$  at velocities

above the trim speed. The motion at this increased speed and nose-down attitude is a "lopsided", stable oscillation. The "lopsided" character of the oscillation is due to the nonlinearity in the pitching moment variation with angle of attack.

The linearized small disturbance motions present at these various wing incidences are investigated in further detail in Appendix I; analog matching is used to compare the statically measured derivatives with the measured transient response. The comparison of the static data and the values required to match the transient motions is shown in Figure 19.

It can be seen that the agreement between these results is good, indicating that the significant derivatives have been measured and that the linearized approach to the small disturbance motions is valid.

Only a first-order discussion of the nonlinearities has been given. Further study of these phenomena is considered to be highly desirable, since some nonlinear behavior is probably typical of tilt-wing aircraft in this speed range where the linearized derivatives are quite small.

The dynamic responses of the model discussed above cannot be precisely interpreted in terms of full-scale motions primarily because of the location of the model center of gravity, which was somewhat too high and forward compared to the location of the center of gravity of the full-scale aircraft. The horizontal center-of-gravity location was 9-percent MAC. While this is somewhat forward in terms of the center-of-gravity range on the actual full-scale aircraft, the horizontal center-of-gravity position in the low speed range has only a small effect on the stability characteristics, as shown in Appendix IV. The vertical center-of-gravity location is taken into account for the discussion in the next section. All aerodynamic data are presented for the proper full-scale vertical center-of-gravity location.

In addition, the scale-model gross weight was too large. The data for this heavy model may be shown, through dimensional analysis, to be exactly equivalent to the motions of a lighter model at a reduced density. That is, if we consider a series of dynamic stability measurements on an aircraft in which, as the altitude of the test is changed, the gross weight is reduced, such that the aircraft mass divided by the air density is constant, there will be no change in the response characteristics of the aircraft at the same flight speed. Thus, for example, at wing incidences of  $50^\circ$  and  $40^\circ$ , the model was in vertical trim, and its weight was 50 pounds. This would be equivalent to a full-scale aircraft weighing 50,000 pounds at sea level and an aircraft weighing 37,400 pounds at 8500 feet

( $\sigma = 0.748 = \frac{37,400}{50,000}$ ). This is an exact equivalence, and so the RFM and

blade angle would be exactly scaled. This point is discussed further in Appendix II. This equivalence indicates that for direct comparisons of model and full-scale data, it is desirable to conduct experiments on heavy



models, since the flight test will always take place at altitudes above sea level.

None of the above effects significantly change the character of the transient motions of the full-scale aircraft in comparison to the model data. The transient responses measured here agree closely with those presented in Reference 4 at the two high wing incidences included ( $90^\circ$  and  $65^\circ$ ). No detailed comparison has been made because of slight differences in the geometric and mass parameters of the two models.

## DYNAMICS OF THE FULL-SCALE AIRCRAFT

In this section the dynamic stability characteristics that result from the model tests are discussed. The full-scale derivatives obtained from the data and the analysis presented in Appendix I are given in Figure 21. Consideration here is restricted to the linearized small-amplitude motions, for reasons discussed in the Introduction.

The dimensional derivatives are presented for a full-scale aircraft using the altitude gross weight equivalence discussed in Appendix II. The density altitude corresponding to any selected gross weight and wing incidence is shown in Figure 22. This method of presentation is considered to be useful for comparison with flight test. Other methods of interpreting the model data, which do not alter the general trends of the derivatives, are discussed in Appendix II.

The derivatives presented are based on a stability axis system shown in Figure 20. They are presented as functions of flight velocity rather than wing incidence, since the experimental results are more strongly dependent on velocity. This fact may be seen by comparing the stability derivatives at a wing incidence of  $60^\circ$  for a level and nose-down trim to those at a wing incidence of  $50^\circ$ .

In cases where the derivative is nonlinear, or was not determined, the probable trend is indicated by a dashed line. For example, the vertical velocity derivatives at hover were small and were not measured.

We now consider first the individual stability derivatives and then the dynamic motions that result.

### STABILITY DERIVATIVES

The various derivatives for the full-scale aircraft are shown in Figure 21. The general trends are as follows:

The Speed Stability ( $M_u$ ). This derivative is very large and positive in or near hovering flight and remains roughly constant for flight speeds from hover to approximately 20 knots. Then it decreases very rapidly, becoming small and negative at 35 knots. Further increases in speed, with corresponding changes in wing incidence, result in a reversal of this trend; the derivative increases and is positive and comparatively small at 60 knots. The large value near hovering produces an oscillatory instability and an appreciable sensitivity to horizontal gusts. The negative value of this derivative near a wing incidence of  $60^\circ$  gives rise to a static instability, and the resulting transient motion of the aircraft is divergent. The negative speed stability obtained from a detailed analysis of the data differs from preliminary analyses of the data made by the LTV Aerospace Corporation. The negative value is verified by the comparison of the static data and the

measured transient response data from the model.

The Angle-of-Attack Stability ( $M_w$ ). This derivative is generally small and positive (unstable) throughout most of the speed range investigated, corresponding to the general trend indicated for this type of vehicle in Reference 8. At lower wing incidences and higher speeds investigated, it becomes negative (stable), although it is markedly nonlinear at a wing incidence of  $40^\circ$ . Apparently the forward speed is not large enough to result in an appreciable stabilizing contribution from the horizontal tail, or else the horizontal tail incidence and downwash angle are such that the tail is stalled. Note that the horizontal tail incidence differs from that in use on the aircraft (Figure 6).

The Pitch Damping ( $M_q$ ). This derivative is very small near hovering and is slightly negative. It increases in a favorable sense (negatively) as the speed increases. The magnitude of this derivative determined by the experiments indicates that the full-scale vehicle would require damping augmentation to provide satisfactory flying qualities, since the level is considerably below that indicated by handling qualities studies as desirable (Reference 12, for example). Again, the forward speed is not great enough to produce an appreciable contribution from the horizontal tail.

The Downwash Lag ( $M_u$ ). It has been assumed in this analysis that  $M_u = 0$ , as discussed earlier.

The Rate of Change of Horizontal Force With Velocity ( $X_u$ ). This derivative, as would be expected, follows the trends of  $M_u$  closely at low speeds. It is very large in hovering, and at about 20 knots is decreasing quite rapidly with increasing speed. A minimum value occurs at 40 knots, and then there is a slow increase with forward speed. The large value in hovering has a favorable effect on the dynamic stability.

The Lift Curve Slope ( $Z_w$ ). This derivative is rather small and nonlinear throughout the speed range investigated. This would be expected of a vehicle flying at low speeds primarily on propeller thrust rather than wing lift. Some measurements were made to determine  $Z_w$  in hovering, where it would be significant in determining the nature of the altitude response of the vehicle. These experiments were inconclusive, only indicating that the magnitude of this derivative was quite small.

The Rate of Change of Lift With Velocity ( $Z_u$ ). This derivative is rather small and dependent upon the angle of attack of the vehicle, as shown in Figure 11. The variation with angle of attack may arise from wing stalling as well as the general nature of propeller thrust variation with speed, which is quite sensitive to angle of attack at low advance ratios (Reference 13).

Rate of Change of Horizontal Force With Angle of Attack ( $X_w$ ). This derivative is rather small and varies in sign over the speed range investigated and is not particularly important.

#### DYNAMIC STABILITY CHARACTERISTICS

The dynamic stability characteristics of the full-scale vehicle that are predicted by these derivatives are now considered.

The values of the stability derivatives discussed above and given in Figure 21 are placed in the linearized equations of motion of the vehicle, and the characteristic roots are evaluated.

For comparison purposes, the two-degree-of-freedom motions ( $\theta = \alpha$ ) and the three-degree-of-freedom motions are computed. Basically, the results indicate that very similar results for the characteristics of the unstable motions are predicted in either case, indicating that, in general, the angle-of-attack derivatives are rather small.

$$\begin{aligned} \dot{u} - X_u u - X_w w + g\theta &= 0 \\ Z_u u + Z_w w - \dot{w} + V_0 \dot{\theta} &= 0 \\ M_u u + M_w w + M_\theta \dot{\theta} - \ddot{\theta} &= 0 \end{aligned}$$

To determine the two-degree-of-freedom motions with the flight path level, we set  $w = V_0 \theta$  in the above equations and discard the vertical force equation. The following results were obtained:

$i_w = 89^\circ$ . At this wing incidence, corresponding to hover, only the two-degree-of-freedom motions are considered, since the vertical equation is uncoupled. The roots of the characteristic equation obtained are:

$$\begin{aligned} s_1 &= -1.1 \\ s_{2,3} &= +0.25 \pm 0.74i \end{aligned}$$

corresponding to a convergence with a time constant of 0.9 second and an unstable oscillation with a period of 8.5 seconds, and a time to double amplitude of 2.8 seconds. Thus, the vehicle is quite unstable in hovering and would be difficult to fly, particularly in gusty weather, since this instability arises from a large value of the speed stability ( $M_u$ ). At a wing incidence of  $80^\circ$ , the dynamics are similar.

$i_w = 70^\circ$ . At this wing incidence, the two- and three-degree-of-freedom results are:

Two degrees of freedom:

$$s_1 = - 0.84$$

$$s_{2,3} = + 0.26 \pm 0.531$$

Three degrees of freedom:

$$s_1 = + 0.16$$

$$s_2 = - 1.1$$

$$s_{3,4} = + 0.29 \pm 0.441$$

The unstable oscillation is similar in both the two- and three-degree-of-freedom cases; however, in the three-degree-of-freedom case we obtain an additional root corresponding to a slow divergence. The divergence has a time constant of 6.5 seconds, and the unstable oscillation has a period of 14.3 seconds and a time to double amplitude of 2.5 seconds. The divergence and unstable oscillation, indicating unfavorable stability characteristics, result from the comparatively large speed stability, positive (unstable) angle-of-attack stability, and low angular damping.

$i_w = 60^\circ$ . At this wing incidence, the two- and three-degree-of-freedom motions are similar and the small disturbance characteristic roots are:

Two degrees of freedom:

$$s_1 = + 0.33$$

$$s_{2,3} = - 0.26 \pm 0.331$$

Three degrees of freedom:

$$s_1 = + 0.47$$

$$s_2 = - 0.37$$

$$s_{3,4} = - 0.17 \pm 0.201$$

The three-degree-of-freedom motions consist of a divergence that is fairly rapid with a time constant of 2.14 seconds, a convergence, and a stable oscillation with a period of 31 seconds and a time to half amplitude of 4.1 seconds. The divergence arises from the negative value of the speed stability and the positive angle-of-attack stability.

$i_w = 40^\circ$ . This is the case in which the motion was quite nonlinear, and so it is difficult to justify small disturbance calculations, since the sign of the attitude stability depends upon the direction of motion. For nose-up motions, the small disturbance motion would be stable; and for nose-down disturbances, the small disturbance motion would be unstable. The following characteristic roots result.

Nose Down	Nose Up
$s_1 = + 0.36$	$s_1 = - 0.09$
$s_2 = - 1.2$	$s_2 = - 0.54$
$s_3 = + 0.22$	$s_{3,4} = - 0.04 \pm 0.471$
$s_4 = - 0.12$	

The nose-down motion is unstable. There are two divergences of 2.8 seconds and 4.6 seconds, respectively. On the basis of the nose-up value of the angle-of-attack stability, the dynamic motions are stable, dominated by a lightly damped motion with a period of 13.3 seconds.

It should be realized that considering this case as a linear motion is only a crude approximation to the actual case. Nonetheless, we see favorable trends in the dynamics beginning to appear.

When the above results are summarized, the general nature of the longitudinal motions of this aircraft at high wing incidences falls into two areas.

At very high incidence ( $90^\circ > i_w > 70^\circ$ ) and correspondingly slow speeds, the longitudinal dynamic characteristics are dominated by a high value of the speed stability ( $M_u$ ). The transient motion is dominated by an unstable oscillation typical of helicopters and other propeller-driven VTOL aircraft near hovering.

At intermediate wing incidences ( $70^\circ > i_w > 40^\circ$ ), the motions become somewhat more complex, since both the speed stability and the angle-of-attack stability are small and nonlinear. The linearized motions of this vehicle are dominated by divergent modes. The linearized derivatives are small and

quite sensitive to details of the configuration. Nonlinear behavior is probably typical of this flight regime, since the change of sign of  $M_{\dot{\alpha}}$  is characteristic of these aircraft (References 3 and 8). In any flight condition where the linearized derivatives are zero or near zero, it would be expected that nonlinearities would be evident in the response. The importance of these nonlinearities merits further investigation. It would be expected that various tilt-wing VTOLs would exhibit quite dissimilar stability characteristics in this regime that would depend on the details of the configuration.

## CONCLUSIONS

As a result of the model tests, the following conclusions may be drawn:

1. For this tilt-wing VTOL, the longitudinal motions at wing incidences above  $40^\circ$  are dynamically unstable. Two regions with a generally different character of motion are indicated:
  - a. At wing incidences between  $90^\circ$  and  $70^\circ$ , a large speed stability derivative and low angular damping produce an unstable oscillation of about a 9-second period.
  - b. At wing incidences between  $70^\circ$  and  $40^\circ$ , the motions are quite complex. Small linearized values of the speed stability and the angle-of-attack stability result in the appearance of nonlinearities in the dynamic motions. The dominating linearized motion was a divergence due to the change in sign of the speed stability and the positive angle-of-attack stability.
2. Favorable trends in the pitching moment derivatives are beginning to appear at a wing incidence of  $40^\circ$  and below.
3. Detailed consideration of nonlinearities is necessary to predict the large amplitude motions noted at wing incidences between  $60^\circ$  and  $40^\circ$ .
4. Hysteresis was evident in the force and moment measurements at flight speeds near hover.



### RECOMMENDATIONS

1. Further detailed study of the nature and importance of nonlinear behavior at wing incidences between  $70^\circ$  and  $40^\circ$  is desirable. The presence of nonlinearities is probably typical of tilt-wing vehicles in this incidence range, as the speed stability is near zero and the angle-of-attack stability is changing sign.
2. These data should be compared with flight test results, where possible, to increase confidence in model testing for quantitative dynamic stability characteristics. While the results of Reference 4 indicate that this configuration is flyable without automatic stabilization, the nature of the dynamic motions measured indicates that flight testing for stability derivatives in this speed range will be difficult.

## REFERENCES

1. Boyden, R. P., and Curtiss, H. C., Jr., An Experimental Investigation of the Lateral-Directional Stability Characteristics of a Four-Propeller, Tilt-Wing VTOL Model at Low Speeds, Princeton University, Department of Aerospace and Mechanical Sciences, Report No. 743, Princeton, New Jersey, June 1965.
2. Beppu, G., and Curtiss, H. C., Jr., An Analytical Study of Factors Influencing the Longitudinal Stability of Tilt-Wing VTOL Aircraft, U. S. Army Aviation Materiel Laboratories, USAAVLABS Technical Report 66-53, Fort Eustis, Virginia, July 1966.
3. Curnutt, R. A., and Curtiss, H. C., Jr., Comparison of Longitudinal Stability Characteristics of Three Tilt-Wing VTOL Aircraft Designs, U. S. Army Aviation Materiel Laboratories, USAAVLABS Technical Report 66-64, Fort Eustis, Virginia, 1966.
4. Newsom, W. A., Jr., and Kirby, R. H., Flight Investigation of Stability and Control Characteristics of a 1/9-Scale Model of a Four-Propeller Tilt-Wing V/STOL Transport, NASA TN D-2443, Washington, D. C., September 1964.
5. Deckert, Wallace H., and Page, V. Robert, Large-Scale Wind-Tunnel Tests of Descent Performance of an Airplane Model With a Tilt Wing and Differential Propeller Thrust, NASA TN D-1857, Washington, D. C., October 1964.
6. Curtiss, H. C., Jr., Putman, W. F., and Traybar, J. J., The Princeton Dynamic Model Track, Presented at the AIAA Aerodynamic Testing Conference, Washington, D. C., March 9-10, 1964.
7. Curtiss, H. C., Jr., Putman, W. F., and Martinez, E., The Evaluation of Stability and Control Characteristics of Aircraft at Low Speeds Using Dynamically Similar Models in Semi-Free Flight, Proceedings of the American Helicopter Society Eighteenth Annual National Forum, Washington, D. C., May 1962.
8. NASA Conference on V/STOL Aircraft, A Compilation of the Papers Presented, (Langley Research Center) Langley Field, Virginia, November 17-18, 1960.
9. Curtiss, H. C., Jr., Traybar, J. J., and Putman, W. F., General Description of the Princeton Dynamic Model Track, U. S. Army Aviation Materiel Laboratories, USAAVLABS Technical Report 66-73, Fort Eustis, Virginia, November 1966

10. Farren, W. S., The Reaction on a Wing Whose Angle of Incidence is Changing Rapidly, Aeronautical Research Council of Great Britain, R. & M. No. 1648, January 1935.
11. Bennett, R. M., and Curtiss, H. C., Jr., An Experimental Investigation of Helicopter Stability Characteristics Near Hovering Flight Using a Dynamically Similar Model, Princeton University, Department of Aerospace and Mechanical Sciences, Report No. 517, Princeton, New Jersey, July 1960.
12. Seckel, E., Traybar, J. J., and Miller, G. E., Longitudinal Handling Qualities for Hovering, Proceedings of the Eighteenth Annual National Forum, Washington, D. C., May 2,3,4, 1962.
13. Shapiro, Jacob, Principles of Helicopter Engineering, page 56, McGraw Hill, New York, 1955.
14. Seckel, E., Stability and Control of Airplanes and Helicopters, Academic Press, New York, 1964.
15. Kuhn, Richard E., and Draper, John W., Investigation of the Aerodynamic Characteristics of a Model Wing-Propeller Combination and of the Wing and Propeller Separately at Angles of Attack up to 90°, NACA Report 1263, 1956.
16. Durand, William Frederick, Ed., Aerodynamic Theory, reprinted by Dover Publications, New York, 1963, Volume IV, Division L, "Airplane Propellers," by H. Glauert.
17. Josephs, L. C., VHR-447 Tri-Service Transport Proposal, Volume 7 Summary Report, Part 2, Airplane Description, Chance Vought Corporation, Hiller Aircraft Corporation and Ryan Aeronautical Company, AER-ElR-13347, April 1961.
18. Shields, M. E., Estimated Flying Qualities XC-142A V/STOL Assault Transport, LTV Aerospace Corporation, Report No. 2-53310/4R939, Dallas, Texas, May 1964.
19. Ransone, Robin K., and Jones, Gay E., XC-142A V/STOL Transport Tri-Service Limited Category I Evaluation, Air Force Flight Test Center, Technical Report No. 65-27, Edwards Air Force Base, California, January 1966.

## APPENDIX I

### ANALYSIS OF DATA

#### AXIS SYSTEM AND EQUATIONS OF MOTION

In this section the experimental data discussed in the text are analyzed to evaluate and correlate the static and dynamic data taken on the model.

The results are analyzed on a linear, or at least piecewise linear, basis. It is considered that this approach is justified from the nature of the data in most cases and that this is the most significant aspect of the data, for reasons discussed in the Introduction. The oscillation measured at a wing incidence of  $40^\circ$  was the only distinctly nonlinear oscillation.

Theoretical linearized equations of motion were set up on an analog computer. Then, using the static derivatives obtained from strain gauge measurements as a starting point, the coefficients in the linearized equations were adjusted until a good match of the measured model transient motion (small amplitude) was obtained.

Measurements of the model motions are made with respect to a carriage, and it is therefore convenient to use a space-fixed axis system to analyze the motion rather than the more conventional stability axis system. The X-axis is located along the direction of the motion of the carriage, the Z-axis is located perpendicular to it, and the origin of the axes system is placed at the pivot point where the model is attached to the vertical link. The stability axis system and the space axis system are shown in Figure 20. The mounting of the model is shown in Figure 23. The pivot axis of the model corresponds to the point about which static force and moment measurements were made and is equivalent to a full-scale aircraft center-of-gravity location of 9-percent MAC. The actual model center of gravity was above this point, and its location is reflected by additional terms in the model equations of motion in the following.

Inertial and gravity components of the forces and moments acting at the pivot point are shown graphically in Figure 23. The location of the pivot point with respect to the model is given in Table I. Since only two-degree-of-freedom motion is considered in the analysis, with vertical velocity zero, only the horizontal force and the pitching moment equations are needed. Summing inertial and gravity forces from Figure 23,

$$\Sigma X_1 = - m \ddot{u} - m_1 \ddot{u} - m_2 \ddot{u} , \quad (1)$$

where  $m$  is the mass of the model and  $m_1$  and  $m_2$  are the masses of the

mounting linkages. Summing pitching moments about the pivot axis due to inertial and gravity forces,

$$\Sigma M = - I_y \ddot{\theta} + l m \dot{u} \cos \theta + m g l \sin \theta , \quad (2)$$

where the last two terms on the right-hand side are due to the model center of gravity located at a distance  $l$  above the pivot axis, and  $I_y$  is the moment of inertia of the model about this axis. The distance  $l$  as a function of wing incidence is also shown in Figure 23.

Under the assumption that the dynamic motion of the model may be described by small-perturbation, linearized equations, the aerodynamic forces and moments are expanded in a Taylor series about equilibrium flight conditions, as discussed in Reference 14.

These aerodynamic terms are summed with the inertial and gravity forces and moments from equations (1) and (2), and the following equations of motion result for trimmed level flight:

$$- m' \ddot{u} + \frac{\partial X}{\partial u} u + \frac{\partial X}{\partial \theta_f} \theta_f = 0 \quad (3)$$

$$m l \dot{u} + \frac{\partial M}{\partial u} u - I_y \ddot{\theta} + \frac{\partial M}{\partial \dot{\theta}_f} \dot{\theta}_f + \left( \frac{\partial M_a}{\partial \theta_f} - m g l \right) \theta_f = 0 , \quad (4)$$

where  $u$  and  $\theta_f$  are perturbations from trim. It is assumed that  $\frac{\partial X}{\partial \theta_f}$  is negligible. Control input terms are not included, since no inputs were applied.

The horizontal force equation is divided by  $m'$  ( $= m + m_1 + m_2$ ), and the pitching moment equation is divided by  $I_y$ . Since equations (3) and (4) are linear, the solutions will be of the form  $u = \bar{u} e^{st}$  and  $\theta = \bar{\theta} e^{st}$ . Substituting these expressions, equations (3) and (4) become

$$\begin{bmatrix} (s - X_u) & - X_{\theta_f} \\ \left( \frac{m l}{I_y} s + M_u \right) & \left( - s^2 + M_{\dot{\theta}_f} s + M_{\theta_f} + \frac{m g l}{I_y} \right) \end{bmatrix} \begin{bmatrix} \bar{u} \\ \bar{\theta}_f \end{bmatrix} = \begin{bmatrix} 0 \\ 0 \end{bmatrix} . \quad (5)$$

In order to obtain nontrivial solutions for "s", the determinant of the coefficient matrix must vanish; this is the characteristic determinant, and yields the characteristic equation:

$$\begin{bmatrix} (s - X_u) & -X_{\theta_f} \\ \left(\frac{m\ell}{I_y} s + M_u\right) & \left(-s^2 + M_{\dot{\theta}_f} s + M_{\theta_f} + \frac{mg\ell}{I_y}\right) \end{bmatrix} = 0. \quad (6)$$

The values of "s" which satisfy this equation are the characteristic roots of the system and determine the character of the transient modes of motion of the aircraft.

There are several terms in this determinant that do not appear in the usual case. The two terms  $\frac{m\ell}{I_y}$  and  $\frac{mg\ell}{I_y}$  account for the fact that the origin of the axis system is not coincident with the center of gravity of the model, and therefore there are inertial and gravity additions to the moment summation. Other differences are attributable to the use of a space-fixed axis system rather than a body-fixed system. There is no vertical velocity (the flight path is horizontal) in the space-fixed system for the two-degree-of-freedom motions considered; a rotation,  $\theta_f$ , of the model, however, causes a change in the body axis velocity  $w_b = u \sin \theta_f$ , or equivalently, a change in angle of attack ( $\alpha = \theta_f$ ). The derivatives  $X_{\theta_f}$  and  $M_{\theta_f}$  are directly related to  $X_w$  and  $M_w$ , respectively, in the stability axis system, as shown in Table IV.

#### SIMULATION RESULTS AND ANALYSIS

The static stability derivatives as determined by force and moment measurements and the angular damping obtained from single-degree-of-freedom responses, were used as initial potentiometer settings on an analog computer. Certain of the derivatives were then varied to match the computer solution to the characteristics of the measured model transient responses.

While, in principle, one should have only to place the statically measured derivatives in the equations, add the angular damping, and obtain the measured transient response, actually carrying out this step serves as a useful check on the correlation between the static and dynamic data, as well as verifies the assumed form of the equations of motion. In addition, in these experiments, rather limited angle-of-attack information was available, since only three angle-of-attack points were measured.

Three of the five stability derivatives were varied from their statically measured values to obtain the desired matching of responses - the three

moment derivatives,  $M_u$ ,  $M_{\dot{\theta}_f}$ , and  $M_{\theta_f}$  - since they exert the greatest influence on the oscillatory portion of the response.

Although  $X_u$  and  $X_{\theta_f}$  also affect the transient motion, relatively large changes are necessary to affect significantly the response characteristics. The value of  $X_{\theta_f}$  is primarily determined by the initial value of the vertical aerodynamic force in the low speed range (in hovering, it is precisely this value) and is reasonably linear (Figure 9). The horizontal force variation with velocity is approximately linear except near a wing incidence of  $70^\circ$  (Figure 10). The values of  $X_u$  and  $X_{\theta_f}$  were therefore set at the values determined by the force measurements for all matching.

Typically, in this speed range, the longitudinal modes of motion in two degrees of freedom consist of an unstable oscillation or a divergence and one or two convergent modes. The contribution of convergent modes to the transient motion is masked by the unstable modes. The accuracy with which the convergent modes of the response are matched cannot be evaluated. Inputs which excite these convergent modes will result in very large motions because of the presence of the unstable modes. As a result, there is a certain degree of nonuniqueness in the results which is reflected by different combinations of the pitching moment derivatives producing essentially identical responses. For this reason, the derivative  $M_u$  was never varied appreciably from the measured static value. Thus, the derivatives  $M_{\dot{\theta}_f}$  and  $M_{\theta_f}$  were adjusted to produce the match.  $M_{\dot{\theta}_f}$  was rather small throughout the low speed range and was rather difficult to evaluate precisely from the single-degree-of-freedom experiments. The limited angle-of-attack information made it desirable to consider  $M_{\theta_f}$  ( $M_\alpha$ ) essentially as unknown.

$i_w = 89^\circ$  - Hover

The static values of the stability derivatives at this wing incidence are shown in Figure 10. The average oscillatory characteristics of the model dynamic responses (runs HFR 1 through HFR 18) were determined to be

$$P = 3.61 \text{ seconds}$$

$$\frac{A_{n+1/2}}{A_n} = 5 .$$

A typical response is shown in Figure 12.

A comparison of the static values and the analog matching values is given below.

Derivative	Analog Matching	Static Value	Units
$M_u$	$= + 0.47 \pm 0.03$	$+ 0.569$	per foot-second
$M_{\theta_f}$	$= 0$	$0$	per second squared
$M_{\dot{\theta}_f}$	$= + 0.47 \pm 0.03$	$- 0.395$	per second

The experimental errors given for the derivatives at this wing incidence, and those given for the succeeding incidences, are estimated simulation errors-that is, the amount each derivative may be changed before an obvious change in the computed response is apparent.

For this incidence, the model data were repeatable, with relatively little scatter. The simulated value of  $M_u$  differs from the static value. This difference probably arises from effective linearization of the hysteresis effect present in the static data. The values of  $M_{\theta_f}$  agree exactly, since this derivative was left unchanged. Although single-degree-of-freedom  $M_{\theta_f}$  and simulated  $M_{\dot{\theta}_f}$  have different signs, the agreement is considered good, since the actual magnitude of this term is small. The accuracy of the result from the single-degree-of-freedom experiments is difficult to evaluate in hover because of the presence of some downwash recirculation. Recirculation effects are particularly noticeable when the angular damping is small.

$$\underline{i_w = 80^\circ}$$

The transient motion at  $80^\circ$  was very similar to that at  $89^\circ$ . A typical transient response is shown in Figure 13. This case was not analyzed in detail.

$$\underline{i_w = 70^\circ}$$

The model static data for this wing incidence are given in Figure 10. The model oscillatory characteristics were taken from runs 64RC to 69RC, which were the five initial nose-up model responses measured at this wing incidence. As discussed in Experimental Results, there was a difference in the nose-up and nose-down motions, as shown in Figure 14, due to the decreasing values of the derivatives with increasing speed. Only the nose-up motion



was matched due to the difficulty of precisely matching a divergent motion. The oscillatory characteristics measured for nose up were:

$$P \approx 4.75 \text{ seconds}$$

$$\frac{A_{n+1/2}}{A_n} \approx 8 .$$

The peak amplitude ratio is approximate, since the model never completed more than a cycle of transient motion before reaching the angular limits. An "averaging" error on the order of 15-20 percent is associated with this value.

The derivative values used to achieve the match on the analog computer compared to the static data are:

Derivative	Analog Matching	Static Value	Units
$M_u$	$= + 0.38 \pm 0.03$	$+ 0.38$	per foot-second
$M_{\theta_f}$	$= + 3.30$	$+ 3.30$	per second squared
$M_{\dot{\theta}_f}$	$= - 0.88 \pm 0.06$	$- 0.253$ (interpolated)	per second

It should be noted that any error in this matching is inherent in the evaluation of the dynamics of a highly unstable system rather than associated with experiment.  $M_u$  agrees with the static value, and  $M_{\theta_f}$ , which was again unchanged, is identical. A difference of  $\pm 0.001$  in  $M_u$  changed the period of the oscillation by 0.2 second on the simulator, without visibly affecting the amplitude ratio; with  $M_{\theta_f}$  held constant,  $M_u$  affected primarily the period of the motion while  $M_{\dot{\theta}_f}$  affected the damping. The simulated value of  $M_{\dot{\theta}_f}$  appears quite different from the interpolated single-degree-of-freedom value of  $- 0.25$ . It is likely that  $M_{\dot{\theta}_f}$  is between  $- 0.3$  and  $- 1.0$ . Since  $M_{\dot{\theta}_f}$  has a strong effect on the peak amplitude ratio, its magnitude cannot be determined more exactly because of the unstable character of the transient motion. Again, the angular damping is very small, and while the percentage error is large, these differences do not reflect large changes in the transient motion. That is, any value of  $M_{\dot{\theta}_f}$  between  $- 0.3$  and  $- 1.0$  would correspond to a very low level of angular damping on the full-scale vehicle.

$$i_w = 60^\circ$$

The static values of the derivatives at  $i_w = 60^\circ$  are summarized in Figure 10. The dynamic model runs at this wing angle were 83RC-84RC, 88RC-91RC, 96RC-98RC, 100RC, 105RC-106RC, and 109RC. Typical responses with initial nose-up rotation (run 91RC) and initial nose-down rotation (run 98RC) are shown in Figure 15. A considerable number of runs at this condition indicated good repeatability of the transient motions.

Following the procedure described, the static values of the derivatives were initially set on the analog computer. From Figure 10, these values for the three derivatives are:

Derivative	Static Value	Units
$M_u$	= - 0.0474	per foot-second
$M_{\theta_f}$	= + 0.85	per second squared
$\dot{M}_{\theta_f}$	= - 0.253	per second

These values yielded a rapid divergence. The character of this response was qualitatively equal to the initial motions in either direction given in Figure 15.

Nonlinear behavior was quite evident at this wing incidence for nose-down motions, as discussed in the test. However, indications were that this motion was piecewise linear, and so the final portion of the response, a lightly damped oscillation occurring at an increased speed and nose-down attitude, was matched on a linear basis, resulting in the following derivatives:

Derivative	Analog Matching	Units
$M_u$	= + 0.135	per foot-second
$M_{\theta_f}$	= - 4.06	per second squared
$\dot{M}_{\theta_f}$	= - 0.894	per second

The changes in  $M_u$  and  $M_{\theta_f}$  from their initial values at level attitude

trim are roughly equivalent to a single second-order term. That is, the nonlinear behavior noted should be approximately accounted for by a single term,  $\frac{\partial^2 M}{\partial \theta_f \partial u}$ , of the order of - 0.05. The general trend of the changes in the derivatives is shown by the static data.

The increase in the angular damping arises from the increased dynamic pressure at the horizontal tail.

$$i_w = 50^\circ$$

There were no static measurements or single-degree-of-freedom damping measurements made at  $i_w = 50^\circ$ . The model dynamic tests consisted of runs 117RC-122RC, 134RC, and 135RC-137RC.

As discussed above, two different responses were repeatable at this wing incidence; two examples are shown in Figure 16 (runs 121RC, 134RC).

The oscillatory characteristics of the small perturbation response were determined to be approximately

$$P = 3.8 \text{ seconds}$$

$$\frac{A_{n+1/2}}{A_n} = 1.2 .$$

The derivative results for the simulator match shown in Figure 19 were:

Derivative	Analog Matching	Units
$M_u$	$= + 0.13 \pm 0.02$	per foot-second
$M_{\theta_f}$	$= - 2.7 \pm 0.2$	per second squared
$M_{\dot{\theta}_f}$	$= - 0.69 \pm 0.06$	per second

These derivatives are quite similar to the final values at the  $i_w = 60^\circ$  case, as would be expected.

The ultimate large amplitude motion corresponds closely to the large amplitude motion at  $i_w = 60^\circ$ , indicating that the stability derivatives are primarily a function of forward speed rather than wing incidence. The

two equilibriums appear to be identical, as trim velocities are the same, and the wing angles with respect to space are approximately equal. (At  $i_w = 60^\circ$ , the average fuselage angle in the final equilibrium is between  $-5^\circ$  and  $-10^\circ$ , placing the wing at  $50^\circ$ - $55^\circ$  with respect to the horizon; at  $i_w = 50^\circ$ , average fuselage angle is  $\cong -2^\circ$  to  $-4^\circ$ .) This behavior is a result of a nonlinear variation of the pitching moment derivatives similar to that at  $60^\circ$ .

$$i_w = 40^\circ$$

Transient responses at  $40^\circ$  wing incidence exhibited perhaps the most pronounced nonlinear characteristics. Typical runs are shown in Figure 17. The initial nose-up motion shows a tendency to oscillate; however, as nose-down motion develops, this oscillation becomes a rapid divergence as the model slows down. The initial nose-down motion is a divergence. Again, as in the  $60^\circ$  case, as the forward speed increases, the derivatives change enough such that the motion becomes a lightly damped and somewhat "lopsided" oscillation.

Using the initial values determined from static tests and the single-degree-of-freedom experiments for damping, the initial nose-down and nose-up motions were reasonably well matched. The value of  $M_{\theta_f}$  was that corresponding to the initial direction of motion:

Derivative	Static		Units
	Nose Down	Nose Up	
$M_u$	= + 0.17	+ 0.17	per foot-second
$M_{\theta_f}$	= + 7.5	- 2.4	per second squared
$M_{\dot{\theta}_f}$	= - 1.83	- 1.83	per second

These static values result in a divergence nose down, and a nearly neutrally stable oscillation nose up, thus agreeing with the initial responses measured.

The final oscillatory motion at  $40^\circ$  was definitely nonlinear, and so no attempt to match this motion on a linearized basis was made.

To summarize these results, the static and single-degree-of-freedom measurements predict the measured transient motions quite well, indicating that the significant derivatives have been taken into account. There appears to be some discrepancy between the damping derivative as determined from the single-degree-of-freedom responses and that required to match the

two-degree-of-freedom motion. This is probably due to the small size of this derivative in the speed range investigated.

Further consideration of the impact of the nonlinearities noted is considered desirable, as they appear quite typical of these intermediate wing angles where the angle-of-attack derivative is changing sign and the speed stability is small.

## APPENDIX II

### NOTES ON METHOD OF CONDUCTING EXPERIMENTS AND SCALING OF DATA

#### FORM OF DATA PRESENTATION

The model data has been presented in the form of dimensional forces and moments rather than in a nondimensional form. This form of presentation was chosen for the following reasons.

It is not convenient to base the coefficients on forward speed, since the data presented encompass hovering and low forward speeds; coefficients based on free-stream dynamic pressure would be numerically large at low forward speeds, and undefined at hover. Use of coefficients based on the slipstream velocity (Reference 15) would necessitate assumptions regarding the variation of propeller forces with forward speed and angle of attack, since no direct measurement of thrust was possible on the dynamic model used in these experiments; presentation of the coefficients in this manner is therefore considered undesirable, since the variations in the data would then depend on these assumptions, which were made for purposes of nondimensionalization. Basing the coefficients on propeller tip speed also was considered undesirable, because, on the basis of certain physical considerations, a broader interpretation of the data is possible. This interpretation implies that the coefficients based on tip speed do not scale. Therefore, the data are presented in dimensional form.

#### AERODYNAMIC CONSIDERATIONS

In order to interpret the model data, and to apply them to a full-scale aircraft through the laws of dynamic similitude, it is important to understand the method in which the experiments were conducted to properly scale the important physical parameters. Although the principles of dimensional analysis are assumed to be familiar, this section discusses briefly the implications of this analysis regarding scaling.

In general, the horizontal and vertical aerodynamic forces acting on a model with a given geometry will be a function of propeller blade angle, aircraft angle of attack, forward velocity, and propeller tip speed:

$$X = X(\beta, \alpha, V, \Omega R)$$

$$Z = Z(\beta, \alpha, V, \Omega R)$$

These relationships may be nondimensionalized in several ways through dimensional analysis; for the purposes of this discussion, consider a nondimensionalization by air density,  $\Omega R$ , and a suitable area. Then, for

given flight conditions,

$$C_x = C_x(\mu, \beta)$$

$$C_z = C_z(\mu, \beta) .$$

The trim conditions in level flight require that  $X = 0$ ,  $Z = W$ . These two conditions give unique values of  $\mu$  and  $\beta$ . The first step in powered model testing for stability derivatives is to determine the proper values of  $\beta$  and  $\mu$  to satisfy the trim requirements.

At the time the experiments were conducted, the full-scale aircraft blade angle was not known. To eliminate the necessity of finding values of  $\beta$  and  $\mu$  to satisfy both trim conditions, the blade angle was set at a reasonable value for low speed flight, and the velocity at which  $C_x = 0$  was taken to be the trim condition. This procedure may be justified by the following considerations.

It may be shown, using momentum theory (Reference 16), that the parameters  $\mu$  and  $\beta$  may be replaced with a single parameter  $C_{T,s}$  under the assumption that the primary aerodynamic force and moment contributions due to the propeller arise from the axial increment in slipstream velocity. This implies that it is not necessary to simulate individually both  $\beta$  and  $\mu$ ; it is necessary only to simulate the proper value of propeller thrust to match the ratio of the slipstream velocity increment to the forward velocity. This assumption is usually made in powered model testing (Reference 15, for example) and is considered satisfactory as long as  $\beta$  and  $\mu$  are near their proper values. Under this assumption, for a given angle of attack, coefficients based on forward speed may be expressed as a function of the single parameter  $C_{T,s}$  as

$$C'_z = C_z \mu^2 = C'_z(C_{T,s})$$

$$C'_x = C_x \mu^2 = C'_x(C_{T,s}) .$$

These equations imply that, when  $C'_x = 0$  is determined, the value of  $C'_z$  is unique. Physically, it is assumed that slipstream rotation does not have a significant influence on the resultant forces.

Note that the above form implies that if  $C_{T,s}$  is obtained by different combinations of blade angle and advance ratio, the coefficients  $C_x$  and  $C_z$  based on tip speed will vary while  $C'_z$  and  $C'_x$  remain constant.

#### SCALING OF DATA

To interpret the data taken on a model, it is necessary to assume that there are no scale effects. The aerodynamic data from the model may then

be interpreted in two ways. We may consider that there are two scale factors involved, a linear scale factor  $\lambda_L$  and a velocity scale factor  $\lambda_V$ , where

$$\lambda_L = \frac{\text{linear dimension of full-scale aircraft}}{\text{linear dimension of model}}$$

$$\lambda_V = \frac{\text{velocity of full-scale aircraft}}{\text{velocity of model}} .$$

The vertical aerodynamic force of the model or full-scale aircraft may be expressed as:

$$\begin{aligned} Z_M &= \rho A_M (\Omega R)_M^2 C_{Z_M} \\ Z_{fs} &= \rho A_{fs} (\Omega R)_{fs}^2 C_{Z_{fs}} = \rho \lambda_L^2 A_M \lambda_V^2 (\Omega R)_M^2 C_{Z_{fs}} . \end{aligned}$$

The assumption of no scale effects implies that  $C_{Z_M} = C_{Z_{fs}}$ . Then the ratio of the aerodynamic forces will be

$$\frac{Z_{fs}}{Z_M} = \lambda_L^2 \lambda_V^2 .$$

A relation between  $\lambda_L$  and  $\lambda_V$  may be determined from the above expression through the trim condition

$$Z_{fs} = GW_{\text{airplane}},$$

giving

$$\lambda_V = \lambda_L^{-1} \sqrt{\frac{GW}{Z_M}} .$$

The scale factor  $\lambda_L$  is determined by the size of the model, and  $Z_M$  is measured in the experiment.

The dimensional data may then be interpreted using the two scale factors  $\lambda_L$  and  $\lambda_V$ , and the following relationships result for velocities, forces, and moments:



$$F_{FS} = \lambda_L^2 \lambda_V^2 F_M$$

$$M_{FS} = \lambda_L^3 \lambda_V^2 M_M$$

$$V_{FS} = \lambda_V V_M .$$

Note that the velocity scale factor is determined from the result of an experiment. However, before conducting the experiment, it was necessary to select one of the velocities in the problem, the propeller tip speed. The equivalent full-scale propeller rotational speed is determined by the relationship

$$\Omega_{FS} = \frac{\lambda_V}{\lambda_L} \Omega_M .$$

By eliminating the velocity scale factor, we obtain a relationship of the following form:

$$\Omega_{FS} = \lambda_L^{-2} \sqrt{\frac{GW}{Z_M}} \Omega_M .$$

The model data may be precisely interpreted through this relationship, resulting in an equivalent full-scale RPM corresponding to any desired full-scale gross weight, with no assumptions other than the absence of scale effects.

If we are conducting experiments to measure only aerodynamic forces, and are not concerned with scale effects, then the velocity scale factor may be arbitrarily selected. If, however, we are conducting dynamic model experiments, the Froude number must also be matched (Reference 6). This leads to a relationship between  $\lambda_L$  and  $\lambda_V$  as follows:

$$\text{Froude Number} = \sqrt{\frac{V^2}{lg}}$$

$$\left( \frac{V^2}{lg} \right)_{FS} = \left( \frac{V^2}{lg} \right)_M$$

$$\frac{V_{FS}^2}{g l_{FS}} = \frac{V_M^2}{g l_M}$$

$$\lambda_V = \sqrt{\lambda_L} .$$

It was on this basis that the model RPM was selected for the experiments described in this report. This then implies that one specific value of the model vertical force is required.

The force, moment, and velocity relationships that result from matching the Froude number are:

$$F_{fs} = \lambda_L^3 F_m$$

$$M_{fs} = \lambda_L^4 M_m$$

$$V_{fs} = V_m \lambda_L^{.5} .$$

Complete relationships are given in Table II. If the experimental data on the aerodynamic forces acting on the vehicle are to be interpreted precisely, for any given flight condition, then the value of the vertical aerodynamic force for level flight trim is a given value. The velocity scale factor is then determined when the full-scale aircraft gross weight is selected. Different full-scale gross weights will imply different full-scale propeller rotational speeds. If we select the full-scale gross weight on the basis of the dynamic similitude laws, then the full-scale RPM will be correctly scaled. If, however, the selected gross weight differs from that predicted by dynamic similitude, we may apply the data to full-scale aircraft with a different propeller speed, or to one flying at altitude. These two interpretations are discussed in Appendix III.

It should be noted that if the data is interpreted at a different altitude, no assumption other than the absence of scale effects is required. To interpret the data at different propeller speeds at sea level, it is necessary to assume that propeller blade angle and RPM are interchangeable, and therefore the thrust coefficient based slipstream velocity is the only important parameter.

### APPENDIX III

#### CONVERSION TO FULL SCALE

The results of the model experiments may be converted to correspond to a variety of full-scale vehicles of similar geometry to the model. It is convenient to consider the scaling of the data in two steps. First, the size of the model is accounted for by using the dynamic model scale factors given in Table II.

The full-scale aircraft of interest here has a linear scale factor of 10; however, other scale factors may be selected to correspond to other geometrically similar aircraft of desired size. This scaling will imply a certain gross weight for the full-scale vehicle. Then, the results may be interpreted at other gross weights by varying certain of the parameters involved, maintaining the lift coefficient (or equivalently, the propeller thrust coefficient based on forward speed) constant. As the gross weight is varied, either the forward speed or the ambient air density can be varied to preserve the equilibrium lift coefficient.

These two interpretations, and the appropriate factors to use for gross weight variation, are given in Table III. We consider here only the effects of changes in gross weight; the size considerations have been taken into account.

#### VELOCITY-GROSS WEIGHT CORRESPONDENCE

Maintaining the equilibrium lift coefficient of the vehicle at two different gross weights, at the same altitude, yields the following relationship between flight velocity and gross weight:

$$\frac{W_c}{V_c^2} = \frac{W_D}{V_D^2} .$$

Defining a weight ratio scale factor as

$$\Lambda_w = \frac{W_D}{W_c} ,$$

the velocity is scaled as

$$\frac{V_D}{V_c} = \sqrt{\Lambda_w} .$$

The advance ratio must also be maintained constant, and so this scaling results in a different RPM; i.e.,

$$\frac{\Omega_b}{\Omega_c} = \sqrt{\Lambda_w} .$$

In the case of the experiments conducted,  $\Omega_b$  will not correspond to the full-scale rotational speed of the propeller, since the model RPM was selected on the basis of a proper value of  $\Omega_c$ . However, assuming that advance ratio and blade angle are interchangeable, the data may be applied at other propeller rotational speeds. Scale factors for conversion of the data in this fashion are given in Table III.

#### AIR DENSITY-GROSS WEIGHT CORRESPONDENCE

Alternately, the lift coefficient may be maintained constant by varying ambient air density in proportion to gross weight:

$$\frac{W_c}{\rho_c} = \frac{W_b}{\rho_b} .$$

Then the data may be interpreted on this basis where the aerodynamic forces will vary by the scale factor  $\Lambda_w$  and the reduced gross weight will be equivalent to flight at a different altitude given by

$$\frac{\rho_b}{\rho_c} = \Lambda_w .$$

In this case, note that

$$V_b = V_c .$$

The scale factors for conversion by this method are also given in Table III.

In this case it may be observed that there will be no change in the dynamic stability characteristics of the aircraft. This result indicates that in many cases it is desirable, for comparison with flight test, to test a model that is overweight on the basis of the dynamic scaling law, since the flight test experiments will always be conducted at altitudes above sea level. This correspondence for the various experiments conducted here is shown in Figure 22.

#### APPENDIX IV

##### EFFECT ON CENTER-OF-GRAVITY POSITION ON STATIC STABILITY DERIVATIVES

The relationship between the pitching moment about the center-of-gravity position given in this report (9-percent MAC) and any other center-of-gravity position is given by

$$M_x = M_{.09} - (x_{cg} - 0.09\bar{c}) Z$$

$$M_x = M_{.09} - \bar{c} \left( \frac{x_{cg}}{\bar{c}} - 0.09 \right) Z ,$$

where  $\bar{c}$  is the mean aerodynamic chord of the wing.

The two static stability derivatives about this center-of-gravity position will be

$$\frac{\partial M_x}{\partial u} = \frac{\partial M_{.09}}{\partial u} - \bar{c} \left( \frac{x_{cg}}{\bar{c}} - 0.09 \right) \frac{\partial Z}{\partial u}$$

$$\frac{\partial M_x}{\partial \alpha} = \frac{\partial M_{.09}}{\partial \alpha} - \bar{c} \left( \frac{x_{cg}}{\bar{c}} - 0.09 \right) \frac{\partial Z}{\partial \alpha} .$$

The subscript 0.09 will be dropped henceforth, since this is the reference point used in the main body of the report. In terms of derivatives divided by moment of inertia and mass, respectively, we obtain

$$M_{x_u} = M_u - \frac{\bar{c}m}{I_y} \left( \frac{x_{cg}}{\bar{c}} - 0.09 \right) Z_u$$

$$M_{x_\alpha} = M_\alpha - \frac{\bar{c}m}{I_y} \left( \frac{x_{cg}}{\bar{c}} - 0.09 \right) Z_\alpha .$$

The parameter  $\frac{\bar{c}m}{I_y}$  for the full-scale aircraft is computed from

$$\bar{c} = 96.9 \text{ inches} = 8.08 \text{ feet}$$

$$m = 1160 \text{ slugs}$$

$$I_y = 123,000 \text{ slug-ft}^2$$

$$\frac{\bar{c}m}{I_y} = 0.0762$$

so that

$$M_{x_u} = M_u - 0.076 (\bar{x} - 0.09) Z_u$$

$$M_{x_\alpha} = M_\alpha - 0.076 (\bar{x} - 0.09) Z_\alpha .$$

The data presented in two other reports on this same configuration are given at 18-percent MAC (Reference 4) and 24.5-percent MAC (Reference 5).

In hovering, there will be no effect of horizontal center-of-gravity position, since  $Z_u$  is zero. As discussed earlier, it was not possible to obtain a good value for  $Z_w$  in hovering, so it is not possible to compute  $M_w$  as a function of center-of-gravity position; however, it is considered that any effect of  $M_w$  in hovering would be small, due to the fact that when  $Z_u$  is zero the vertical motion is uncoupled from the pitching and horizontal motion.

First, we consider the speed stability. At a wing incidence of  $70^\circ$ , these relationships would be

$$M_{x_u} = 0.012 - 0.076 (\bar{x} - 0.09)(+ 0.085) .$$

Thus, for the center of gravity at 19-percent MAC,

$$M_{x_u} = 0.012 - 0.00065 \cong 0.012 .$$

That is, 10-percent center-of-gravity change would have a negligible effect on the speed stability. At a wing incidence of  $60^\circ$ ,

$$M_{x_u} = - 0.0015 - 0.076 (\bar{x} - 0.09)(- 0.1)$$

$$M_{x_u} = - 0.0015 + 0.00076 = - 0.0008 .$$

In this case, with the initially very small value of the speed stability, moving the center of gravity aft does have a favorable and noticeable effect on the speed stability and, considering only this derivative, would act to reduce the divergence. Moving the center of gravity aft 20-percent would make the speed stability zero in this particular case. At  $40^\circ$  wing incidence,

$$M_{x_u} = 0.005 - 0.076 (\bar{x} - 0.09)(0) .$$

In this case  $Z_u$  is zero, and moving the center of gravity has no effect on this derivative.

Now, let us consider the angle-of-attack stability at an  $i_w = 70^\circ$ :

$$M_{x_\alpha} = + 0.4 - 0.076 (\bar{x} - 0.09)(- 9.2) .$$

For the center of gravity at 19-percent MAC,

$$M_{x_\alpha} = + 0.4 + 0.07 = 0.47 ,$$

so that moving the center of gravity aft will have some small effect in this case. At an  $i_w = 60^\circ$ ,

$$M_{x_\alpha} = + 0.1 - 0.076 (\bar{x} - 0.09)(- 17.8) .$$

For the center of gravity at 19-percent MAC,

$$M_{x_\alpha} = + 0.1 + 0.135 = 0.235 ,$$

so that in this case, again because the initial value is very small, the center of gravity does have an appreciable effect. The maximum lift curve slope has been used in these calculations.

Thus, the position of the center of gravity does have some effect on the stability derivatives; however, the terms are generally rather small and would not result in significant alterations in the dynamics. The most significant effect, at low speeds, of moving the center of gravity would be in changing the value of the required trimming moment. This effect is not considered here.

TABLE I

## COMPARISON OF MODEL AND CORRESPONDING FULL-SCALE CHARACTERISTICS

		Model	FS
Weight, pounds	$i_w = 89^\circ$ :	36.05	36,050
	Other:	46.3	46,300
Wing span, feet		6.75	67.5
Wing area (S), feet squared		5.34	534
Moment of inertia in pitch ( $I_y$ ), slug-feet squared	$i_w = 89^\circ$ :	1.18	118,000
	$i_w = 70^\circ, 60^\circ, 50^\circ$ :	1.23	123,000
	$i_w = 40^\circ$ :	1.28	128,000
Horizontal center-of-gravity location: 9-percent MAC.			



TABLE II

## SCALE FACTORS FOR DYNAMIC MODEL SIMILARITY

Multiply full-scale property by scale factor to obtain model property.

		For $\lambda_L = 10$
Linear dimension	$\lambda_L^{-1}$	.1
Area	$\lambda_L^{-2}$	.01
Volume, mass, force	$\lambda_L^{-3}$	.001
Moment	$\lambda_L^{-4}$	.0001
Moment of inertia	$\lambda_L^{-5}$	.00001
Linear velocity	$\lambda_L^{-.5}$	.316
Linear acceleration	$\lambda_L^0$	1
Angular velocity	$\lambda_L^{.5}$	3.16
Angular acceleration	$\lambda_L$	10
Time	$\lambda_L^{.5}$	.316
Frequency	$\lambda_L^{.5}$	3.16
Reynolds number	$\lambda_L^{-1.5}$	.0316
Mach number	$\lambda_L^{.5}$	.316

$$\text{where } \lambda_L = \frac{\text{full-scale linear dimension}}{\text{model linear dimension}}$$

TABLE III

INTERPRETATION OF FORCES, MOMENTS, AND VELOCITIES AT OTHER GROSS WEIGHTS

To determine aerodynamic quantities at other gross weights, multiply dynamic scaling results by the following quantities:

	altitude-gross weight	velocity-gross weight
Forces	$\Lambda_w$	$\Lambda_w$
Moments	$\Lambda_w$	$\Lambda_w$
Velocities, angular and linear	1	$\Lambda_w^{.5}$
Air density	$\Lambda_w$	1
Angles	1	1

$$\text{where } \Lambda_w = \frac{W_p}{W_c} = \frac{\text{desired gross weight}}{\text{gross weight determined by dynamic scaling}}$$

NOTE: Use of the first column results in no change in dynamic stability characteristics. Use of second column results in changes in dynamics.

TABLE IV

CONVERSION OF DERIVATIVES, STABILITY AXIS DERIVATIVES IN TERMS  
OF SPACE AXIS DERIVATIVES, BOTH AXIS SYSTEMS INITIALLY ALIGNED

Stability Axes	Space Axes
$\frac{\partial X}{\partial u}$	$\frac{\partial X_f}{\partial u_f}$
$\frac{\partial X}{\partial w}$	$\frac{1}{V_0} \left[ \frac{\partial X_f}{\partial \theta_f} - z_0 \right]$
$\frac{\partial Z}{\partial u}$	$\frac{\partial Z_f}{\partial u_f}$
$\frac{\partial Z}{\partial w}$	$\frac{1}{V_0} \frac{\partial Z_f}{\partial \theta_f}$
$\frac{\partial M}{\partial u}$	$\frac{\partial M}{\partial u_f}$
$\frac{\partial M}{\partial w}$	$\frac{1}{V_0} \frac{\partial M}{\partial \theta_f}$
$\frac{\partial M}{\partial \dot{\theta}}$	$\frac{\partial M}{\partial \dot{\theta}_f} + V_0 \frac{\partial M}{\partial \dot{w}_f}$
$\frac{\partial M}{\partial \dot{w}}$	$\frac{\partial M}{\partial \dot{w}_f}$

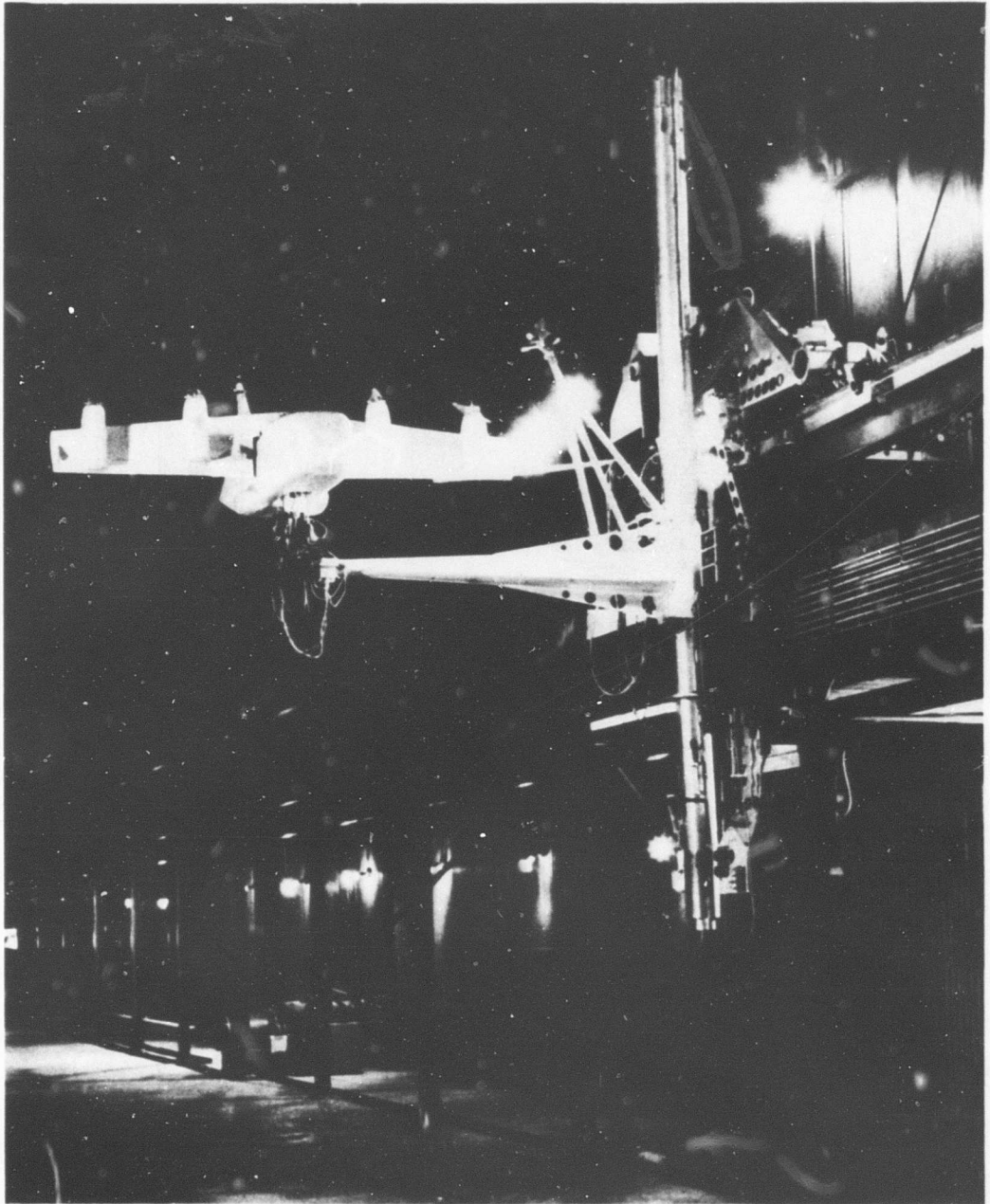


Figure 1. Princeton Dynamic Model Track Longitudinal Mount With One-Tenth Scale Dynamically Similar Model.



NOTE: WING AIRFOIL SECTION NACA 63-318  
 ANGULAR TRAVEL OF VANE =  $1.075 \times$  ANGULAR TRAVEL AT FLAP  
 ALL DIMENSIONS GIVEN IN PERCENT CHORD AT ANY WING STATION

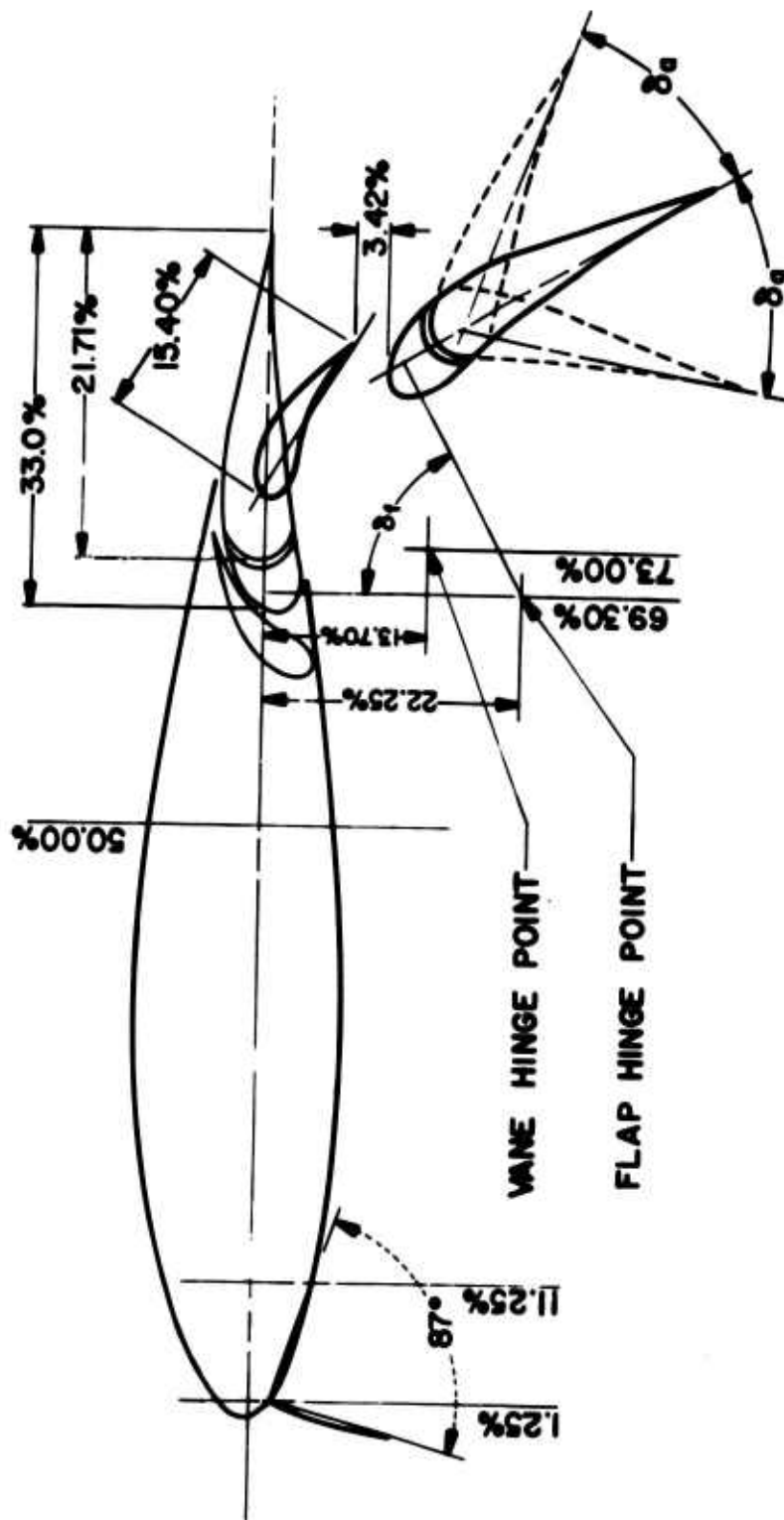
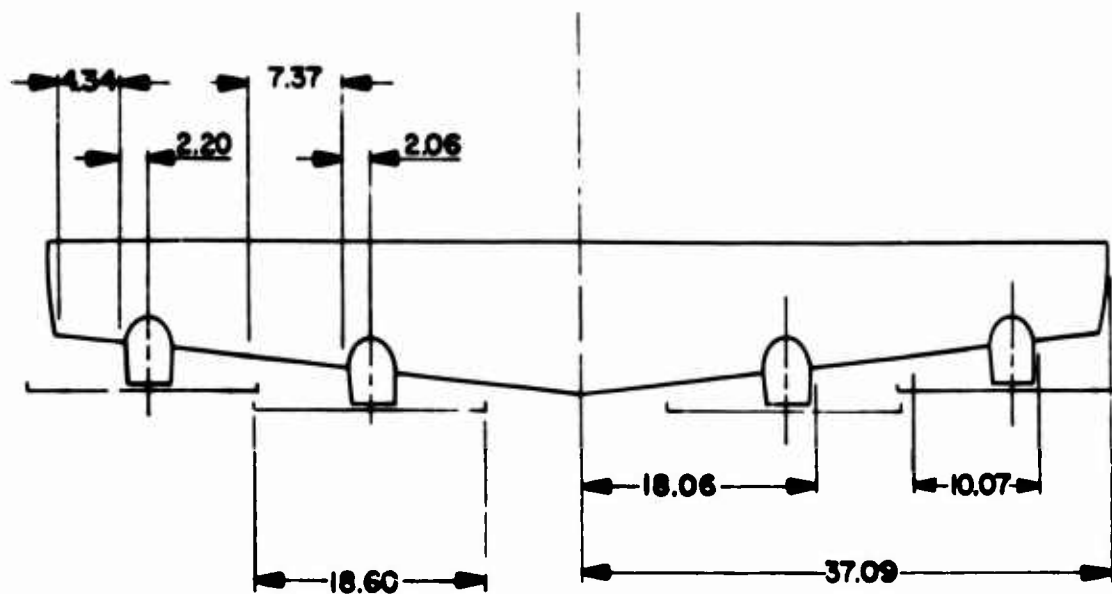


Figure 3a. Flap Arrangement.

**NOTE: LEADING EDGE DEVICES EMPLOYED ONLY  
BEHIND UP-GOING BLADES.**



**Figure 3b. Spanwise Location of Krüger Flaps.**

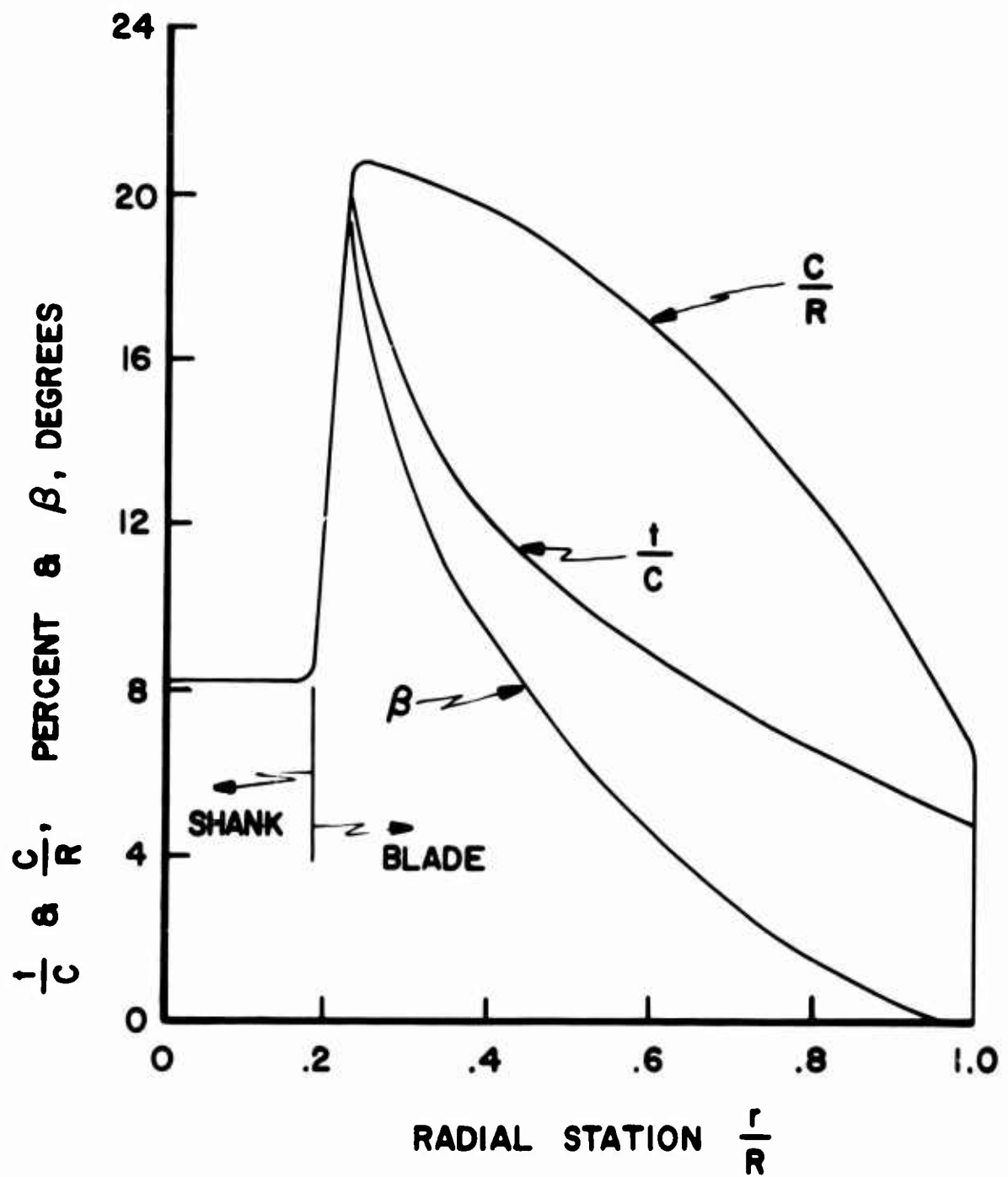


Figure 4. Propeller Blade Characteristics, Four Blades.



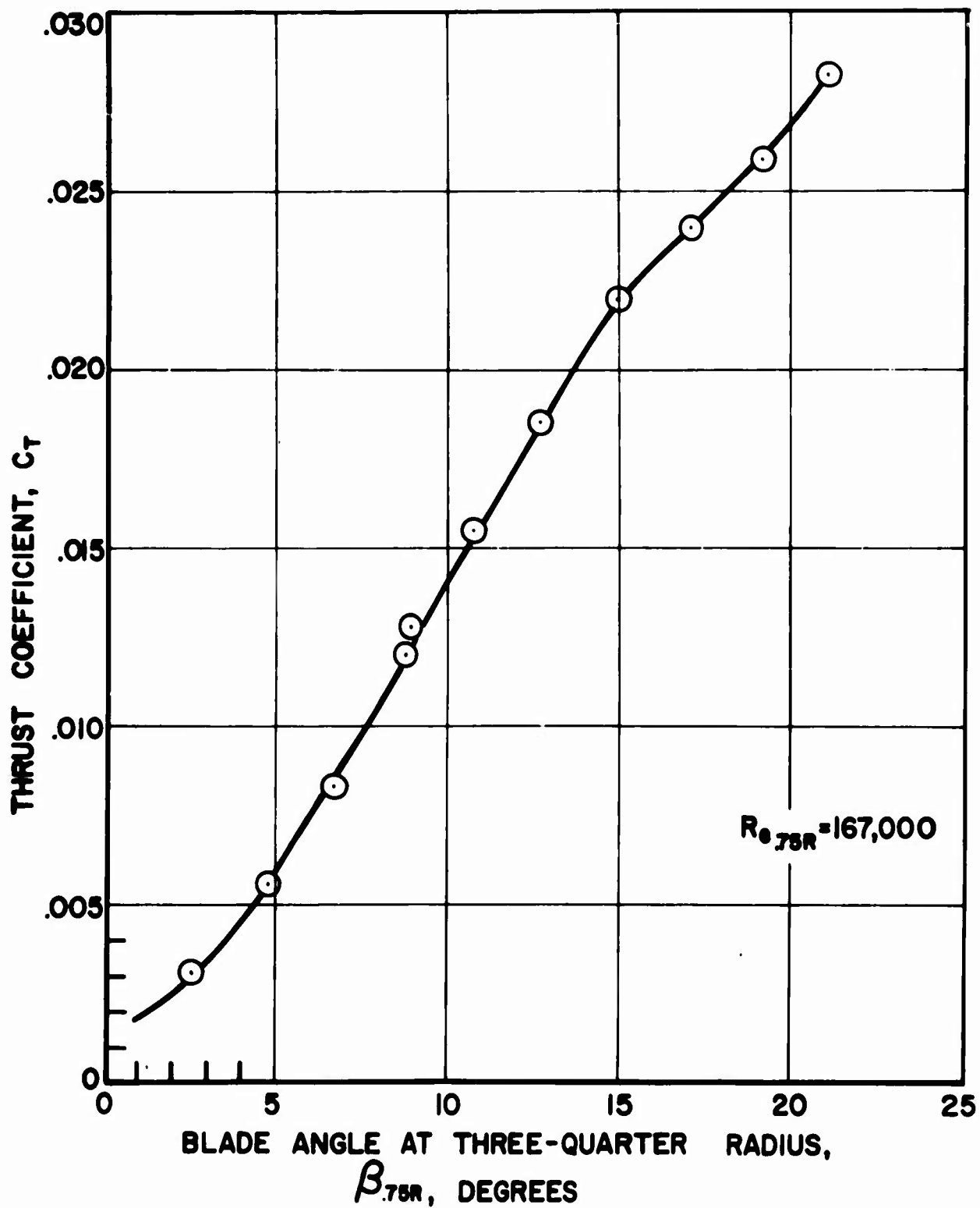


Figure 5. Propeller Static Thrust Characteristics.

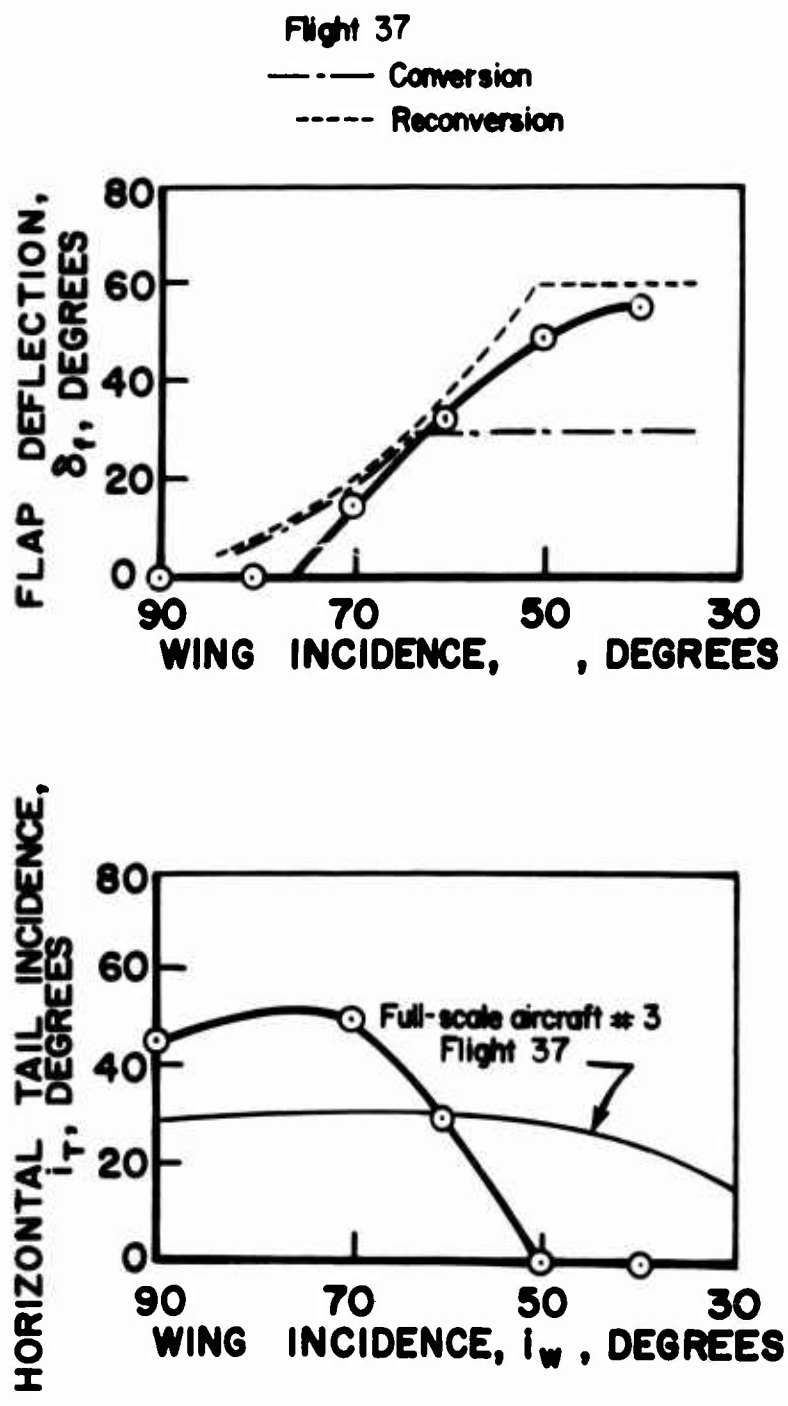


Figure 6. Model and Full-Scale Flap Deflection and Tail Incidence Versus Wing Incidence.

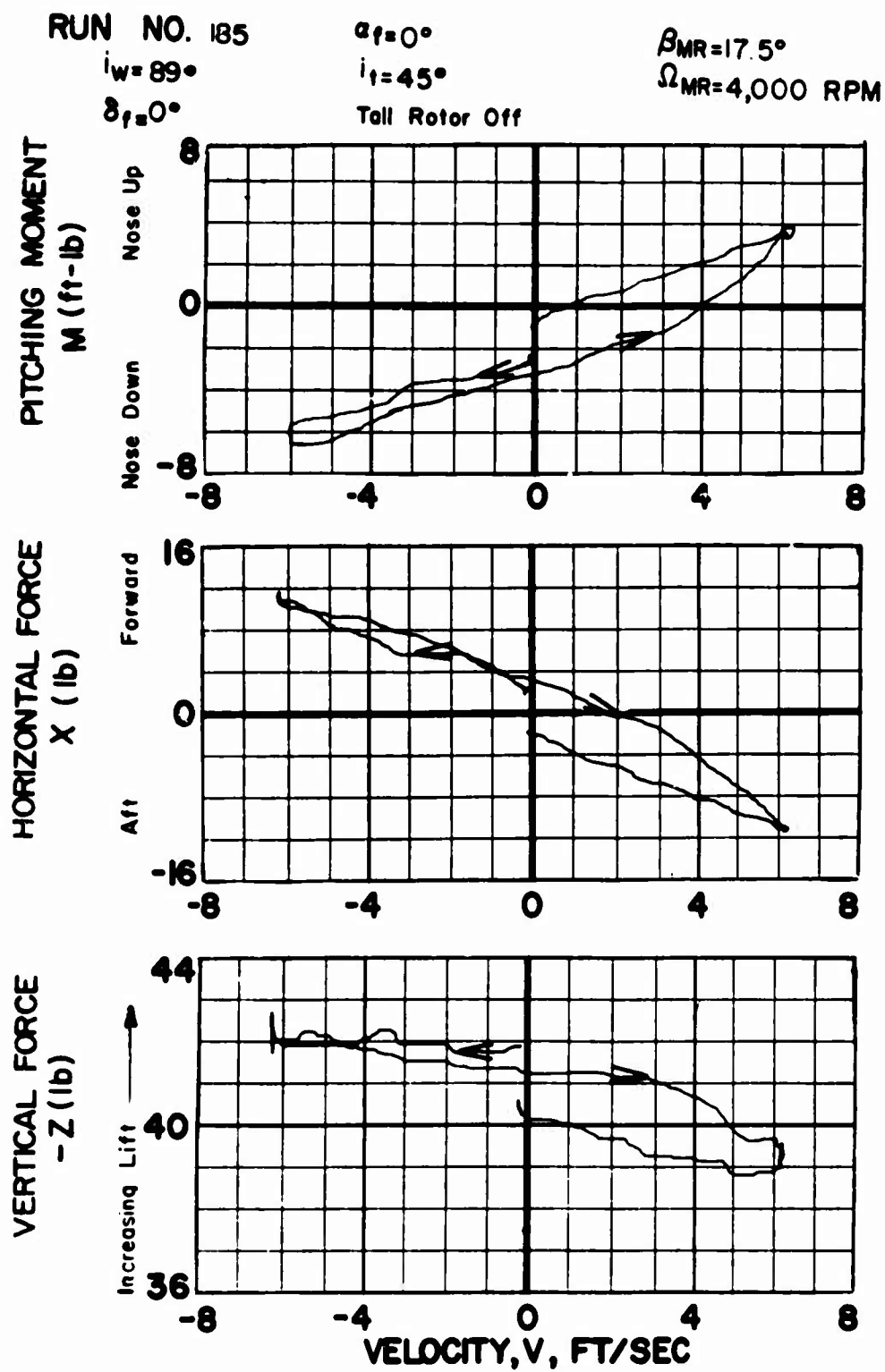


Figure 7a. Static Longitudinal Test Data.

RUN NO. 177

$i_w = 89^\circ$

$\delta_f = 0^\circ$

$\alpha_f = 0^\circ$

$i_t = 45^\circ$

Tail Rotor Off

$\beta_{MR} = 17.5^\circ$

$\Omega_{MR} = 4,000 \text{ RPM}$

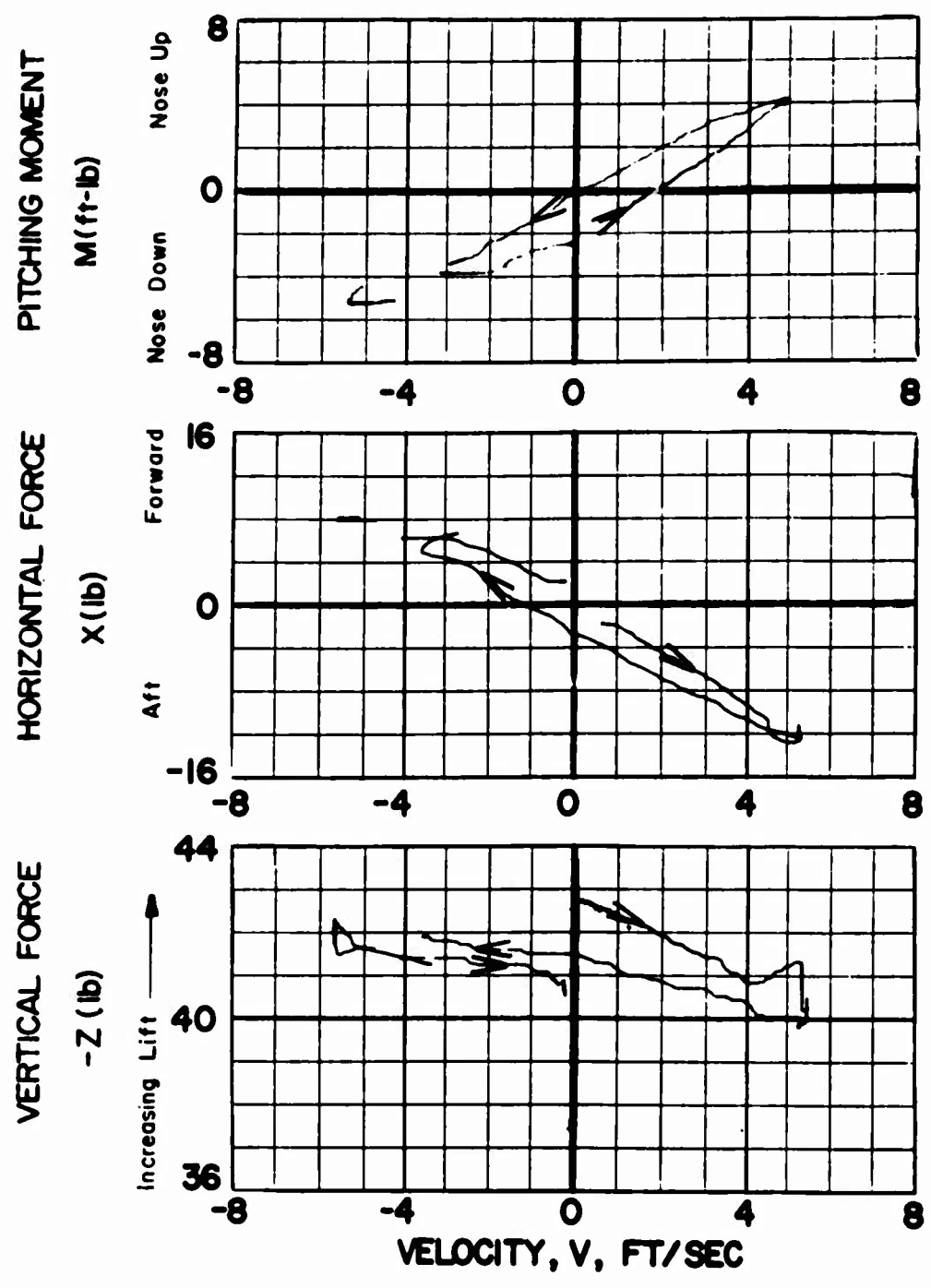


Figure 7b. Static Longitudinal Test Data.

RUN NO. 191

$\alpha_f = 15^\circ$

$\beta_{MR} = 17.5^\circ$

$i_w = 89^\circ$

$i_t = 45^\circ$

$\Omega_{MR} = 4,000 \text{ RPM}$

$\delta_f = 0^\circ$

Tail Rotor Off

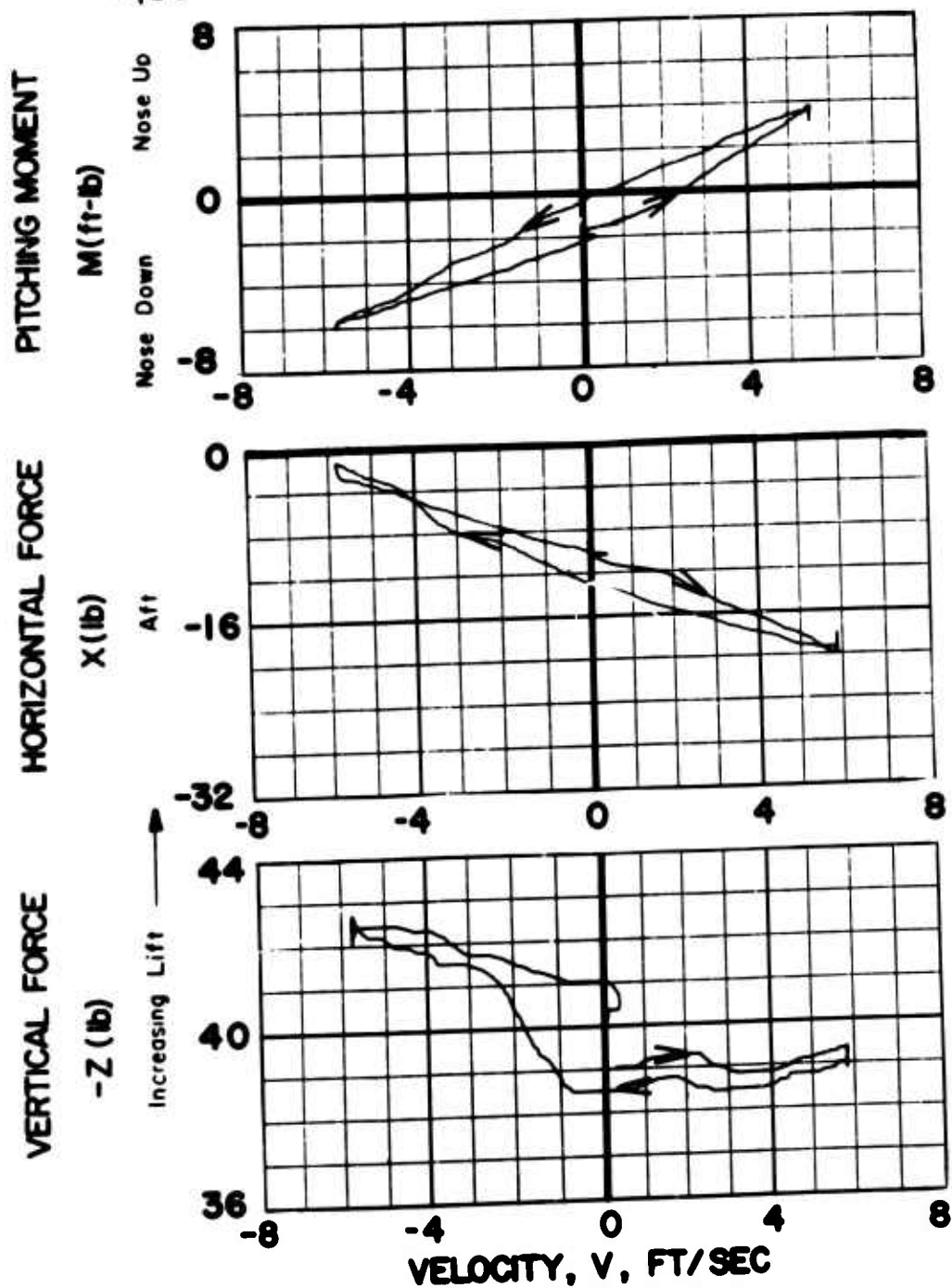


Figure 7c. Static Longitudinal Test Data.

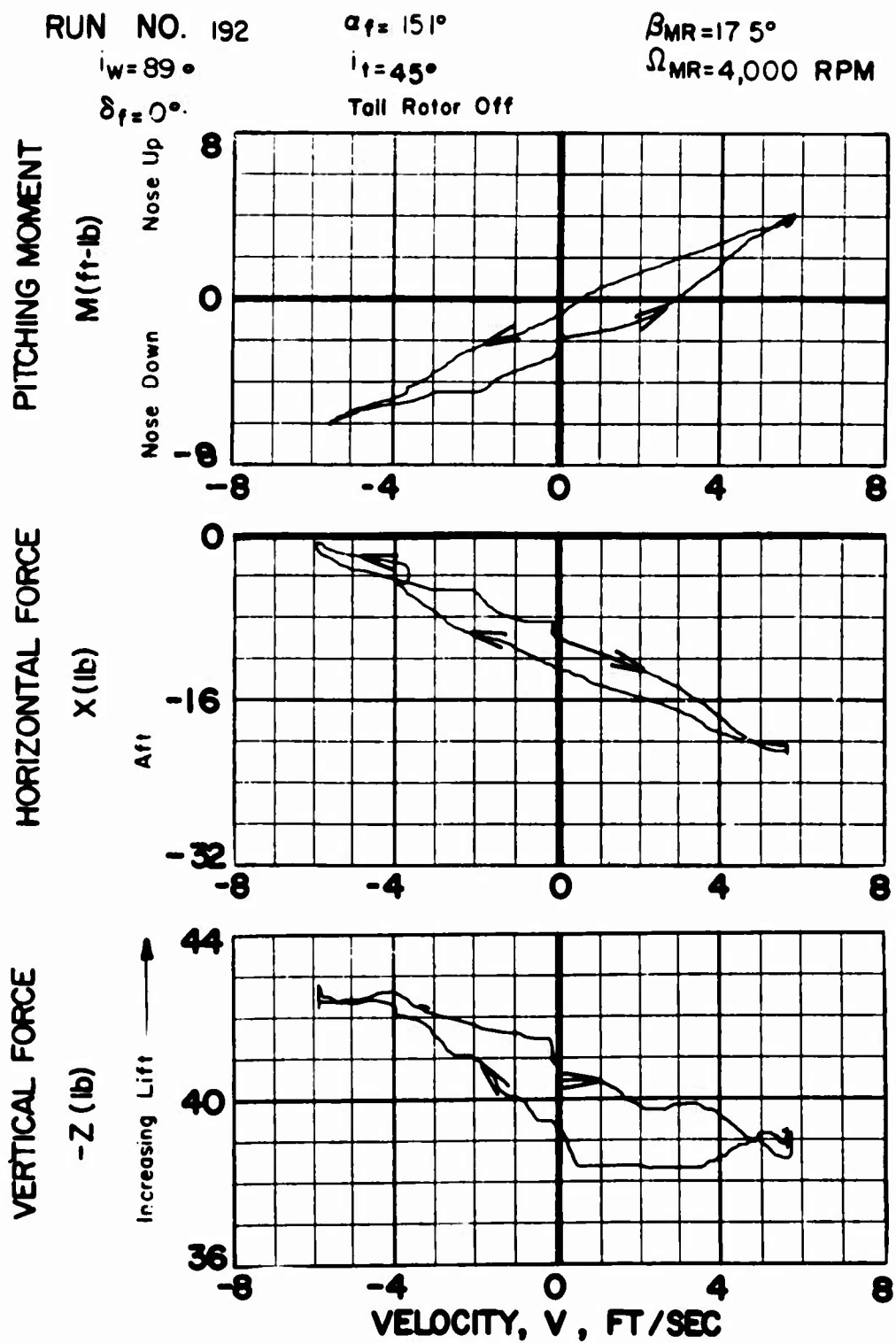


Figure 7d. Static Longitudinal Test Data.

RUN NO. 186

$\alpha_w = 89^\circ$

$\delta_f = 0^\circ$

$\alpha_f = -15.5^\circ$

$i_f = 45^\circ$

Tail Rotor Off

$\beta_{MR} = 17.5^\circ$

$\Omega_{MR} = 4,000 \text{ RPM}$

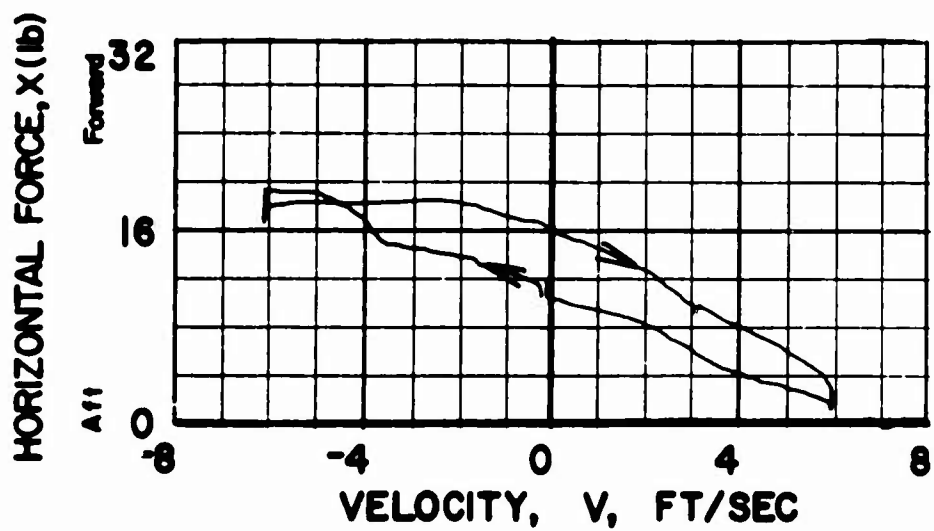
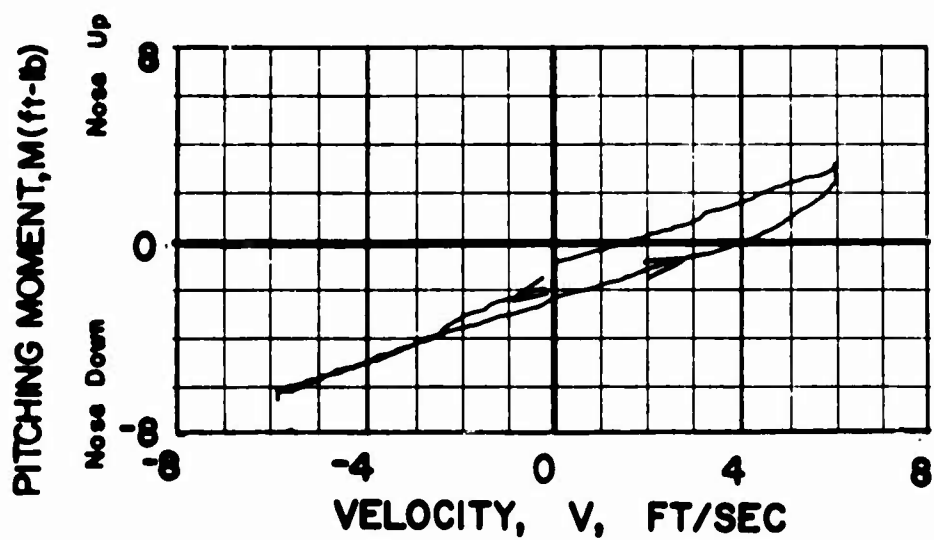


Figure 7e. Static Longitudinal Test Data.

RUN NO. 188

$i_w = 89^\circ$

$\delta_{fz} = 0^\circ$

$\alpha_{fs} = -15.5^\circ$

$i_f = 45^\circ$

Tail Rotor Off

$\beta_{MR} = 17.5^\circ$

$\Omega_{MR} = 4,000 \text{ RPM}$

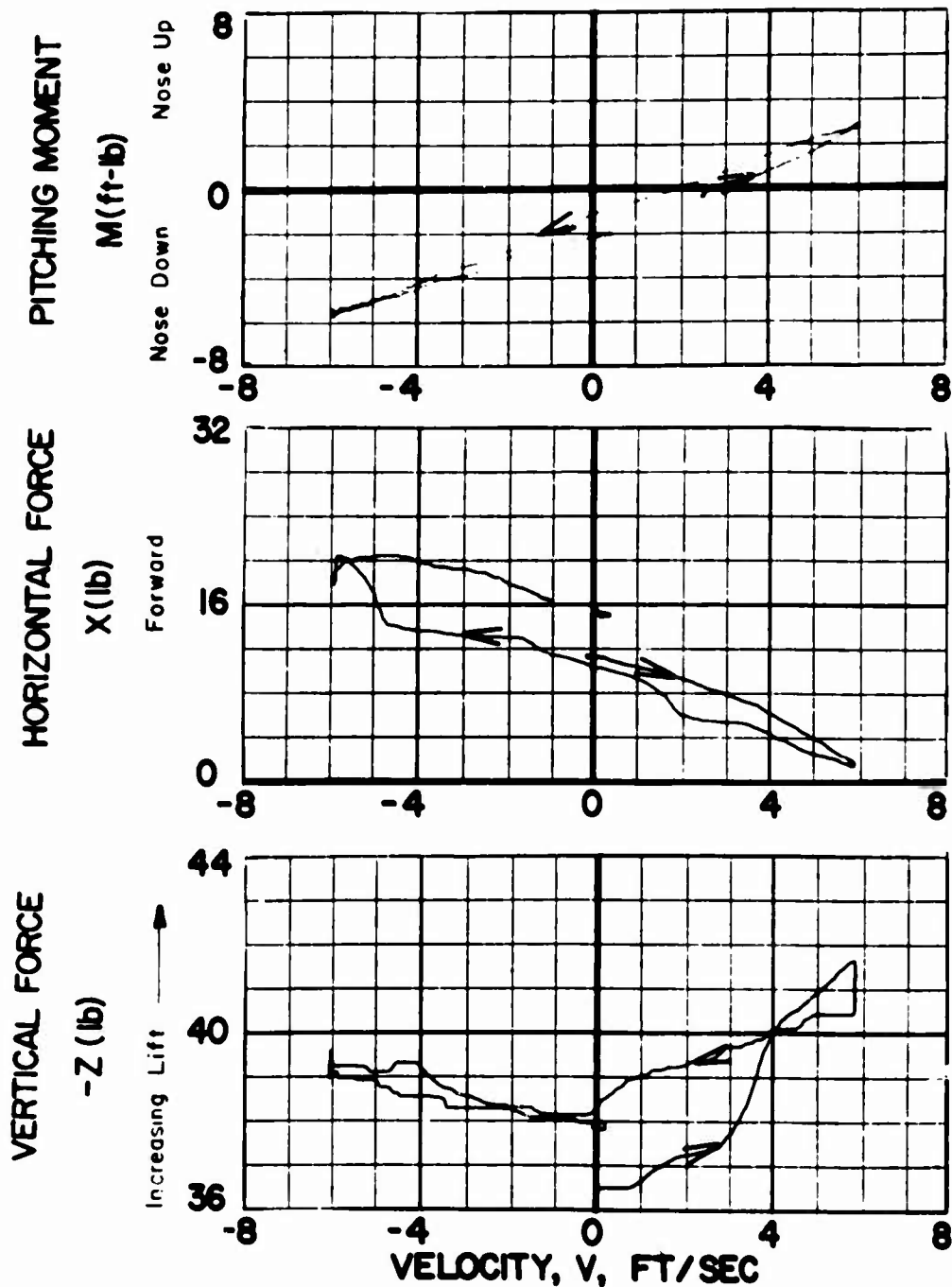


Figure 7f. Static Longitudinal Test Data.



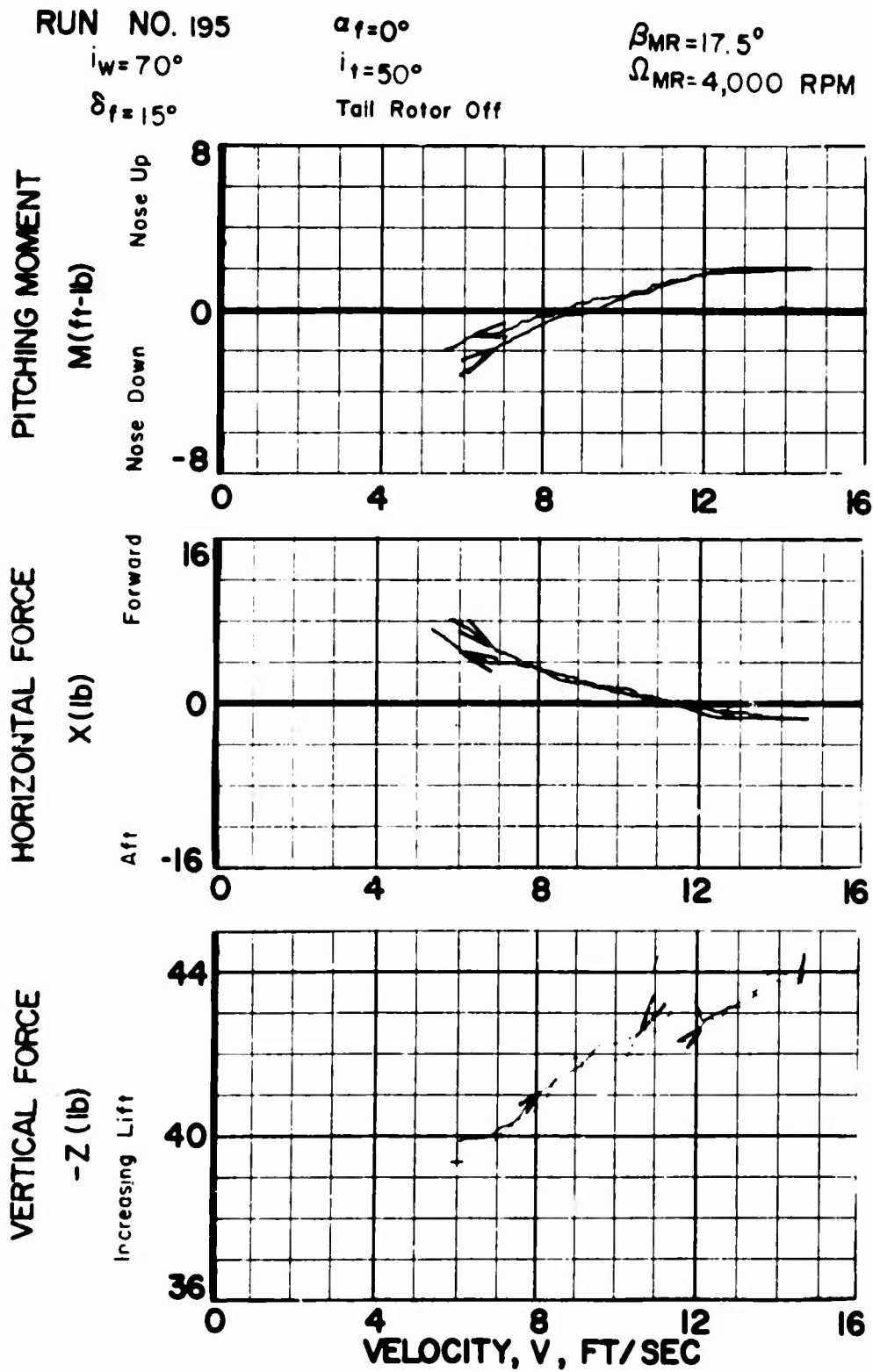


Figure 7g. Static Longitudinal Test Data.

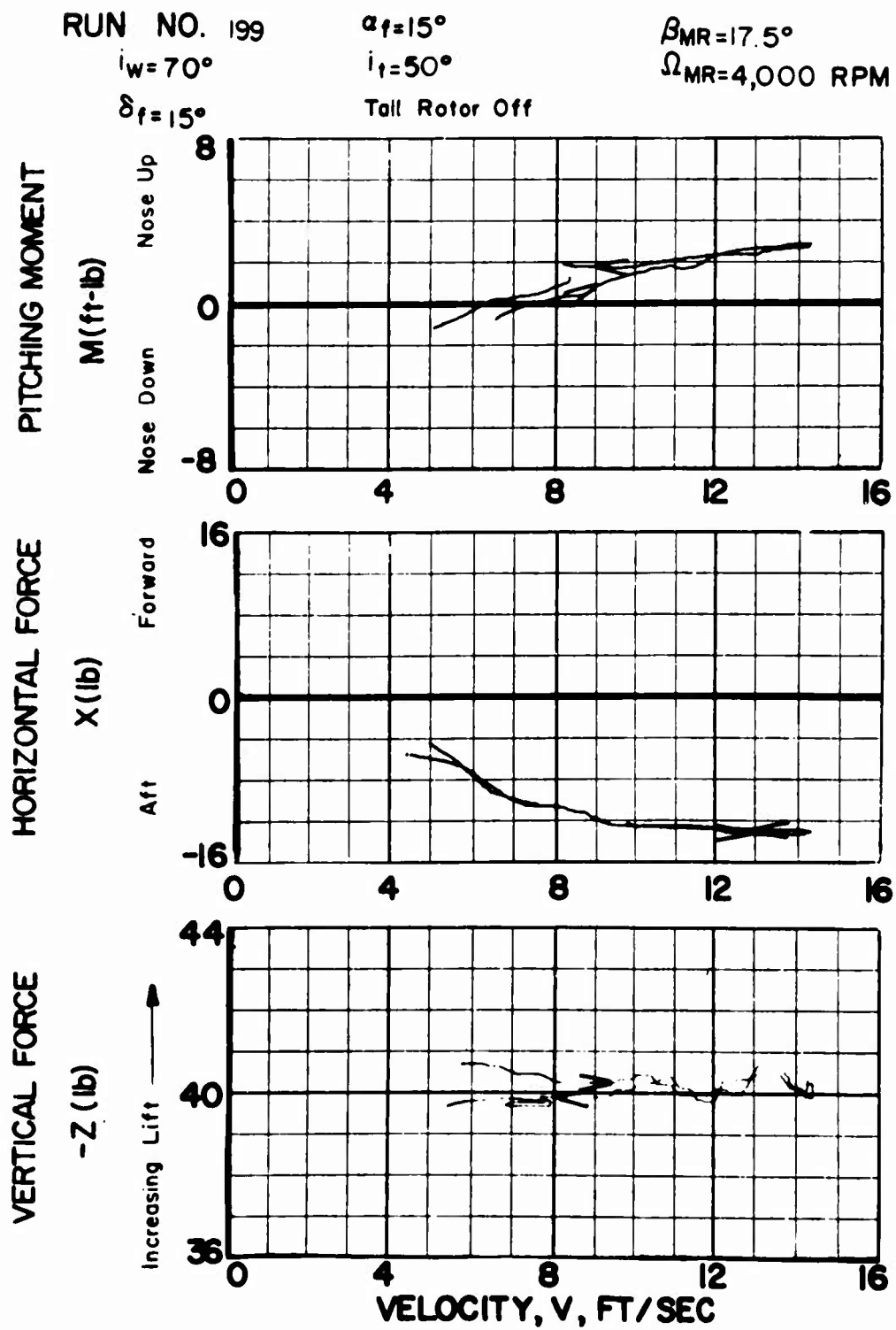


Figure 7h. Static Longitudinal Test Data.

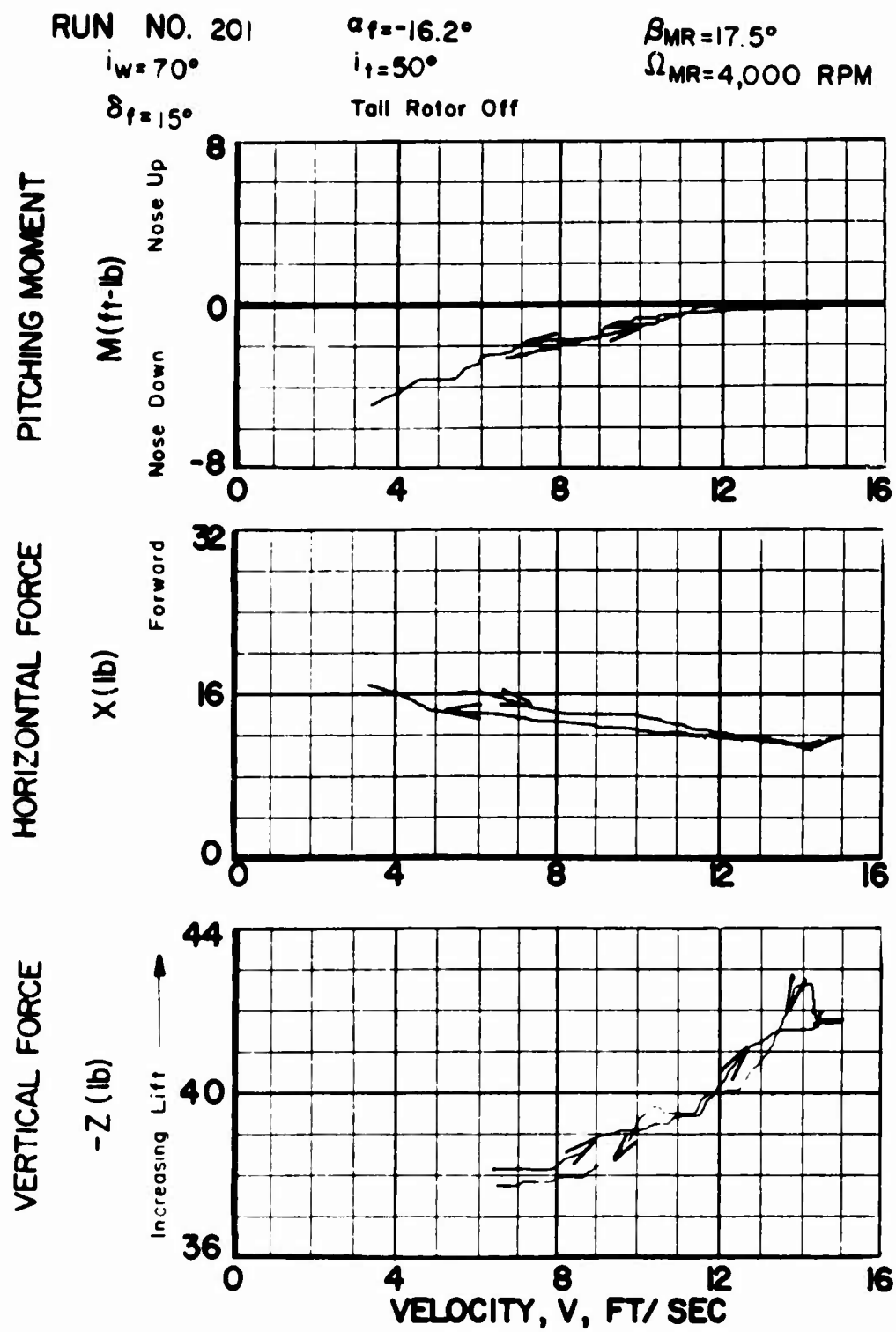


Figure 7i. Static Longitudinal Test Data.

RUN NO. 209

$\alpha_f = 0^\circ$

$\beta_{MR} = 17.5^\circ$

$\delta_w = 60^\circ$

$i_t = 30^\circ$

$\Omega_{MR} = 4,000 \text{ RPM}$

$\delta_f = 32.5^\circ$

Tail Rotor Off

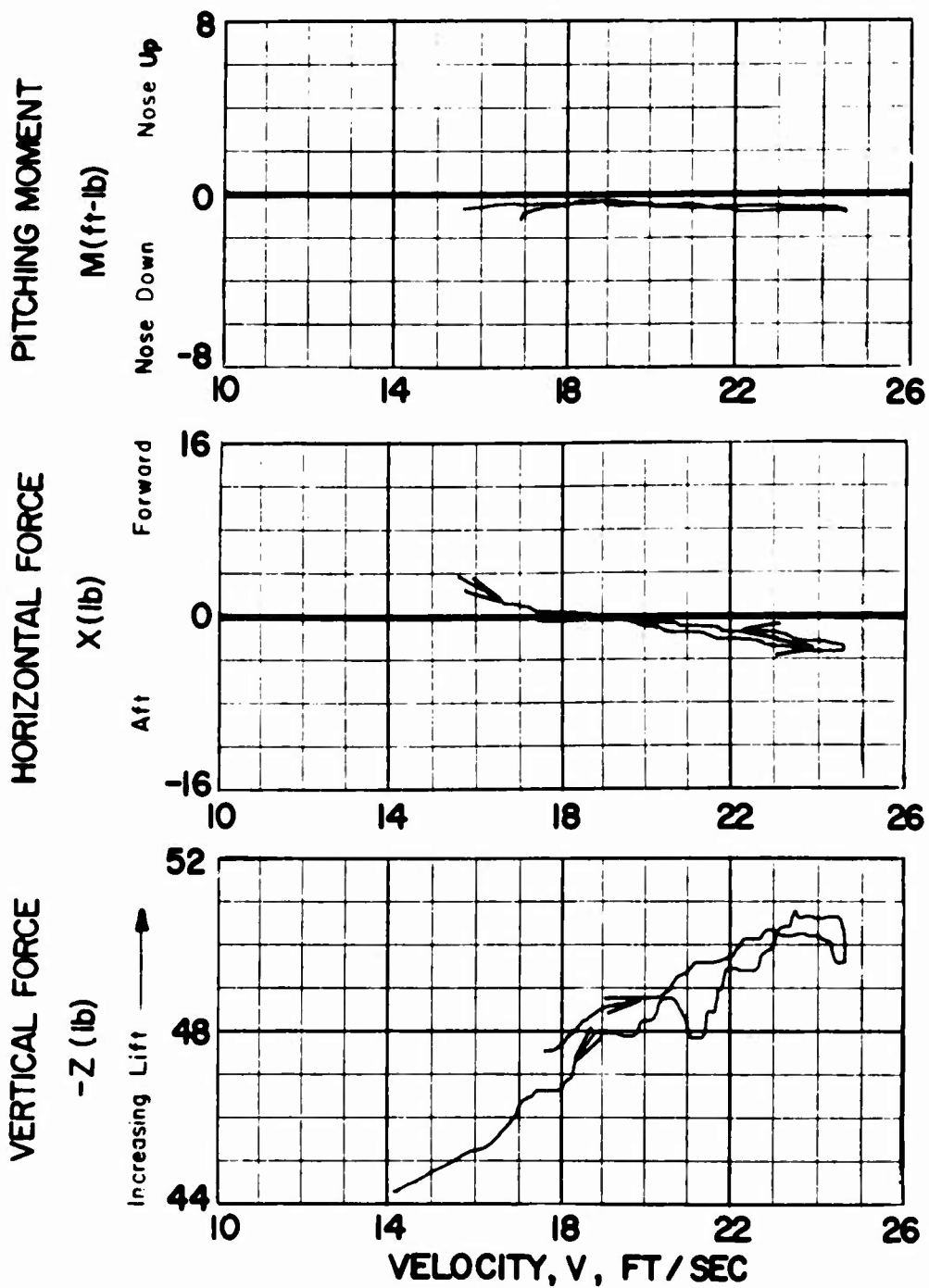


Figure 7j. Static Longitudinal Test Data.

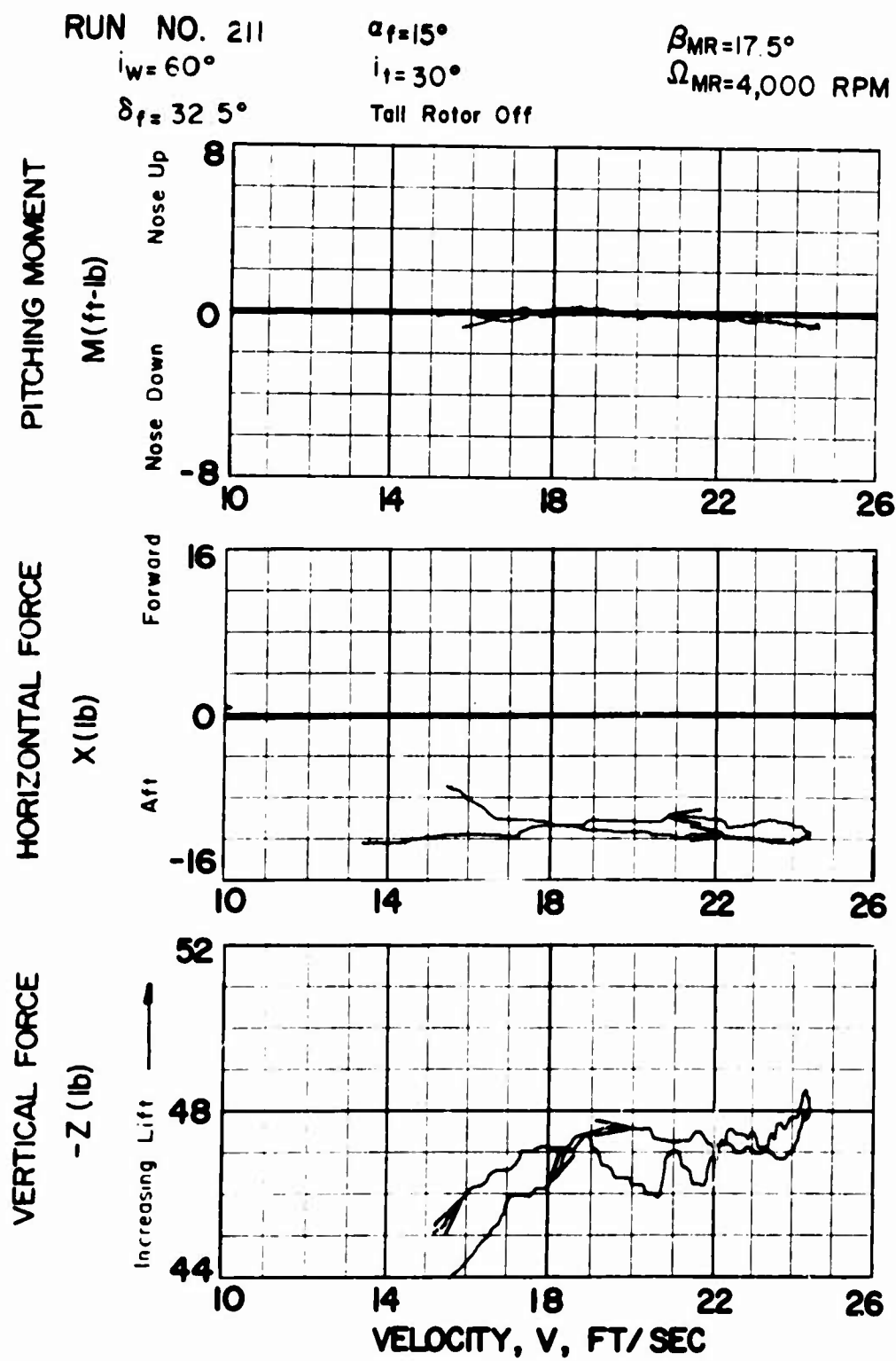


Figure 7k. Static Longitudinal Test Data.

RUN NO. 205

$i_w = 60^\circ$

$\delta_f = 32.5^\circ$

$\alpha_f = -16.2^\circ$

$i_t = 30^\circ$

Tail Rotor Off

$\beta_{MR} = 17.5^\circ$

$\Omega_{MR} = 4,000 \text{ RPM}$

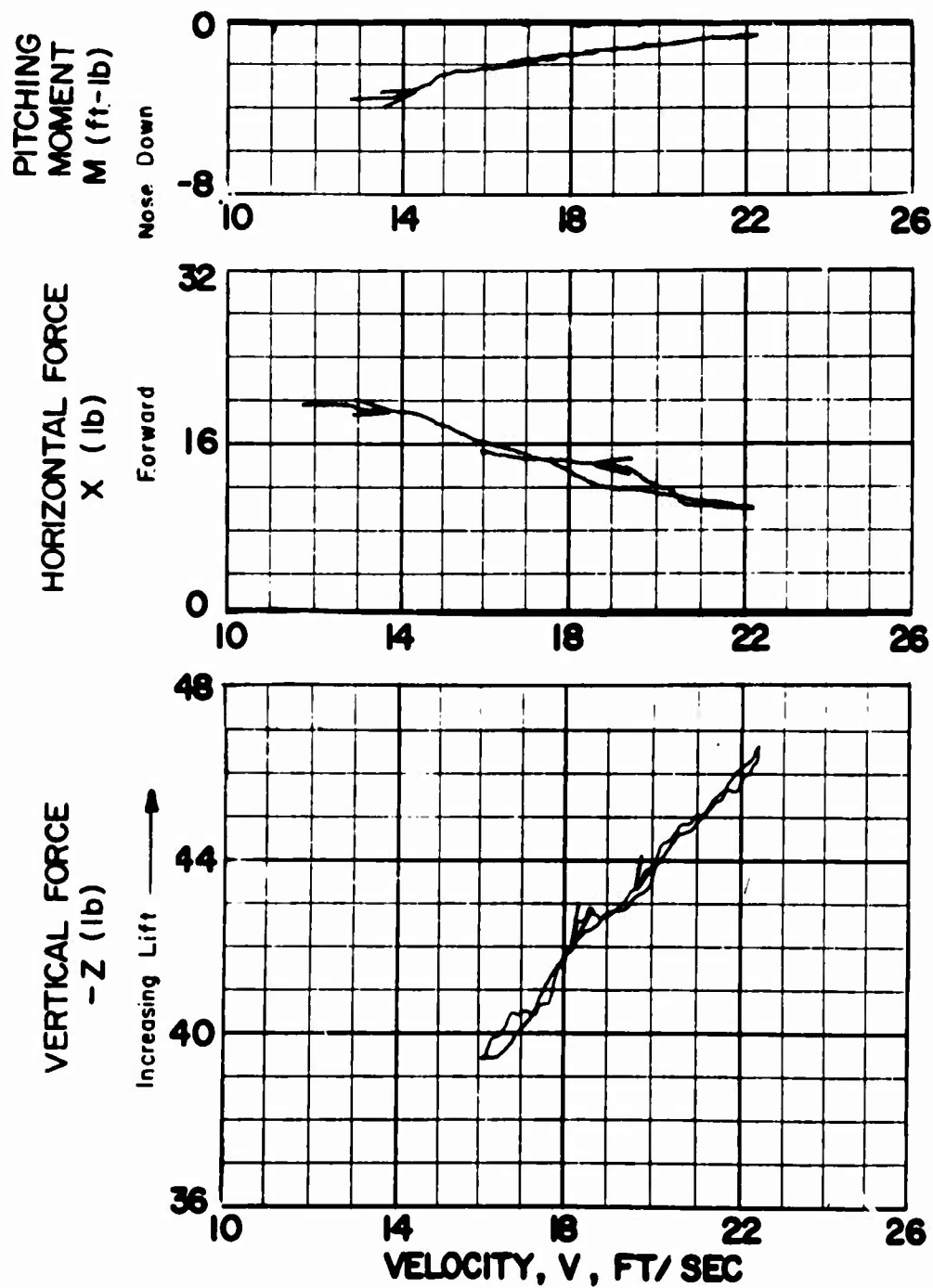


Figure 74. Static Longitudinal Test Data.

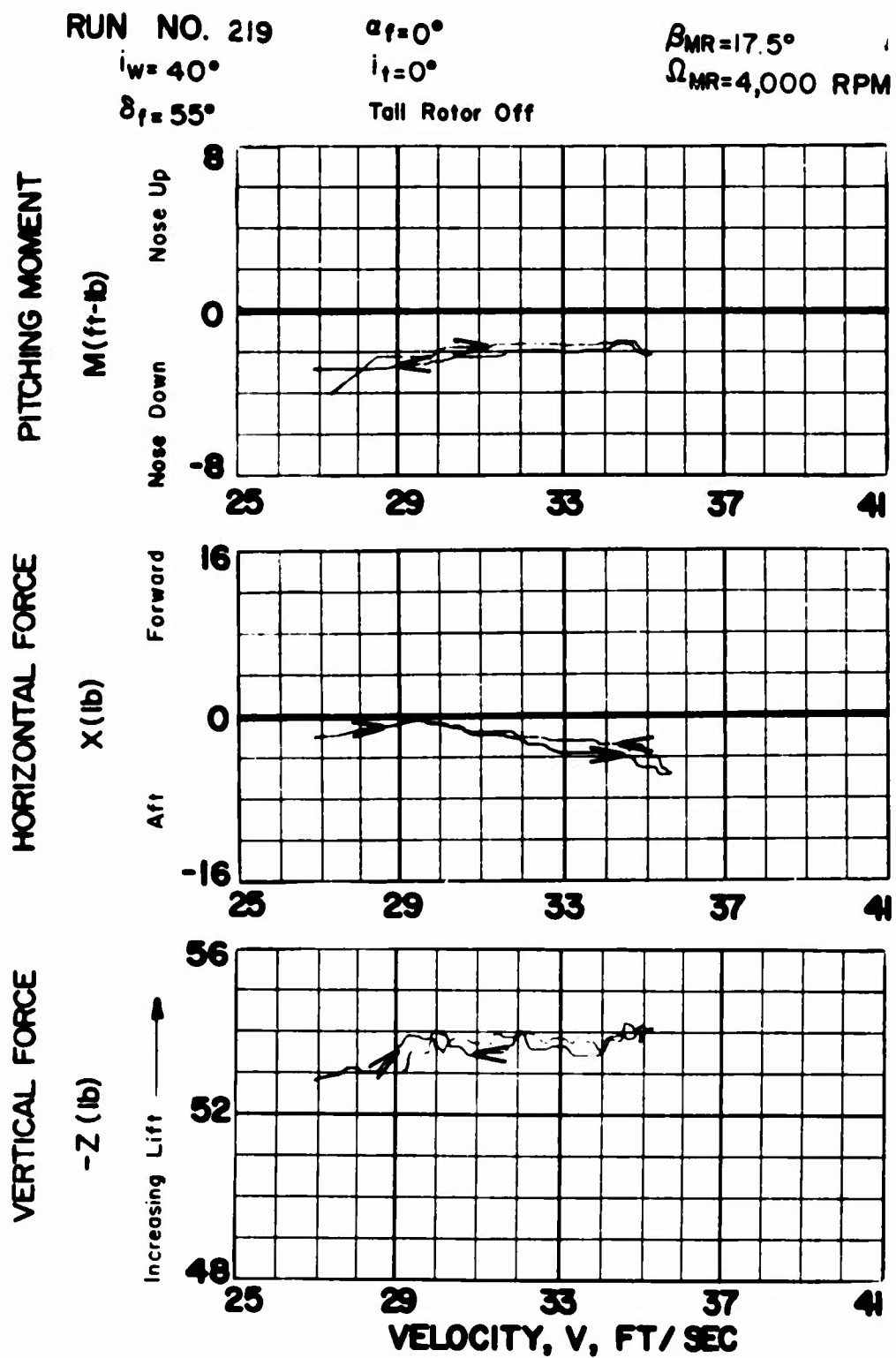


Figure 7m. Static Longitudinal Test Data.

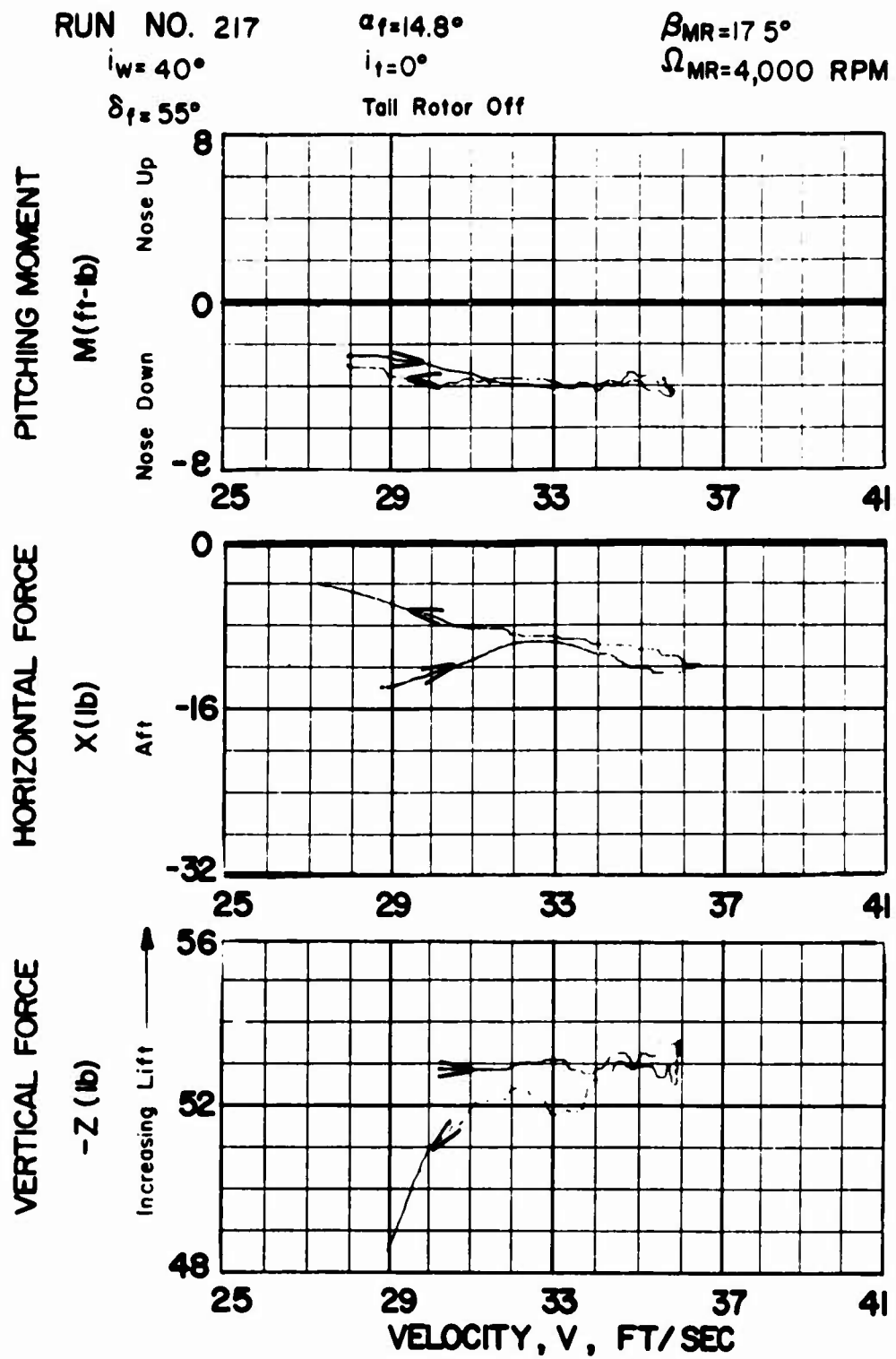


Figure 7n. Static Longitudinal Test Data.



RUN NO. 220

$\alpha_f = -15.9^\circ$

$\beta_{MR} = 17.5^\circ$

$i_w = 40^\circ$

$i_t = 0^\circ$

$\Omega_{MR} = 4,000 \text{ RPM}$

$\delta_f = 55^\circ$

Tail Rotor Off

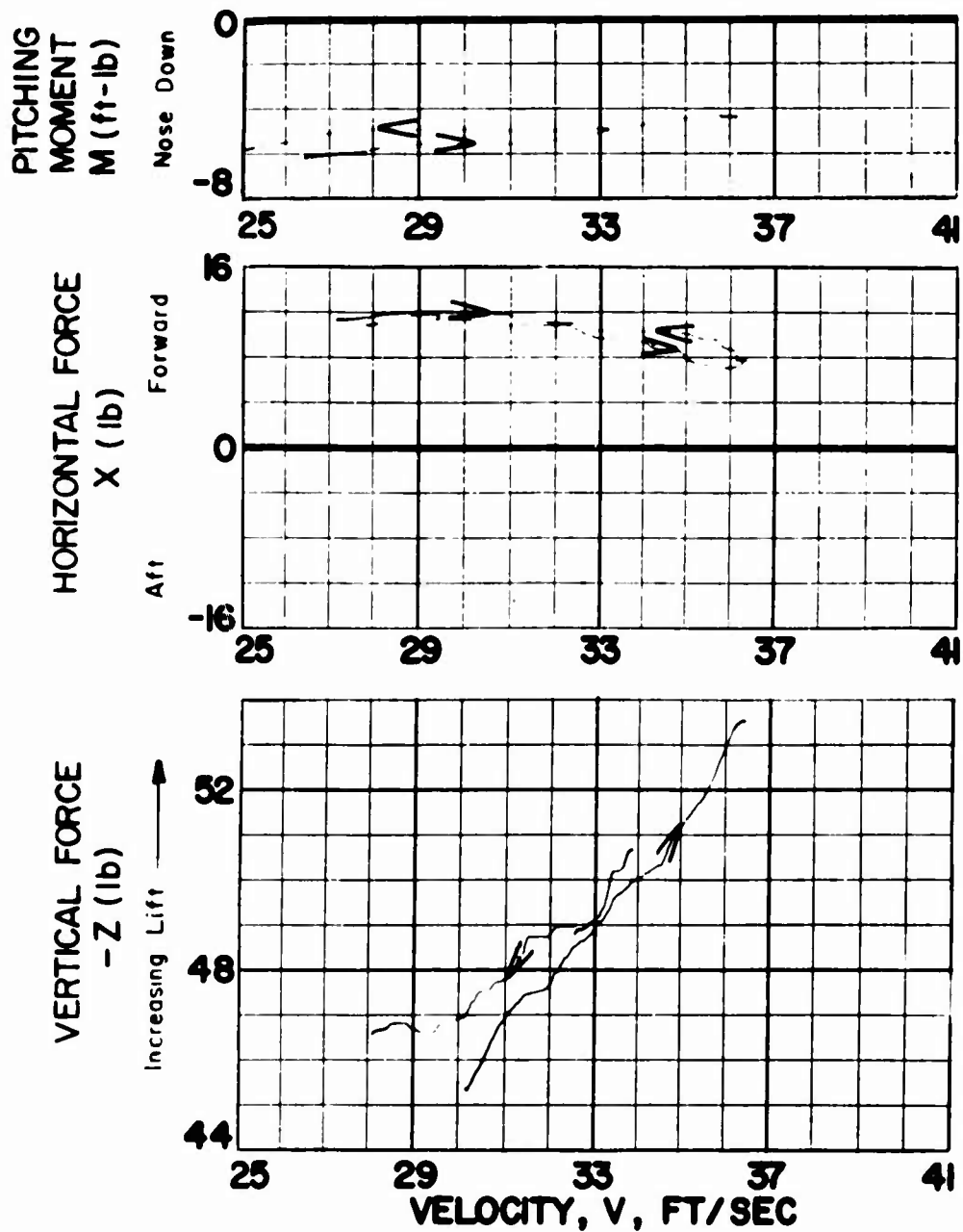


Figure 7a. Static Longitudinal Test Data.

RUN NO. 222

$\alpha_f = 0^\circ$

$\beta_{MR} = 14.8^\circ$

$i_w = 40^\circ$

$i_t = 0^\circ$

$\Omega_{MR} = 4,000 \text{ RPM}$

$\delta_f = 55^\circ$

Tail Rotor Off

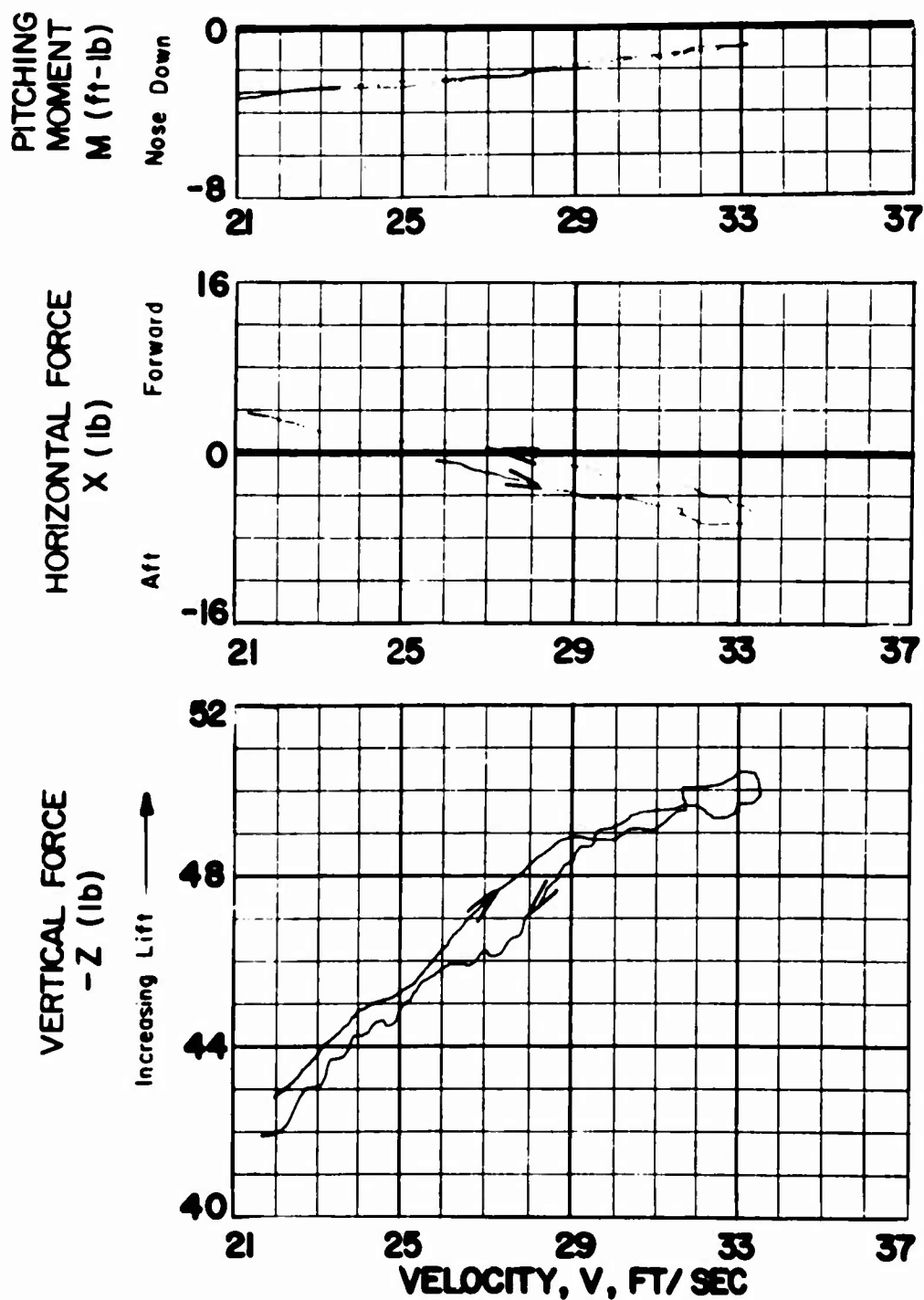


Figure 7p. Static Longitudinal Test Data.

RUN NO. 224

$i_w = 40^\circ$

$\delta_f = 55^\circ$

$\alpha_f = 0^\circ$

$i_f = 0^\circ$

Tell Rotor Off

$\beta_{MR} = 13^\circ$

$\Omega_{MR} = 4,000 \text{ RPM}$

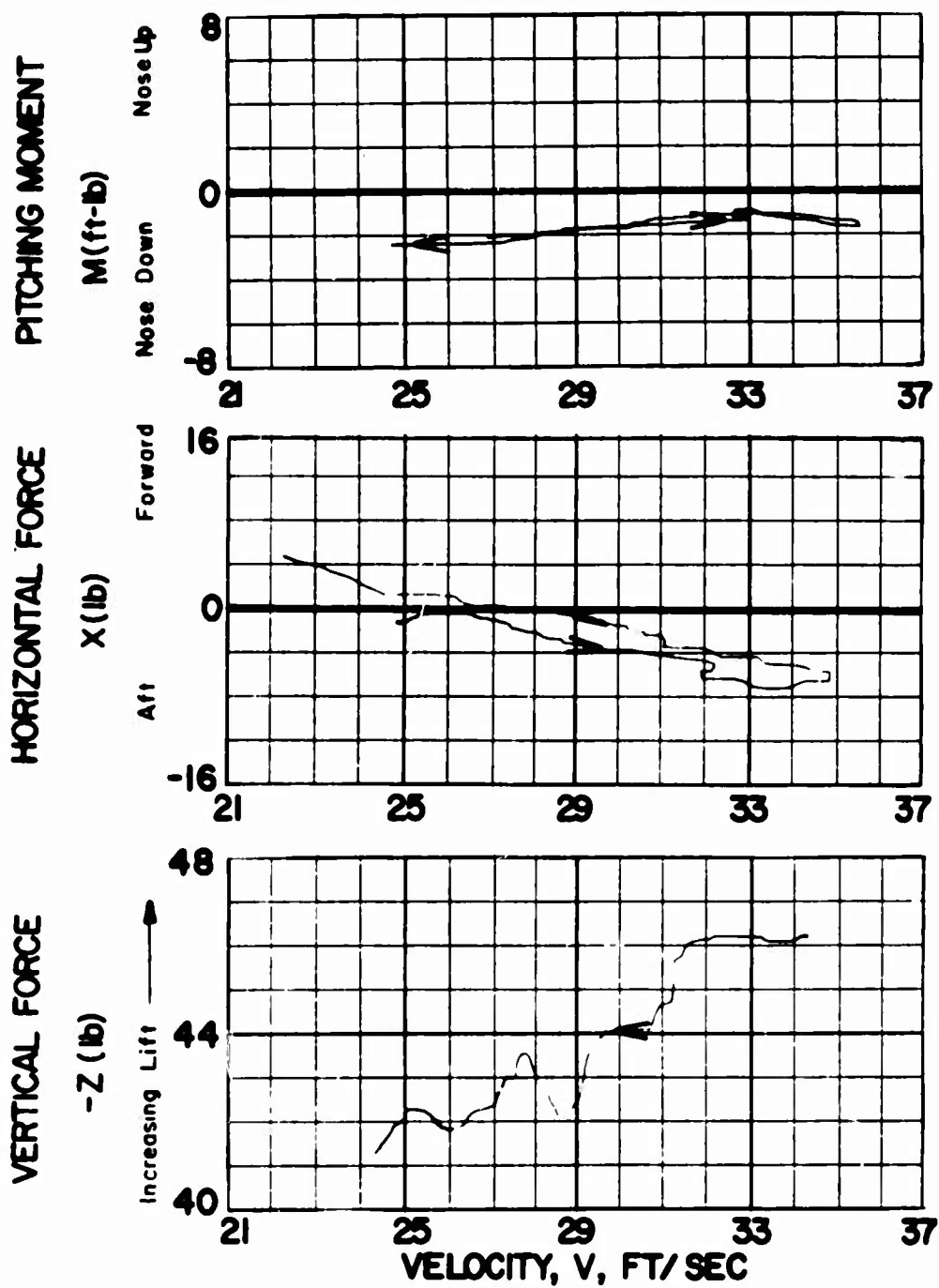


Figure 7q. Static Longitudinal Test Data.

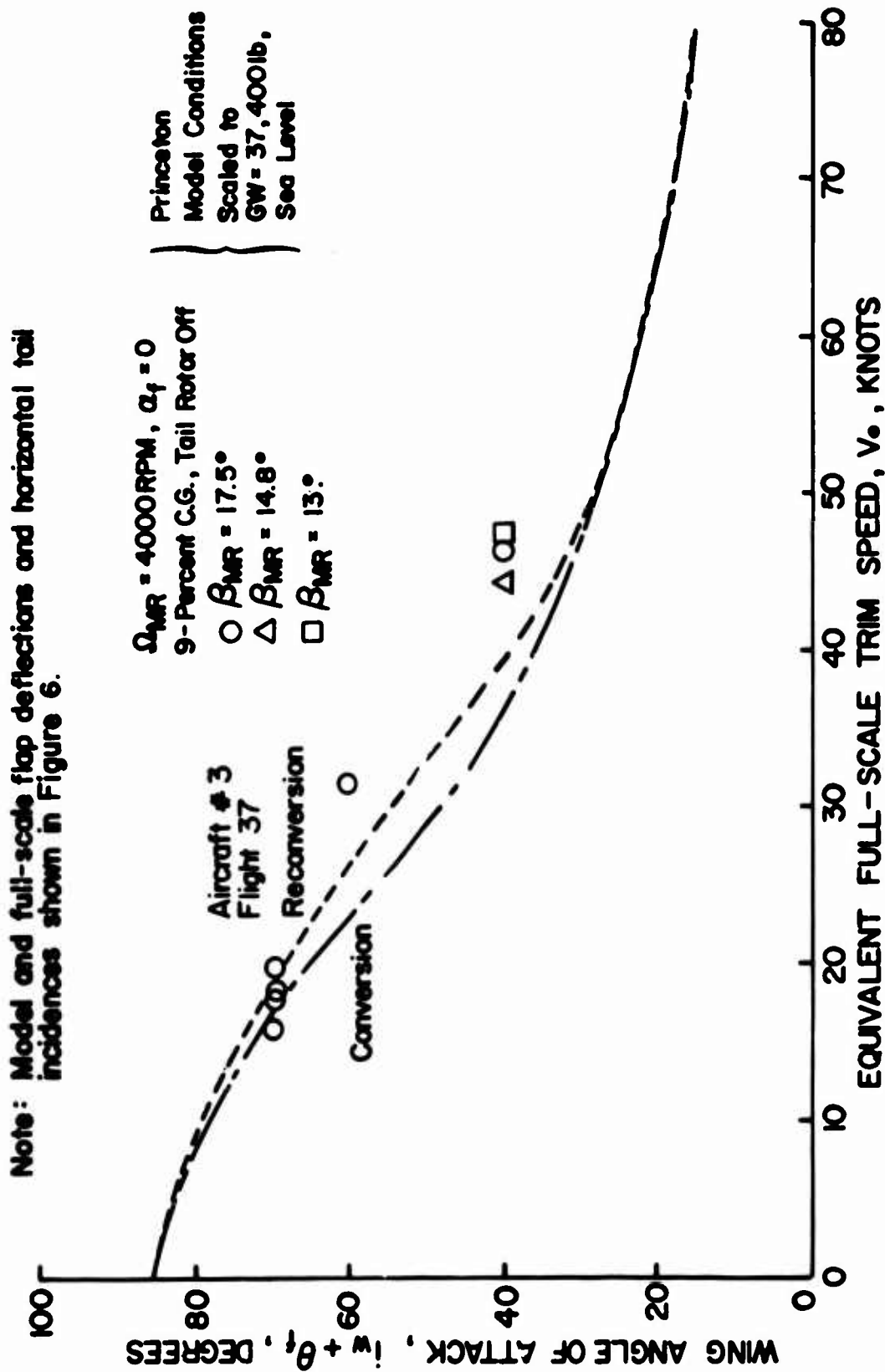


Figure 8a. Comparison of Scaled Model Trim Conditions With Full-Scale Aircraft.

$\circ \beta_{MR} = 17.5^\circ$   
 $\triangle \beta_{MR} = 14.8^\circ$   
 $\square \beta_{MR} = 13.^\circ$   
 $\Omega_{MR} = 4000 \text{ RPM}$

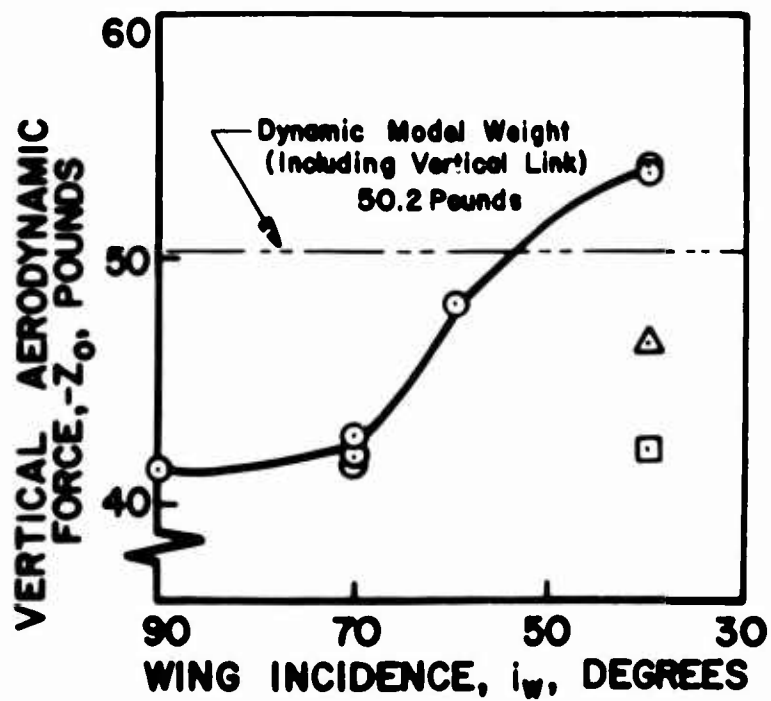


Figure 8b. Model Trim Conditions From Static Data.  
 ( $\theta_f = 0$ ,  $\alpha_f = 0$ , 9-Percent C.G., Tail Rotor Off,  
 $\delta_f$  and  $i_t$  Shown in Figure 6)

$$\odot \beta_{MR} = 17.5^\circ$$

$$\triangle \beta_{MR} = 14.8^\circ$$

$$\square \beta_{MR} = 13^\circ$$

$$\Omega_{MR} = 4000 \text{ RPM}$$

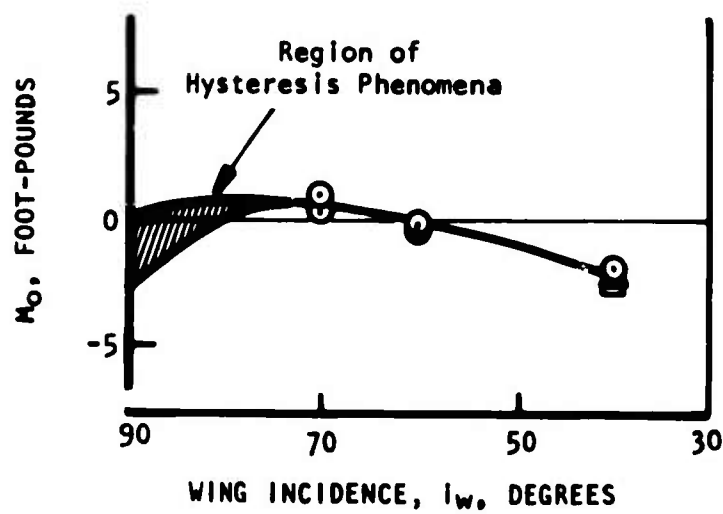


Figure 8c. Unbalanced Model Pitching Moment From Static Data.  
 $(\theta_f = 0, \alpha_f = 0, 9\text{-Percent C.G., Tail Rotor Off,}$   
 $\delta_f$  and it Shown in Figure 6)

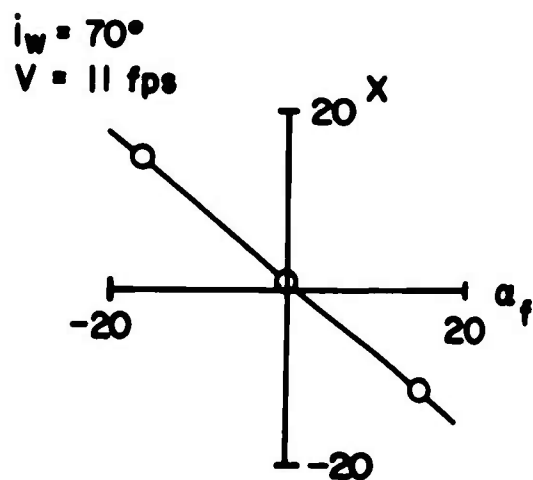
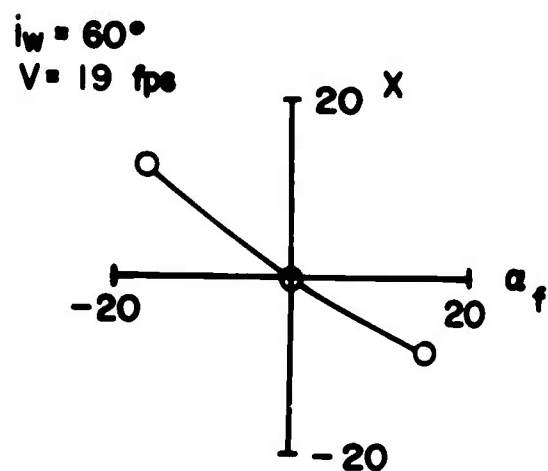
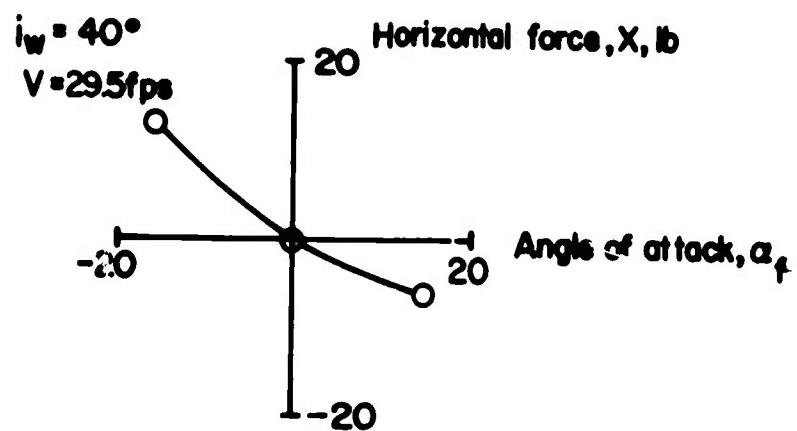


Figure 9a. Variation of Horizontal Force With Angle of Attack.  
 (Tail Rotor Off,  $\beta_{mr} = 17.5^\circ$ ,  $\Omega_{mr} = 4,000 \text{ RPM}$ ,  
 $\alpha_f$  and  $i_t$  Shown in Figure 6)

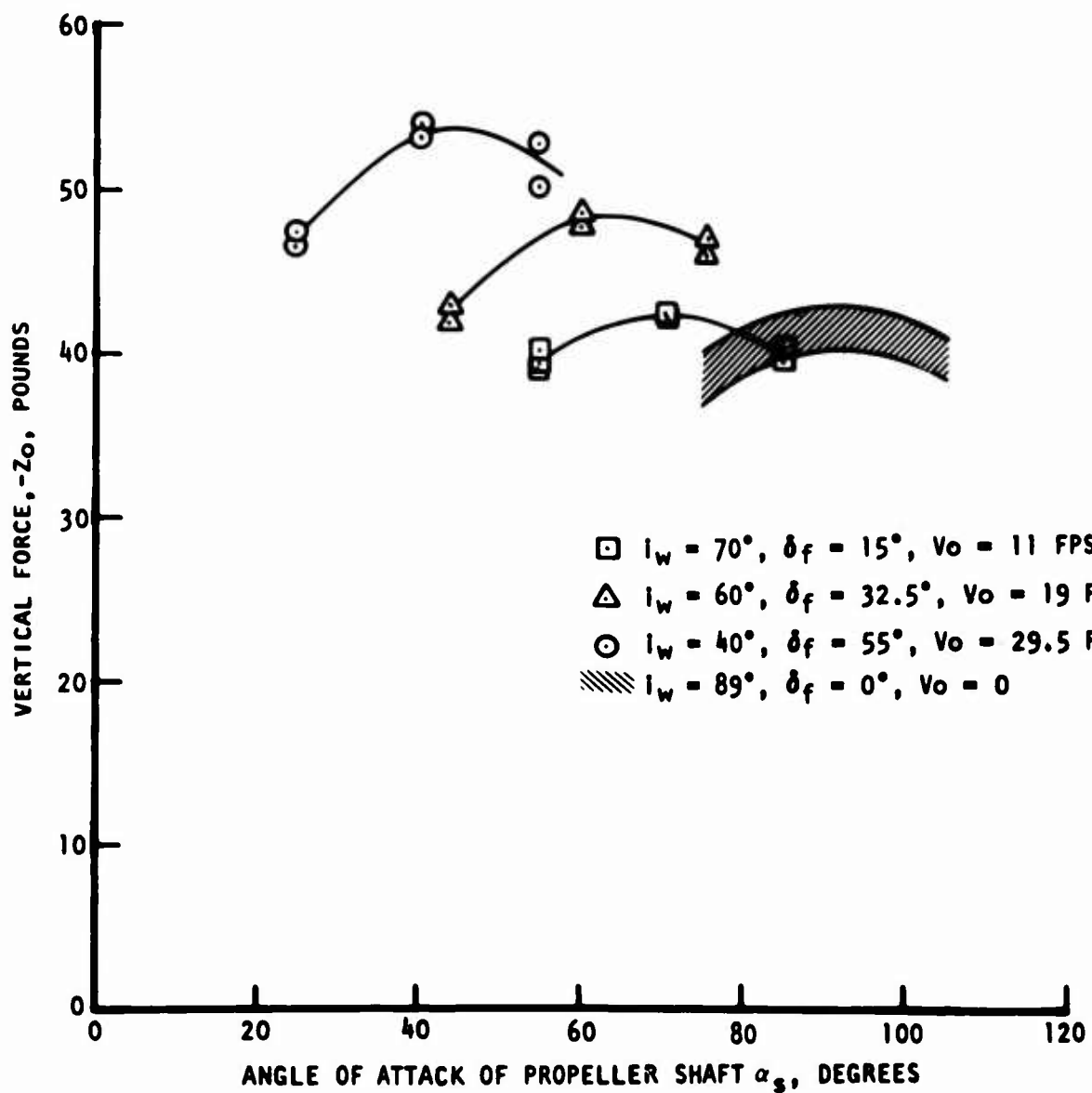


Figure 9b. Variation of Model in Vertical Force With Angle of Attack of Propeller Shaft Near Trim Conditions.  
(Tail Rotor Off,  $\beta_{mr} = 17.5^\circ$ ,  $\Omega_{mr} = 4,000$  RPM,  $i_t$  Shown in Figure 6)



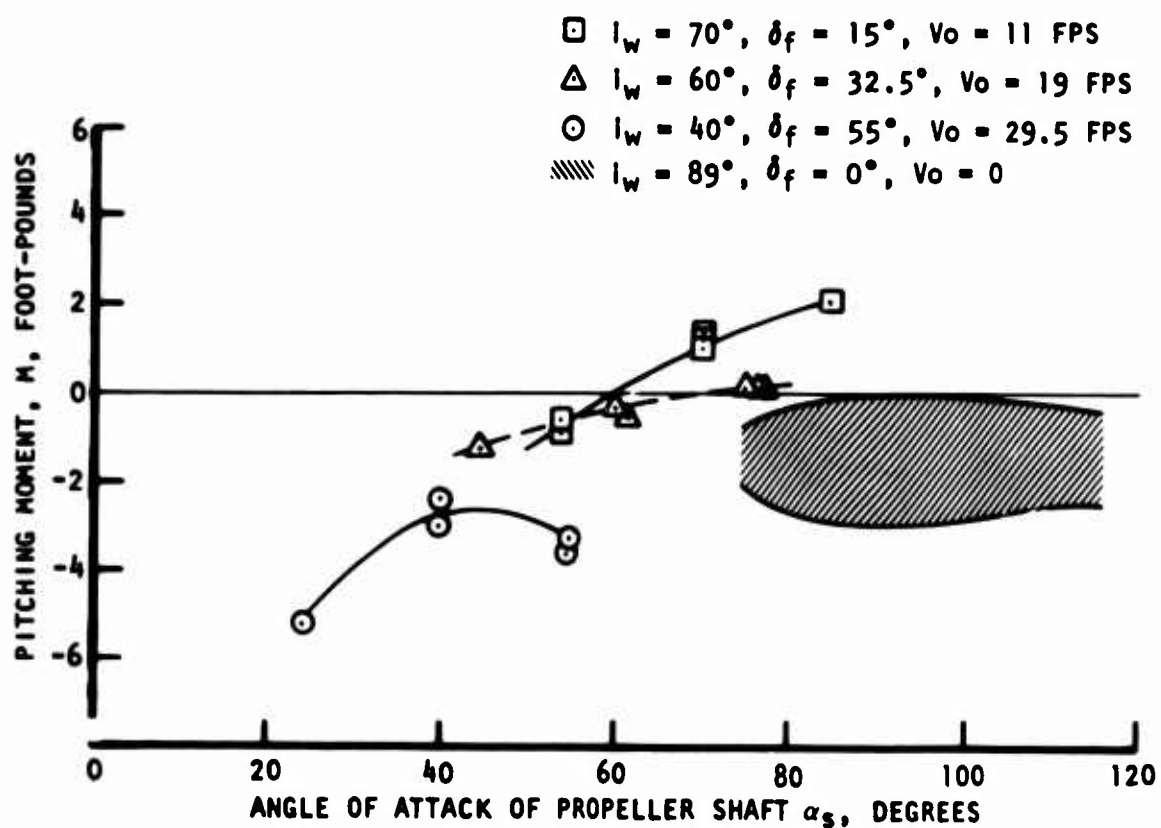


Figure 9c. Variation of Model Pitching Moment With Angle of Attack of Propeller Shaft Near Trim Conditions From Static Data. (Tail Rotor Off,  $\beta_{NR} = 17.5^\circ$ ,  $\Omega_{NR} = 4,000 \text{ RPM}$ ,  $i_t$  Shown in Figure 6)

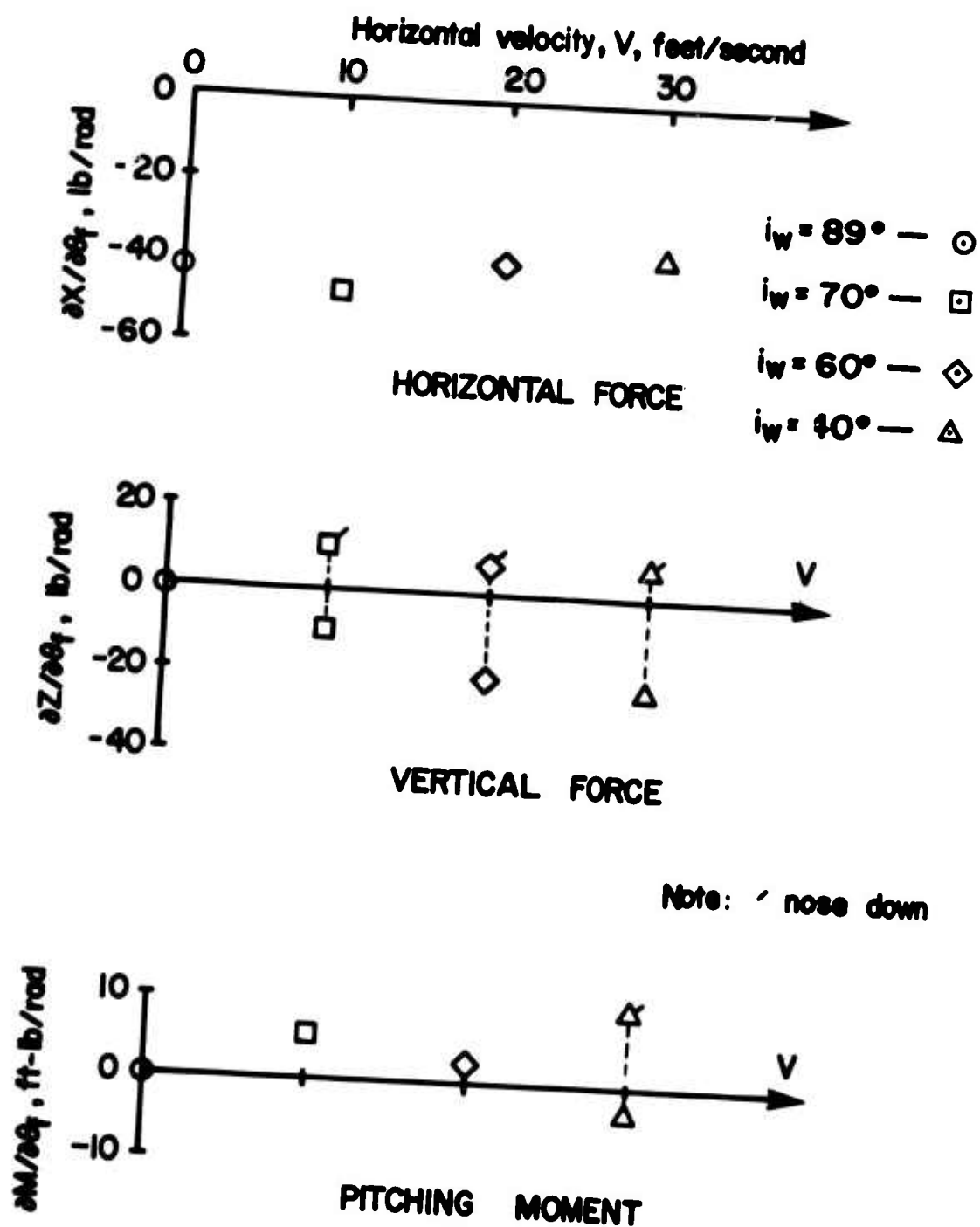


Figure 10a. Rate of Change of Forces and Pitching Moment With Fuselage Pitch Angle ( $\sim$  Angle of Attack) From Static Data. (Tail Rotor Off,  $\beta_{MR} = 17.5^\circ$ ,  $\Omega_{MR} = 4,000$  RPM,  $\delta_f$  and  $i_t$  Shown in Figure 6)

RATE OF CHANGE OF VERTICAL FORCE WITH  
HORIZONTAL VELOCITY,  $\partial Z/\partial u$ , LB/FT/SEC

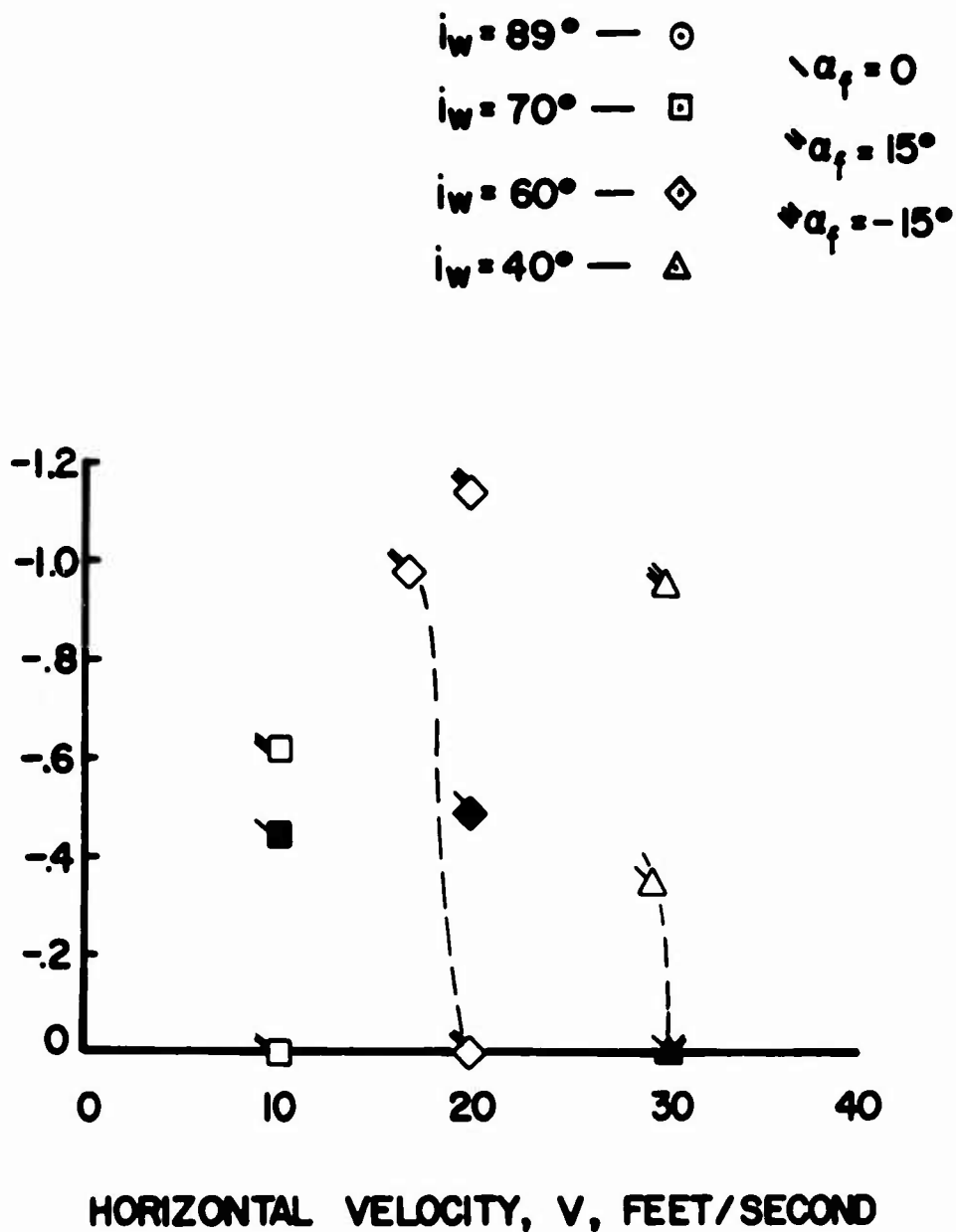


Figure 10b. Rate of Change of Vertical Force With Horizontal Velocity Versus Horizontal Velocity From Static Data.  
(Tail Rotor Off,  $\beta_{MR} = 17.5^\circ$ ,  $\Omega_{MR} = 4,000$  RPM,  
 $\delta_f$  and  $i_t$  Shown in Figure 6)

RATE OF CHANGE OF HORIZONTAL FORCE WITH  
HORIZONTAL VELOCITY,  $\partial X/\partial u$ , LB/FT/SEC

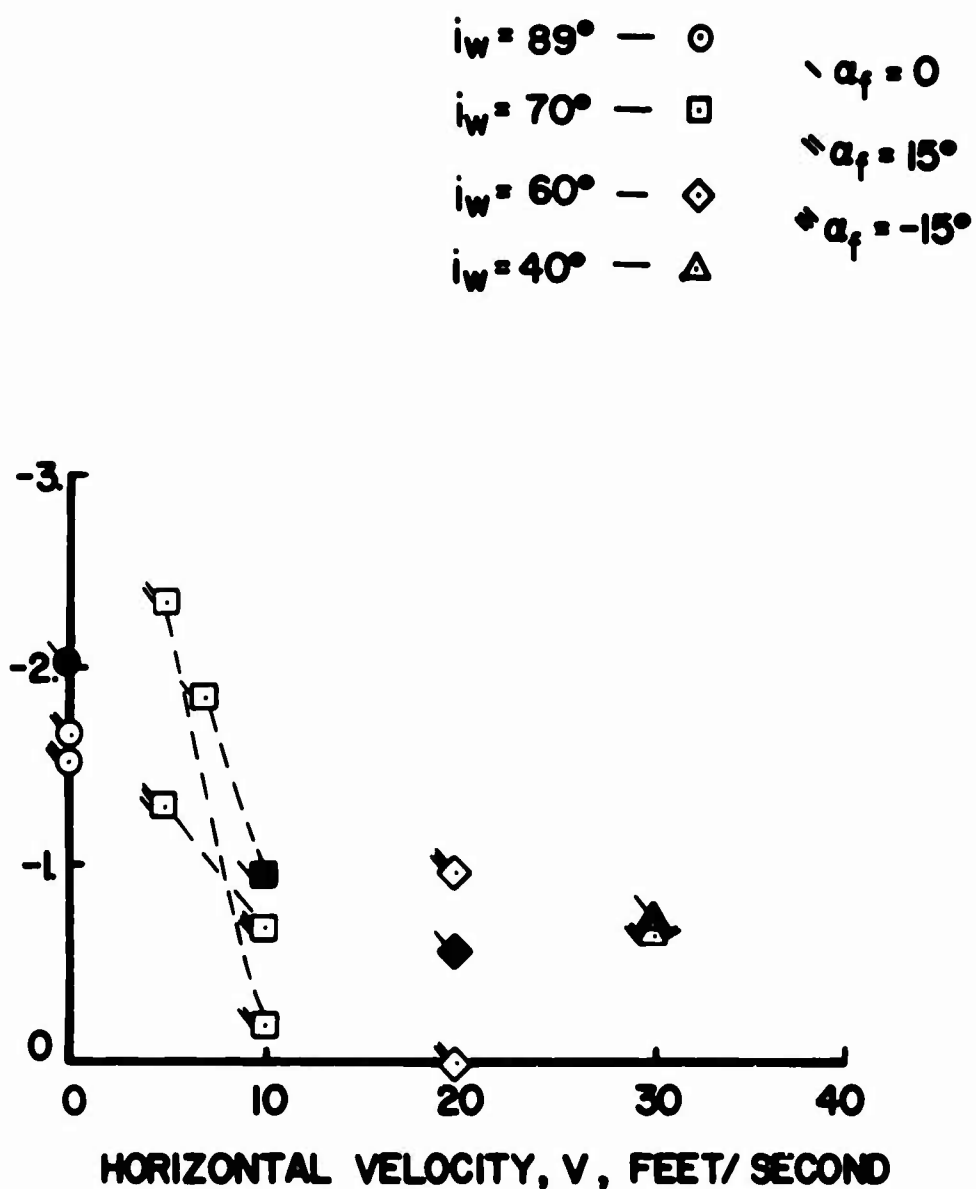


Figure 10c. Rate of Change of Horizontal Force With Horizontal Velocity Versus Horizontal Velocity From Static Data.  
(Tail Rotor Off,  $\beta_{WR} = 17.5^\circ$ ,  $\Omega_{WR} = 4,000$  RPM.  
 $\delta_f$  and  $i_t$  Shown in Figure 6)

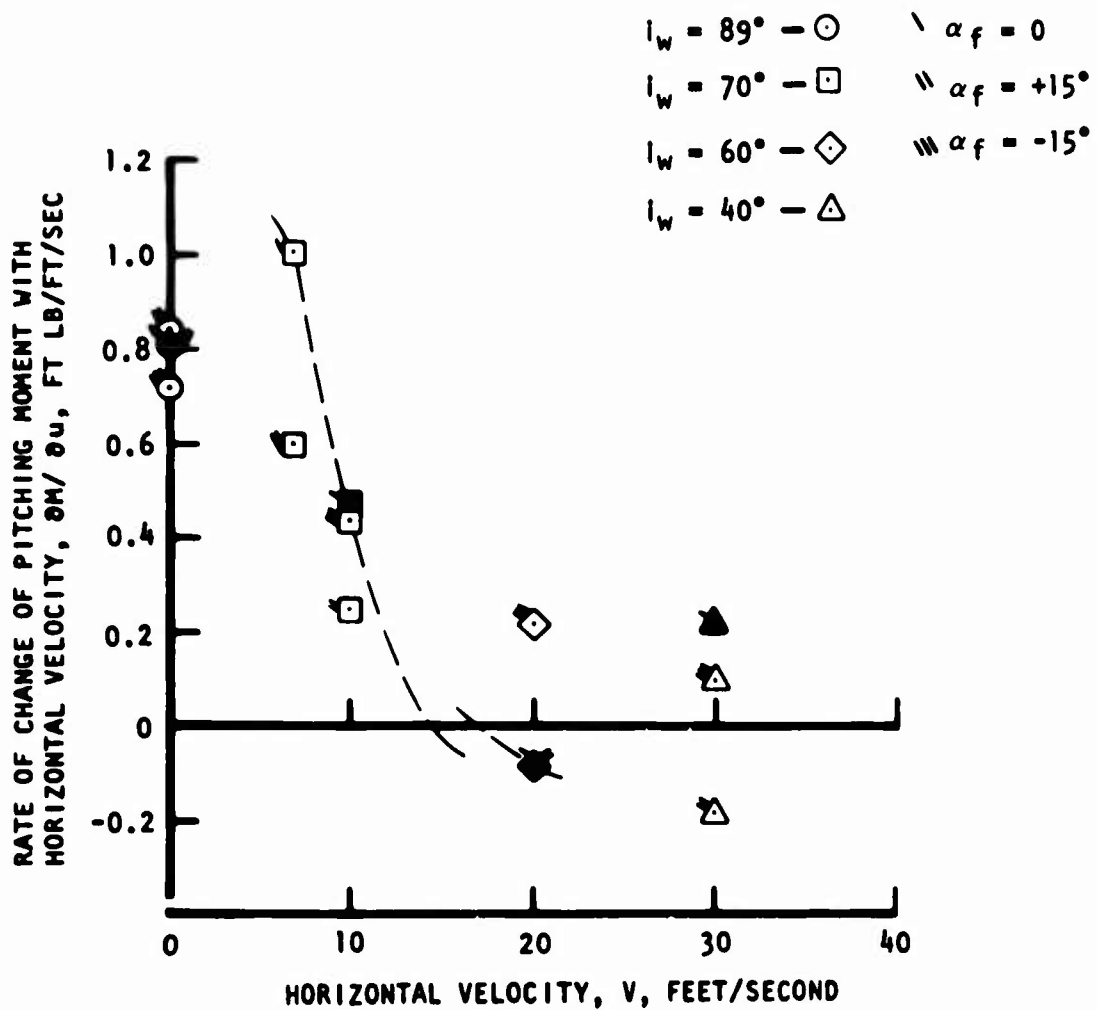
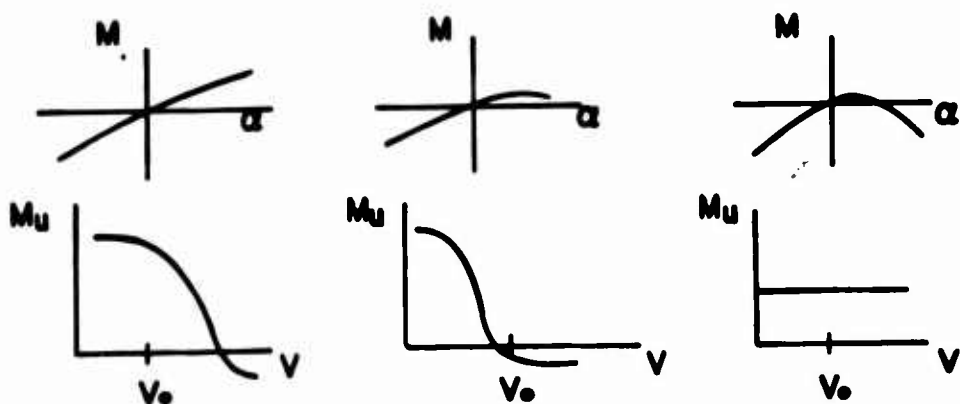
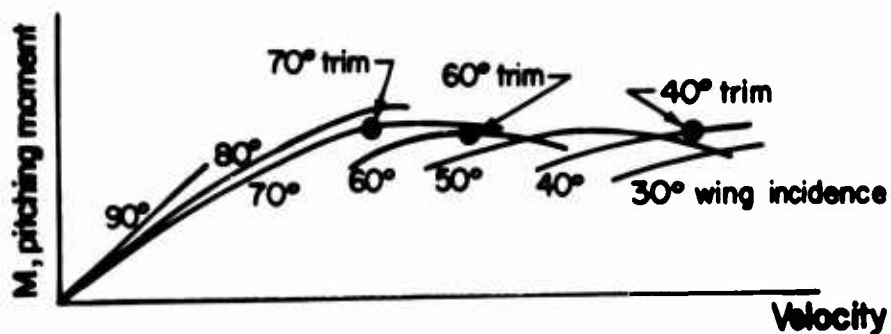


Figure 10d. Rate of Change of Pitching Moment With Horizontal Velocity Versus Horizontal Velocity From Static Data.  
(Tail Rotor Off,  $\beta_{NR} = 17.5^\circ$ ,  $\Omega_{NR} = 4,000$  RPM,  
 $\delta_f$  and  $i_t$  Shown in Figure 6)



General nature of pitching-moment curves (for clarity, effects of flap deflection and trimming are not shown)

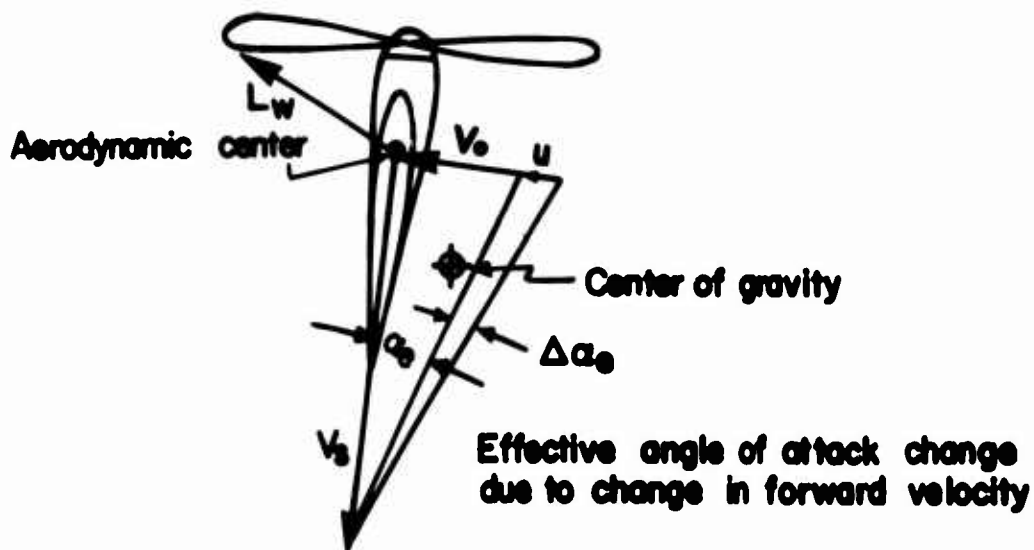


Figure 11. General Nature of Static Stability Derivatives.

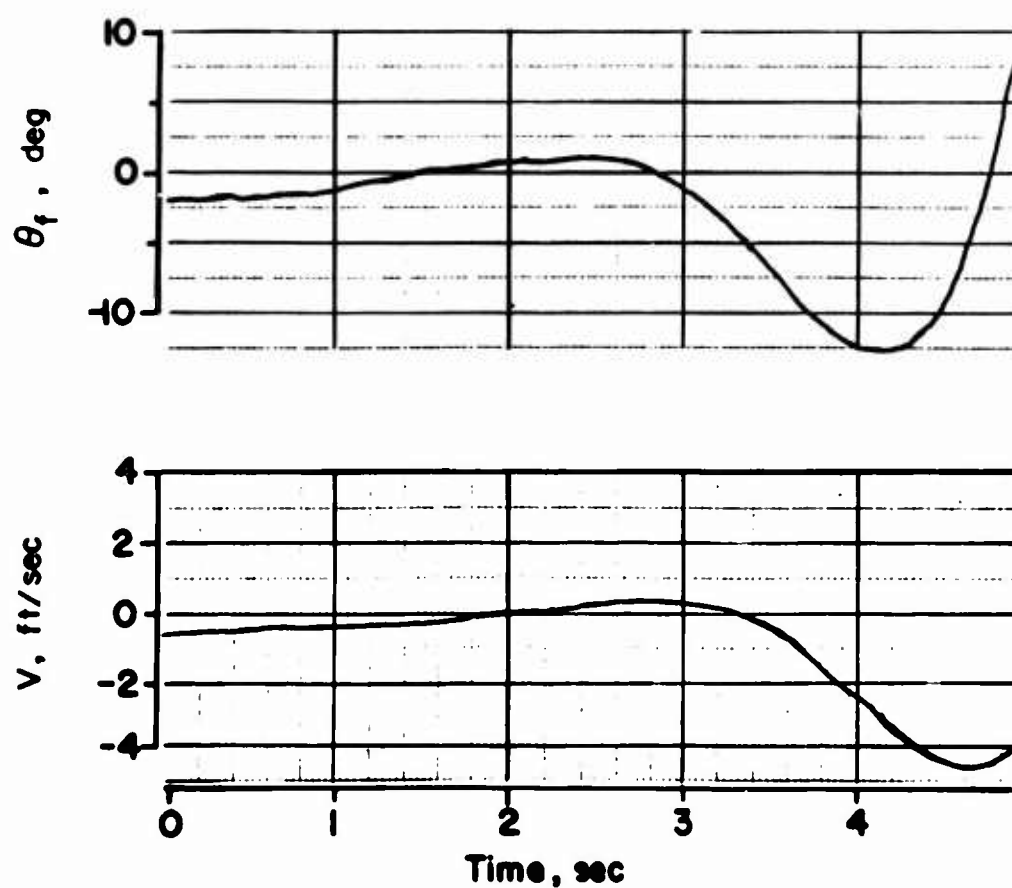


Figure 12. Model Transient Self-Excited Response,  
 $i_w = 89^\circ$ , Two Degrees of Freedom.  
 ( $\Omega_{nn} = 4,000$  RPM,  $\theta_{nn} = 17.4^\circ$ ,  $i_t = 45^\circ$ ,  $\delta_f = 0^\circ$ , 9-Percent C.G.)

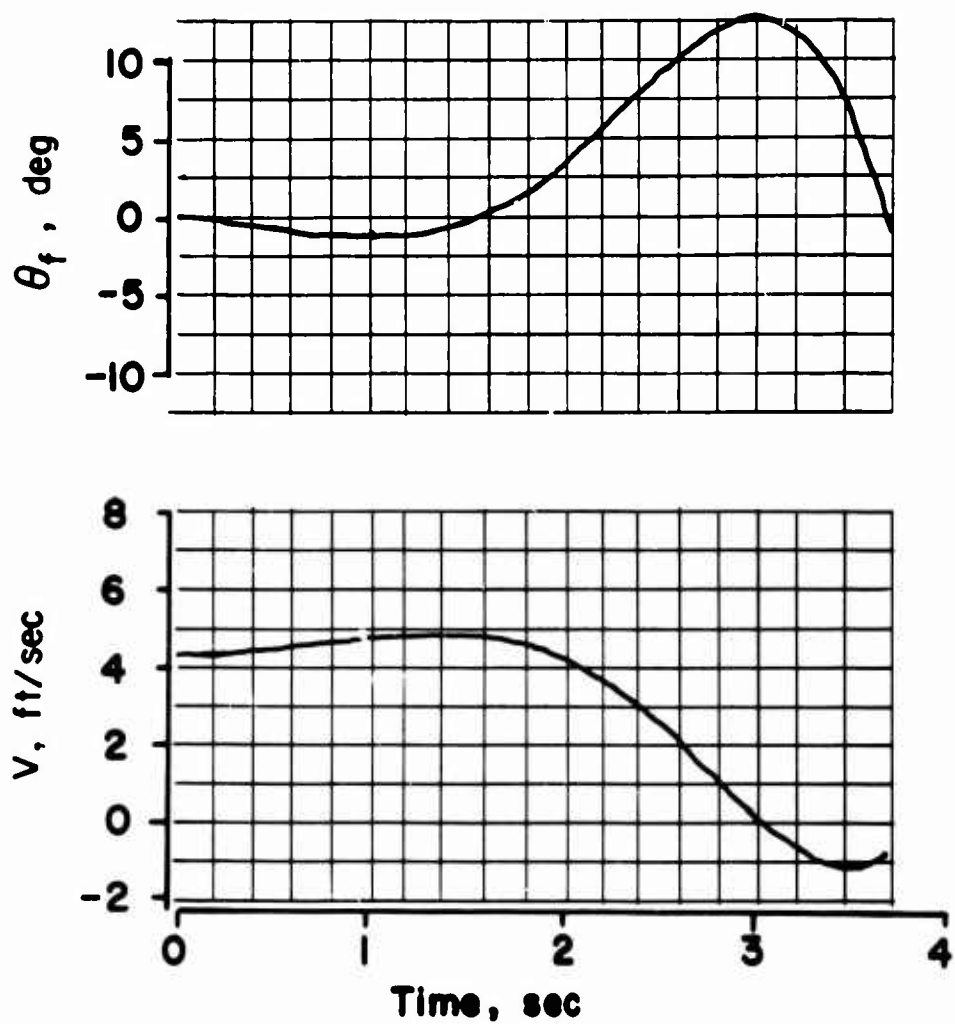


Figure 13. Model Transient Self-Excited Response,  $i_w = 80^\circ$ ,  
Two Degrees of Freedom.  
( $\Omega_{MR} = 4,000$  RPM,  $\theta_{MR} = 17.4^\circ$ ,  $i_t = 50^\circ$ ,  
 $\delta_f = 0^\circ$ , 9-Percent C.G.)



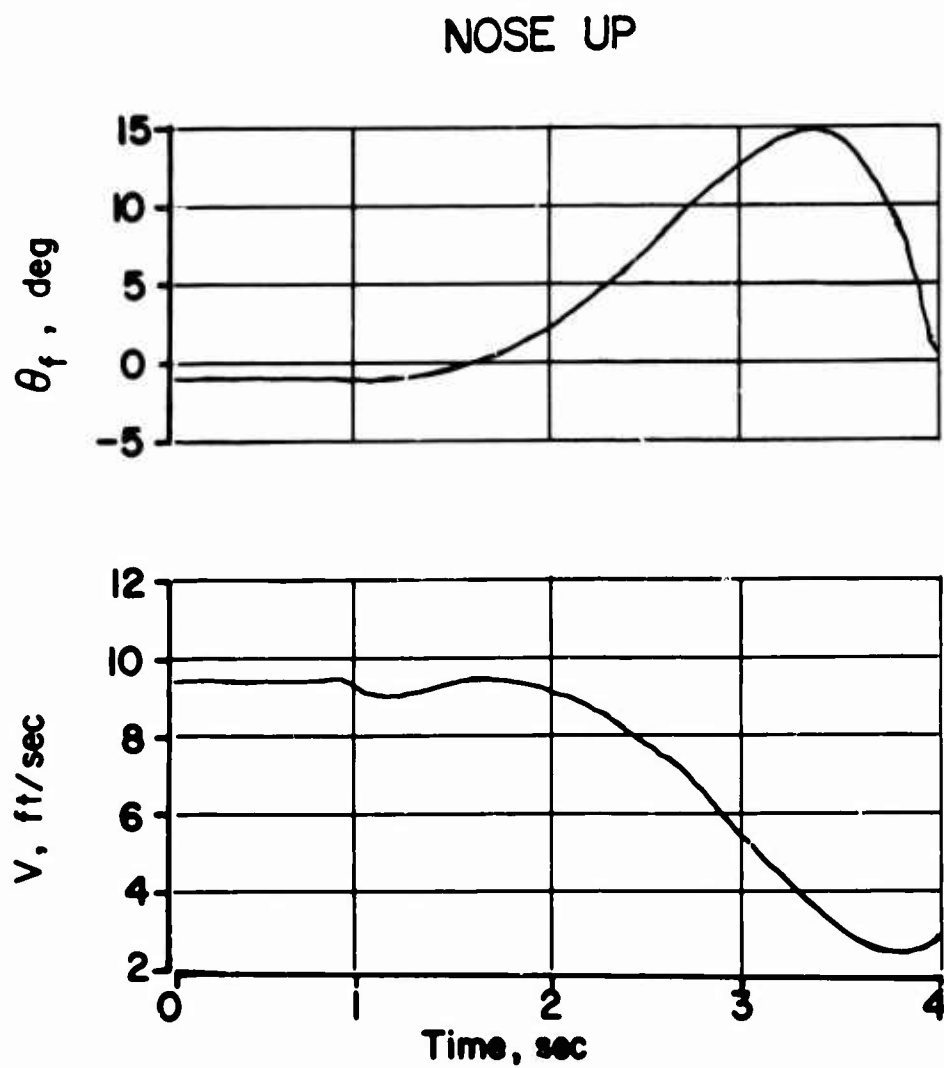


Figure 14a. Model Transient Self-Excited Response,  
 $i_w = 70^\circ$ , Two Degrees of Freedom.  
 ( $\Omega_{MR} = 4,000$  RPM,  $\beta_{MR} = 17.4^\circ$ ,  $i_t = 50^\circ$ ,  
 $\delta_f = 15^\circ$ , 9-Percent C.G.)

# NOSE DOWN

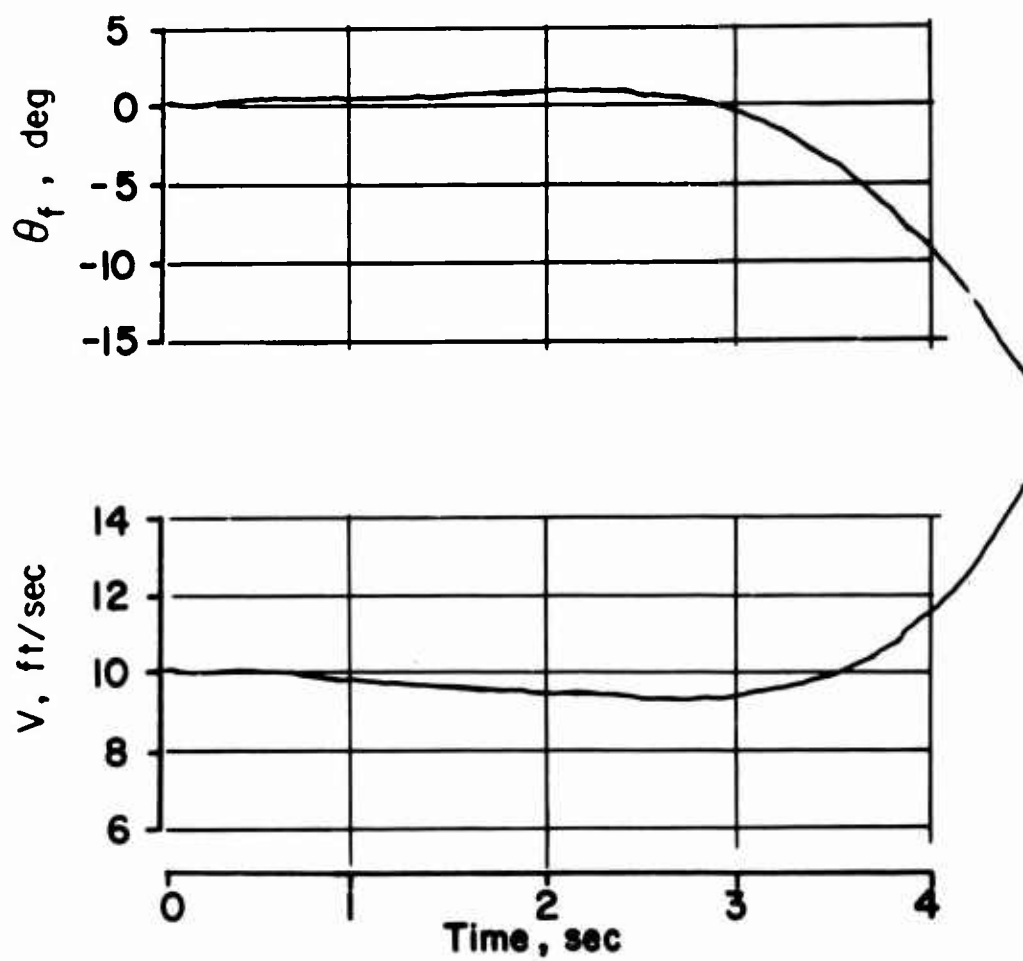


Figure 14b. Model Transient Self-Excited Response,  
 $i_w = 70^\circ$ , Two Degrees of Freedom.  
 $(\Omega_{MR} = 4,000 \text{ RPM}, \beta_{MR} = 17.4^\circ, i_t = 50^\circ,$   
 $\delta_f = 15^\circ, 9\text{-Percent C.G.})$

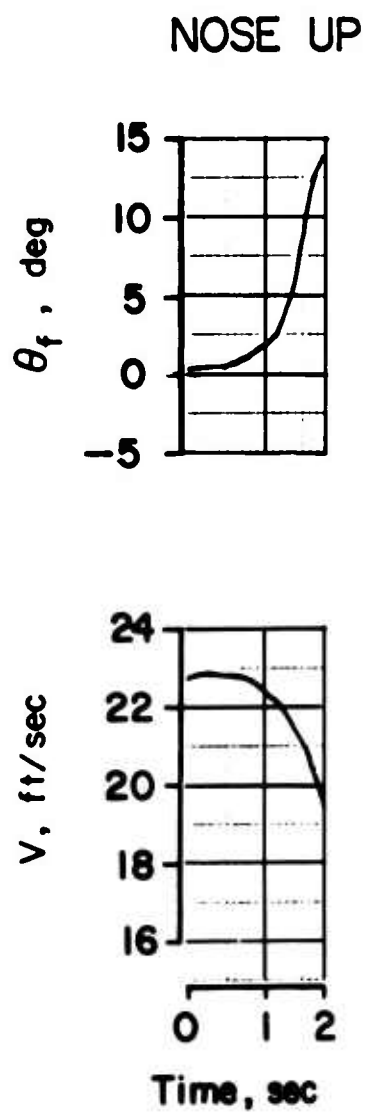


Figure 15a. Model Transient Self-Excited Response,  
 $i_w = 60^\circ$ , Two Degrees of Freedom.  
 ( $\Omega_{MR} = 4,000$  RPM,  $\alpha_{MR} = 17.4^\circ$ ,  $i_t = 30^\circ$ ,  
 $\delta_f = 32.5^\circ$ , 9-Percent C.G.)

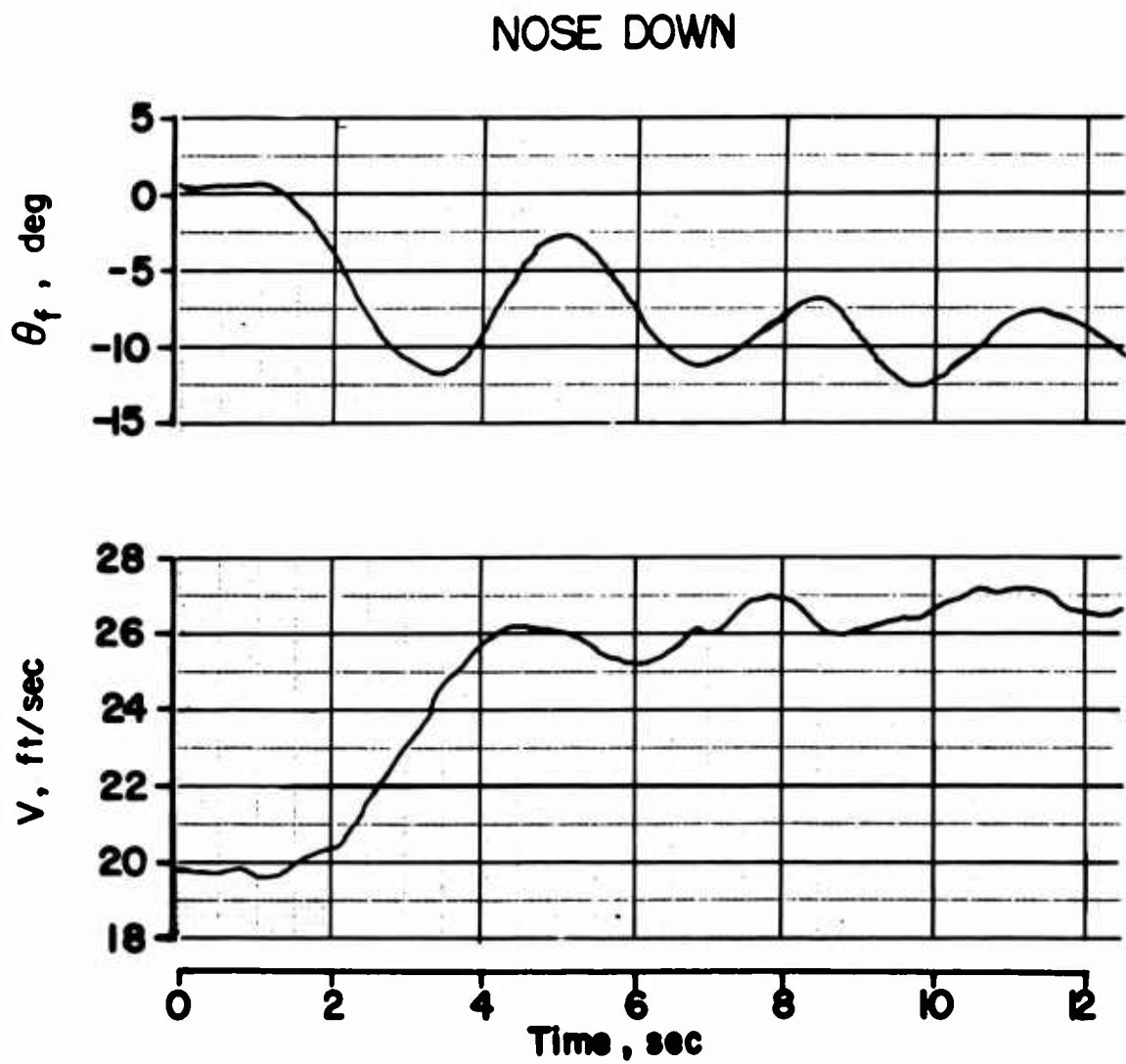


Figure 15b. Model Transient Self-Excited Response,  
 $i_w = 60^\circ$ , Two Degrees of Freedom.  
 ( $\Omega_{MR} = 4,000$  RPM,  $\beta_{MR} = 17.4^\circ$ ,  $i_t = 30^\circ$ ,  
 $\delta_f = 32.5^\circ$ , 9-Percent C.G.)

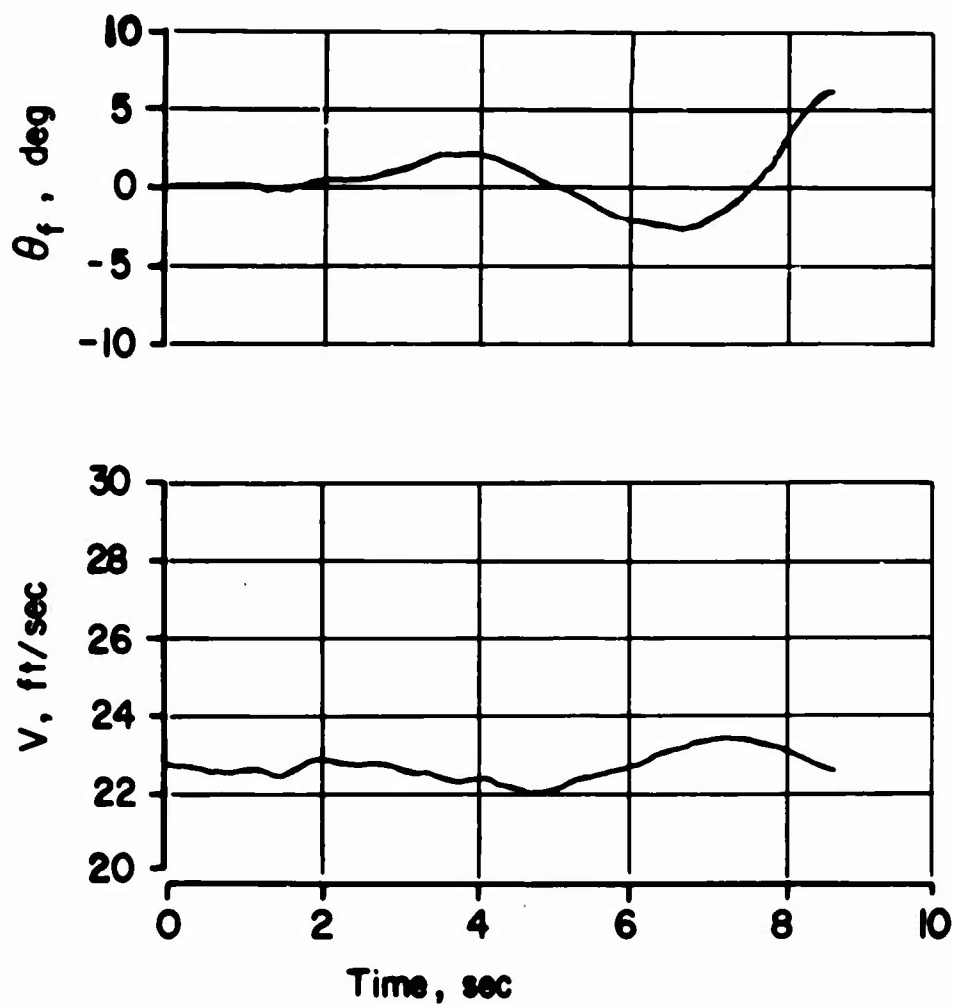


Figure 16a. Model Transient Self-Excited Response,  
 $i_w = 50^\circ$ , Two Degrees of Freedom, Small Amplitude Motion.  
 ( $\Omega_{MR} = 4,000$  RPM,  $\beta_{MR} = 14.8^\circ$ ,  $i_t = 0^\circ$ ,  
 $\delta_r = 50^\circ$ , 9-Percent C.G.)

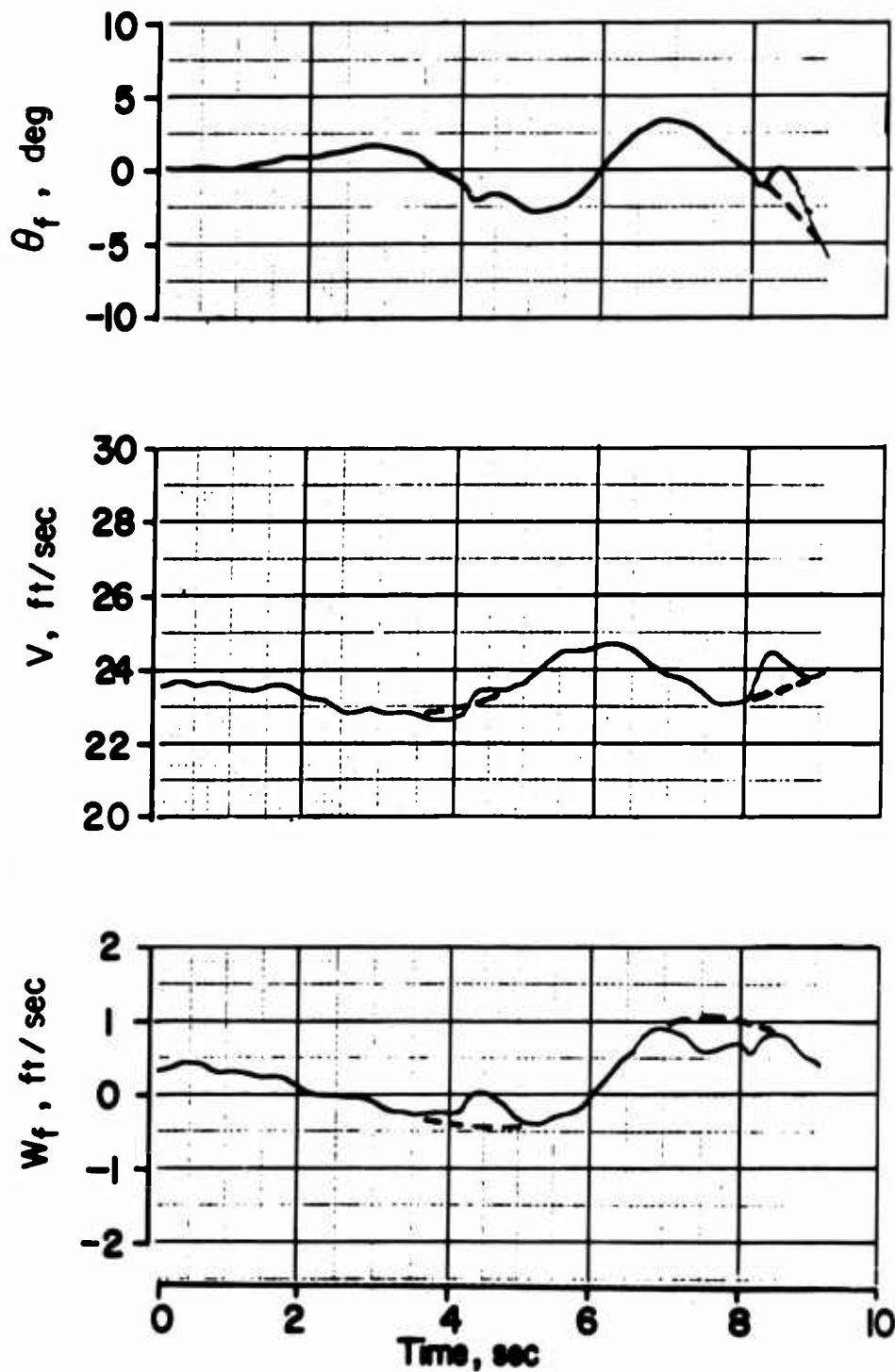


Figure 16b. Model Transient Self-Excited Response,  
 $i_w = 50^\circ$ , Three Degrees of Freedom.  
 ( $\Omega_{MR} = 4,000$  RPM,  $\beta_{MR} = 14.8^\circ$ ,  $i_t = 0^\circ$ ,  
 $\delta_f = 50^\circ$ , 9-Percent C.G.)

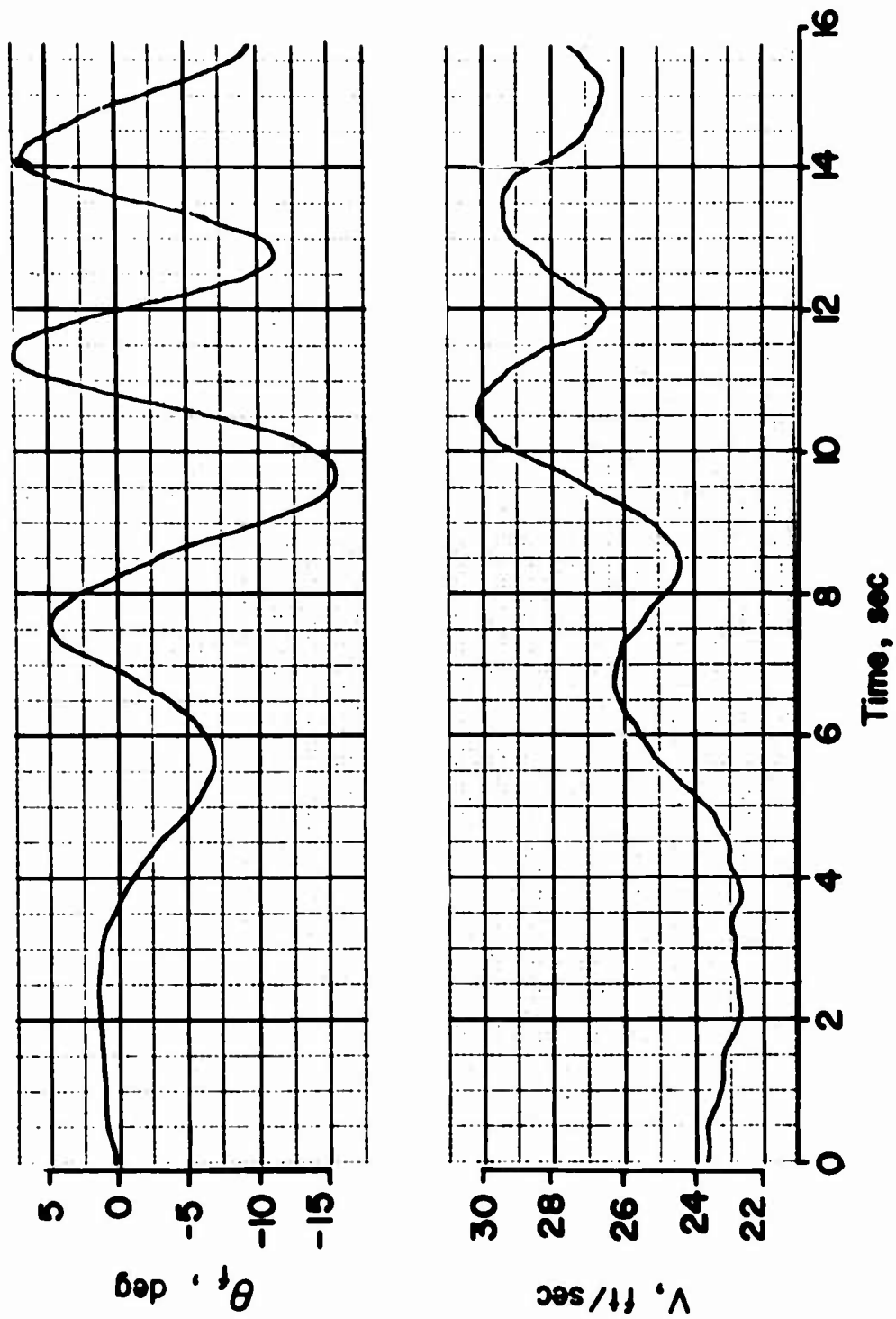


Figure 16c. Model Transient Self-Excited Response,  $i_w = 50^\circ$ , Two Degrees of Freedom, Large Amplitude Motion.  
 $(\Omega_{MR} = 4,000 \text{ RPM}, \beta_{MR} = 14.8^\circ, i_t = 0^\circ, \delta f = 50^\circ, 9\text{-Percent C.G.})$

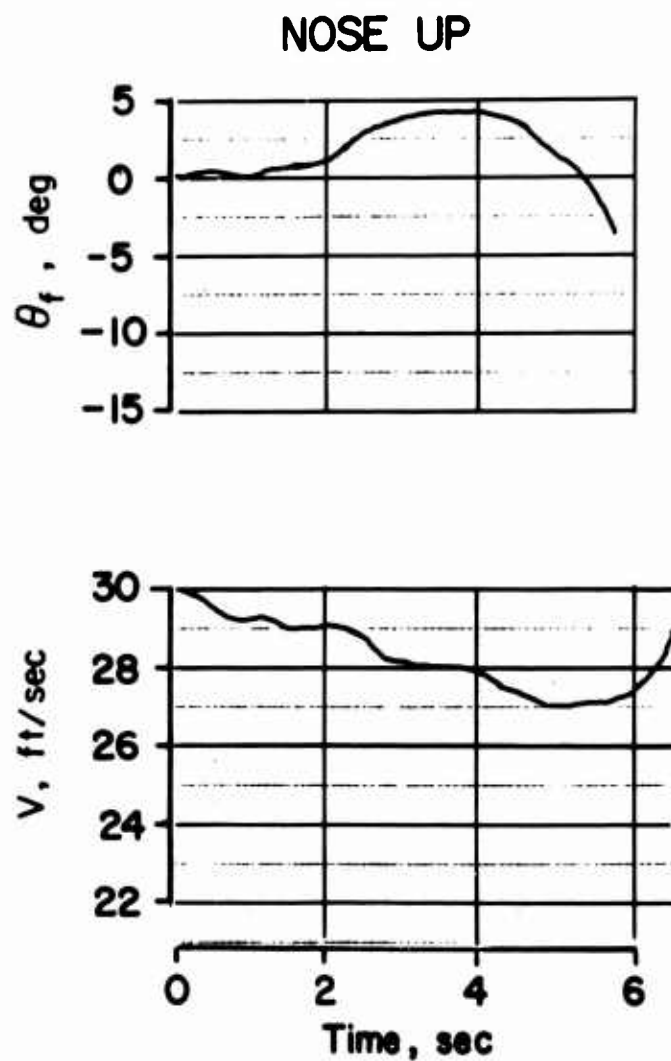


Figure 17a. Model Transient Self-Excited Response,  
 $i_w = 40^\circ$ , Two Degrees of Freedom.  
 ( $\Omega_{MR} = 4,000$  RPM,  $\beta_{MR} = 14.3^\circ$ ,  $i_t = 0^\circ$   
 $\delta_f = 55^\circ$ , 9-Percent C.G.)



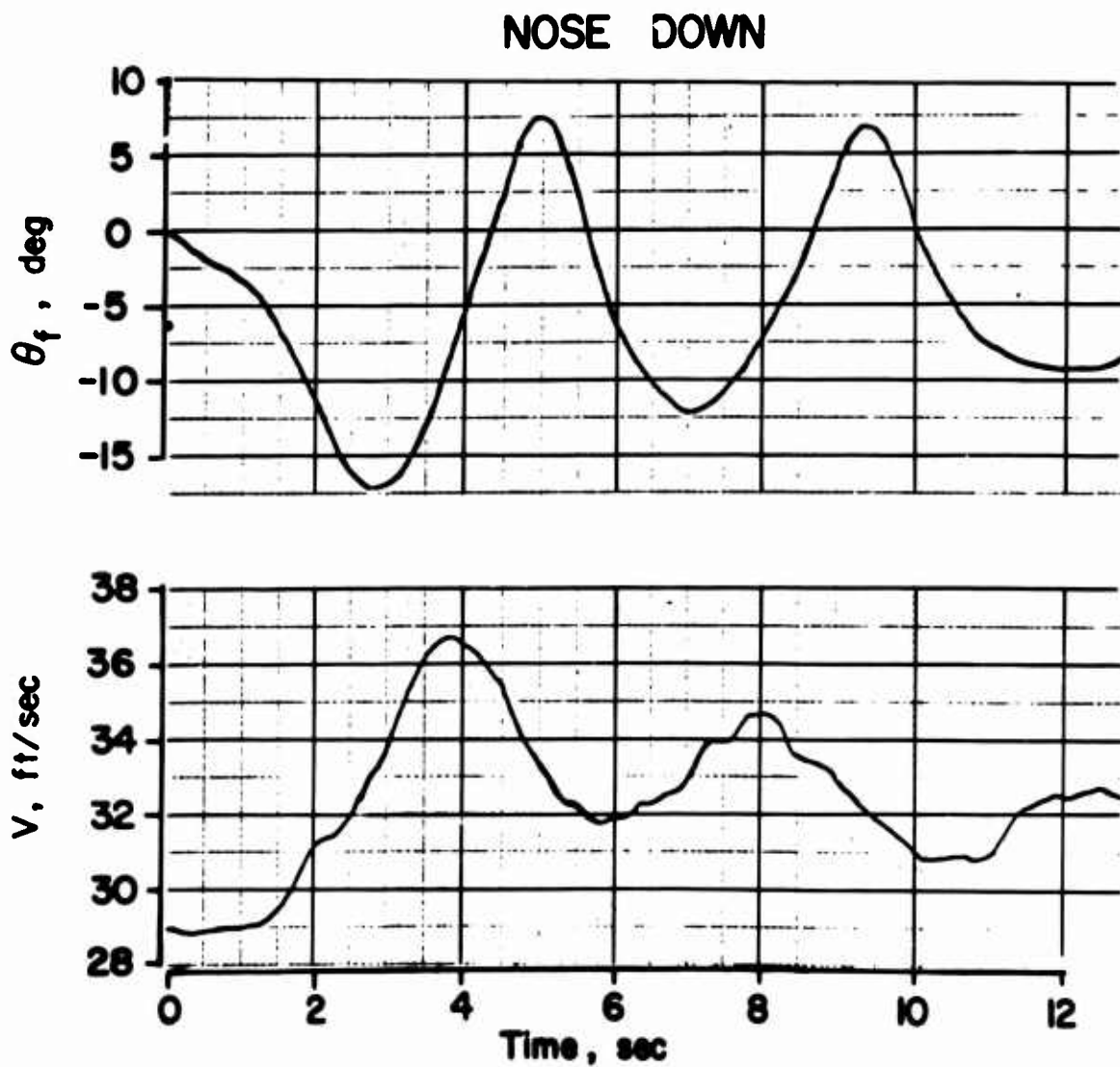


Figure 17b. Model Transient Self-Excited Response,  
 $i_w = 40^\circ$ , Two Degrees of Freedom.  
 ( $\Omega_{mr} = 4,000$  RPM,  $\beta_{mr} = 14.3^\circ$ ,  $i_t = 0^\circ$   
 $\delta_f = 55^\circ$ , 9-Percent C.G.)

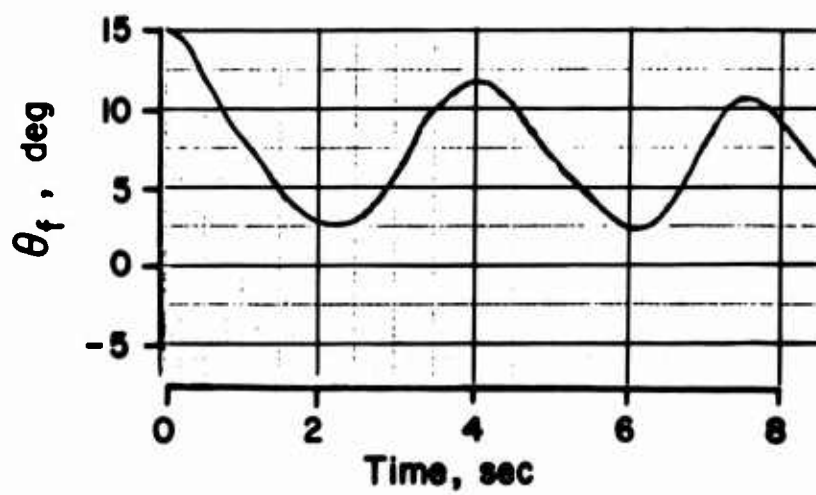
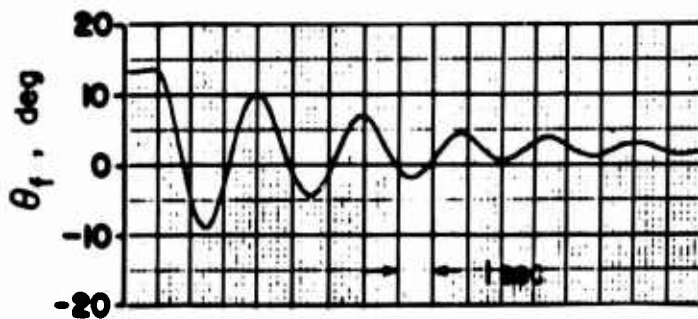


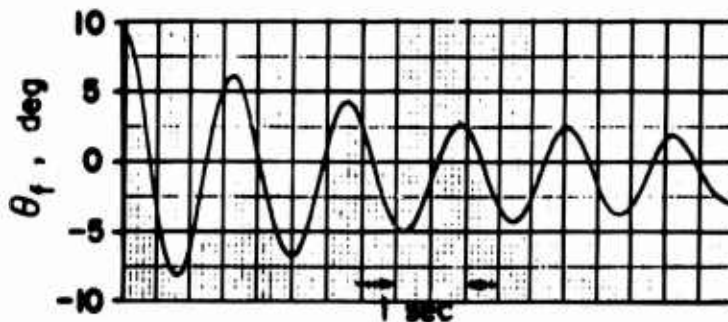
Figure 17c. Model Transient Self-Excited Response,  
 $i_w = 40^\circ$ , One Degree of Freedom,  $V_o = 29$  fps.  
 ( $\Omega_{MR} = 4,000$  RPM,  $\theta_{MR} = 14.3^\circ$ ,  $i_t = 0^\circ$ ,  
 $\delta_f = 55^\circ$ , 9-Percent C.G.)

EQUATION OF MOTION:

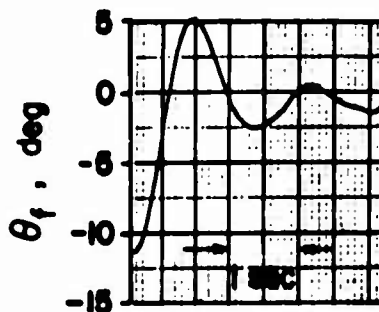
$$I_Y \ddot{\theta}_t - \left[ \frac{\partial M}{\partial \theta} + \frac{\partial M}{\partial \alpha} \right] \dot{\theta}_t + \left[ K_\theta - \frac{\partial M}{\partial \alpha} \right] \theta_t = 0$$



$i_w = 89^\circ$ ,  $\Omega_{MR} = 4000$  RPM,  $\beta_{MR} = 17.4^\circ$ , Tail rotor on,  $V = 0$

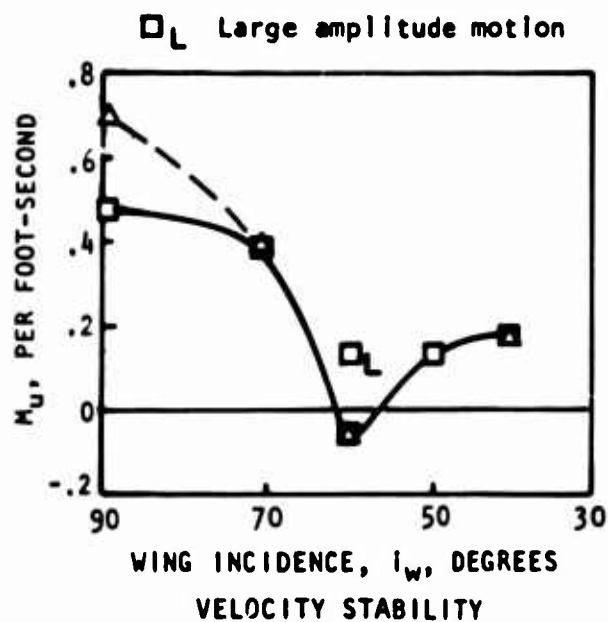


$i_w = 60^\circ$ ,  $\Omega_{MR} = 4000$  RPM,  $\beta_{MR} = 16.6^\circ$ , Tail rotor off,  $V = 20$  fps



$i_w = 40^\circ$ ,  $\Omega_{MR} = 4000$  RPM,  $\beta_{MR} = 16.6^\circ$ , Tail rotor off,  $V = 30$  fps

Figure 18. Model Single-Degree-of-Freedom Runs With Springs.  
(9-Percent C.G.,  $\delta_f$  and  $i_t$  Shown in Figure 6)



- $\Delta$  Static data, without tail rotor,  $\beta_{MR} = 17.4^\circ$   
 $\square$  Analog matching, with tail rotor,  $\beta_{MR} = 17.4^\circ$ ,  $i_w = 89^\circ$ ,  $70^\circ$ ,  $60^\circ$   
 $\beta_{MR} = 14.8^\circ$ ,  $i_w = 50^\circ$   
 $\beta_{MR} = 14.3^\circ$ ,  $i_w = 40^\circ$

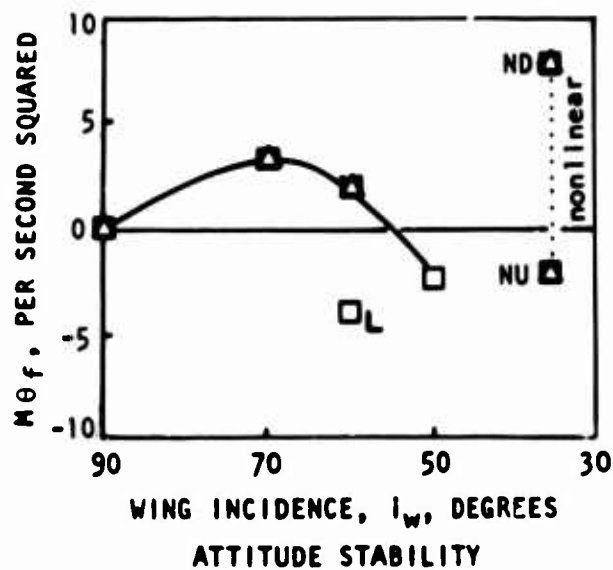


Figure 19a. Comparison of Model Static and Analog-Matching Data. ( $\Omega_{MR} = 4,000$  RPM, 9-Percent C.G.,  $\delta_f$  and  $i_t$  Shown in Figure 6)

- $\Delta$  Single-degree-of-freedom data (see Figure 18)
- $\square$  Analog matching (see Figure 19a)
- $\square_L$  Large amplitude motion

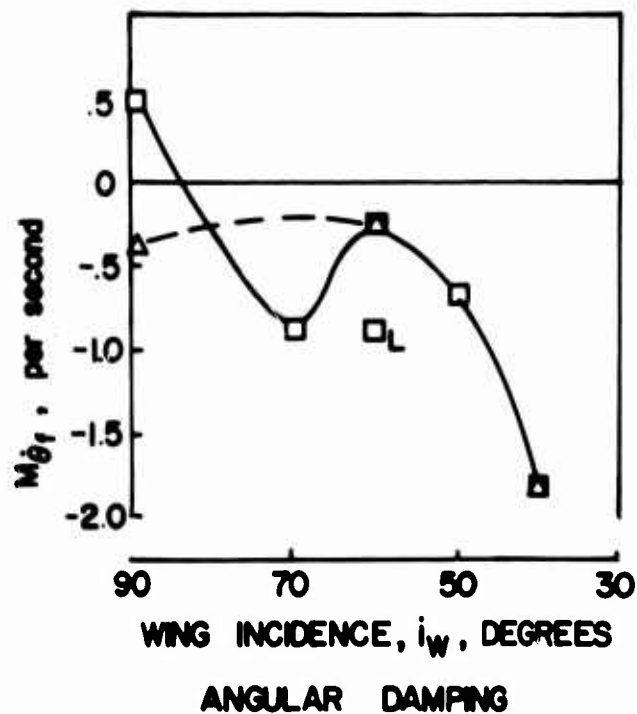
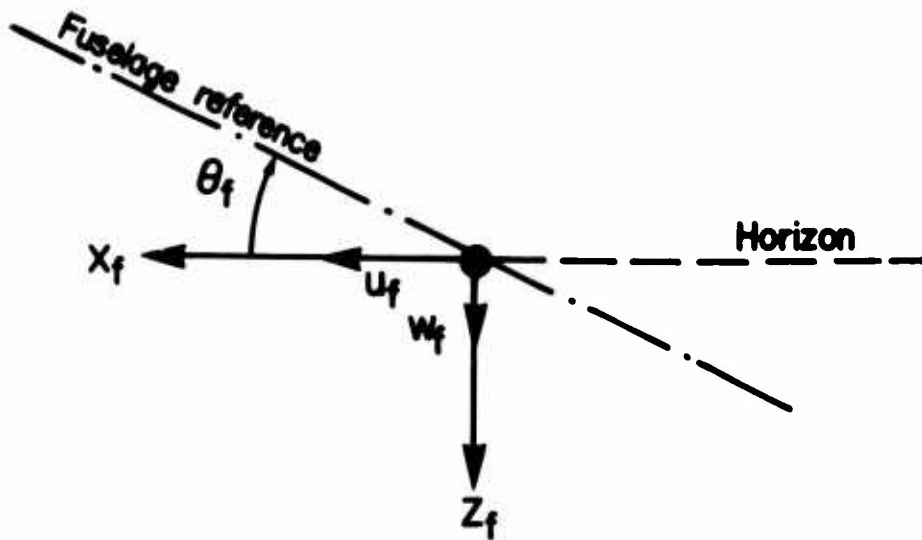
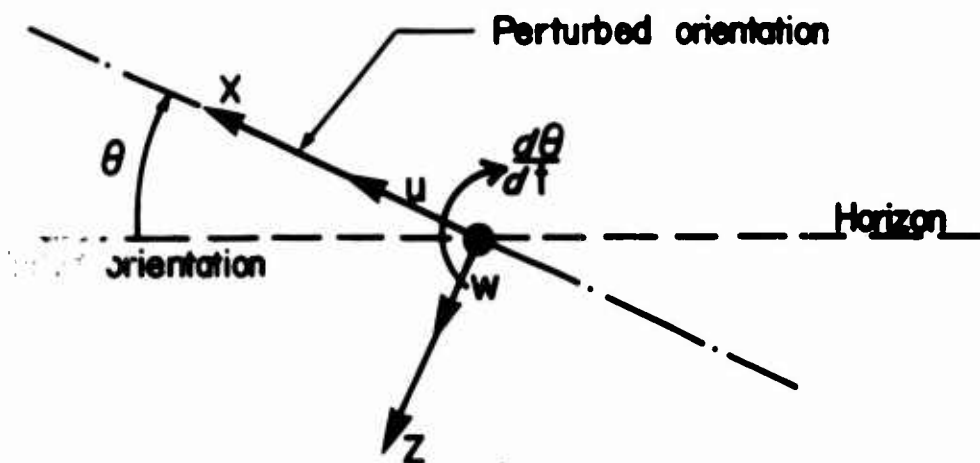


Figure 19b. Comparison of Model Single-Degree-of-Freedom and Analog-Matching Data.  
 $(\Omega_{aa} = 4,000 \text{ RPM}, 9\text{-Percent C.G.}, \delta_f \text{ and } i_t \text{ Shown in Figure 6})$



### SPACE - FIXED AXIS



### STABILITY AXIS

(body fixed, initially aligned with freestream velocity at forward speeds, with horizon in hover)

Figure 20. Axis Systems.

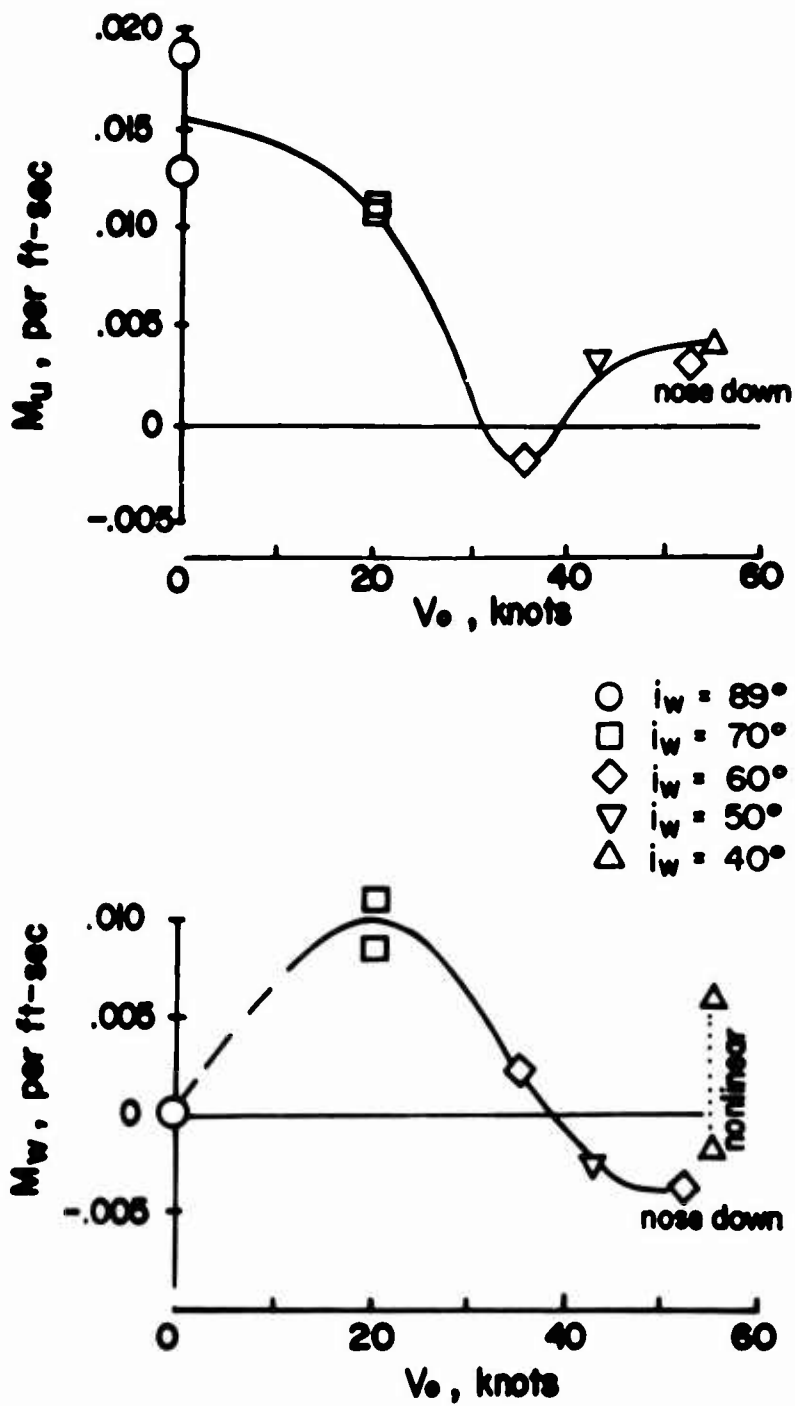


Figure 21a. Full-Scale Stability Derivatives for Altitude/Gross Weight Correspondence Given in Figure 22. (9-Percent C.G.,  $k_y = 10.3$  ft,  $\delta_f$  and  $i_t$  Shown in Figure 6, See Table III for Scaling)

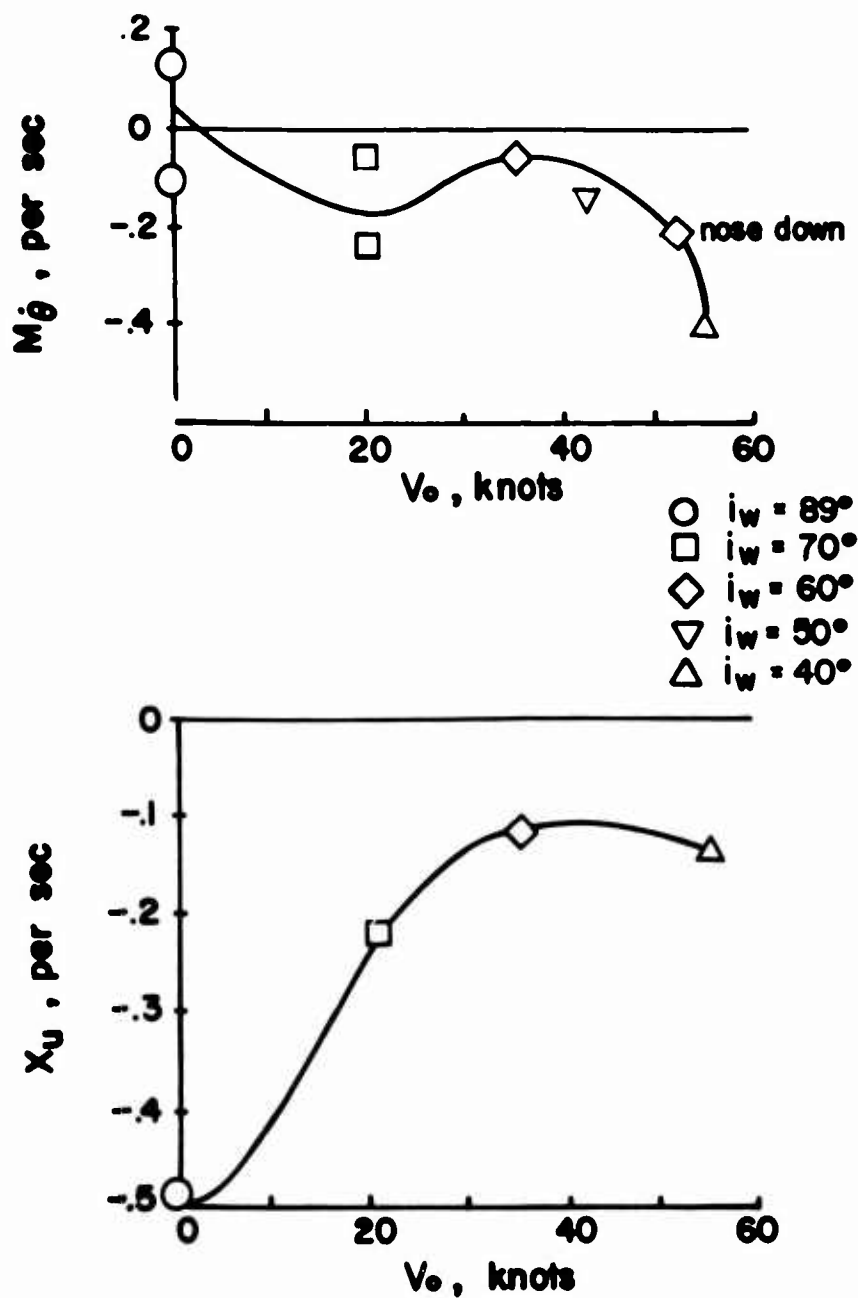


Figure 21b. Full-Scale Stability Derivatives for Altitude/Gross Weight Correspondence Given in Figure 22. (9-Percent C. G.,  $k_y = 10.3$  ft,  $\delta_f$  and  $i_t$  Shown in Figure 6, See Table III for Scaling)



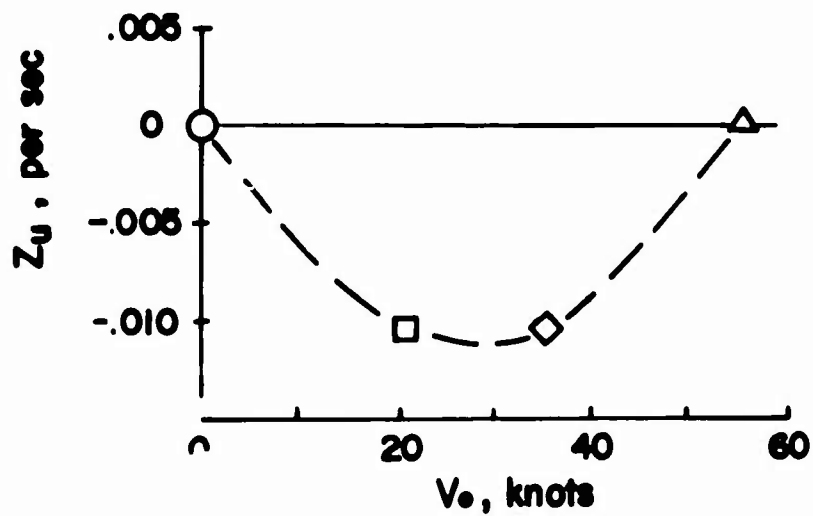
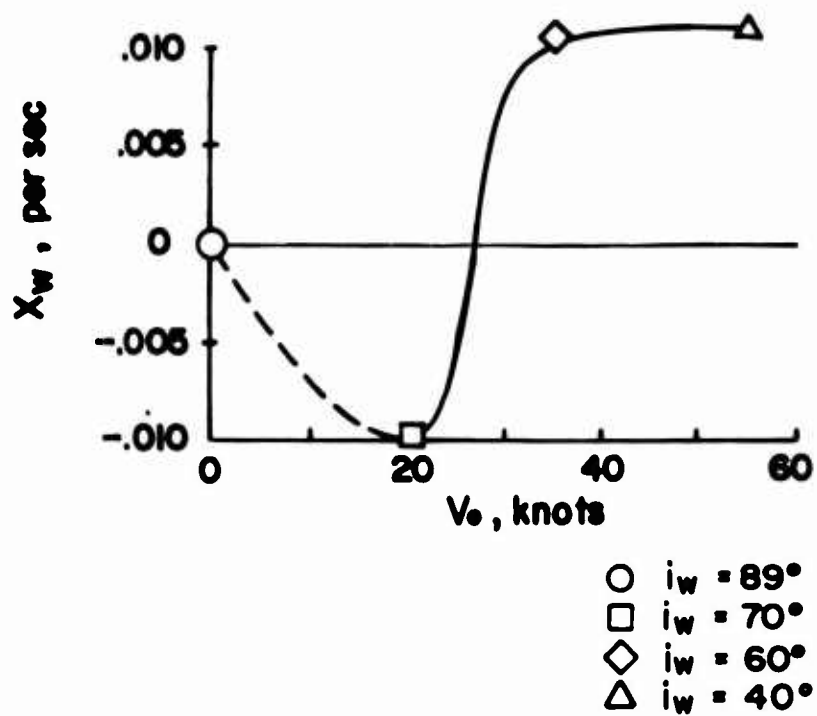


Figure 21c. Full-Scale Stability Derivatives for Altitude/Gross Weight Correspondence Given in Figure 22. (9-Percent C.G.,  $k_y = 10.3$  ft,  $\delta_f$  and  $i_t$  Shown in Figure 6, See Table III for Scaling)

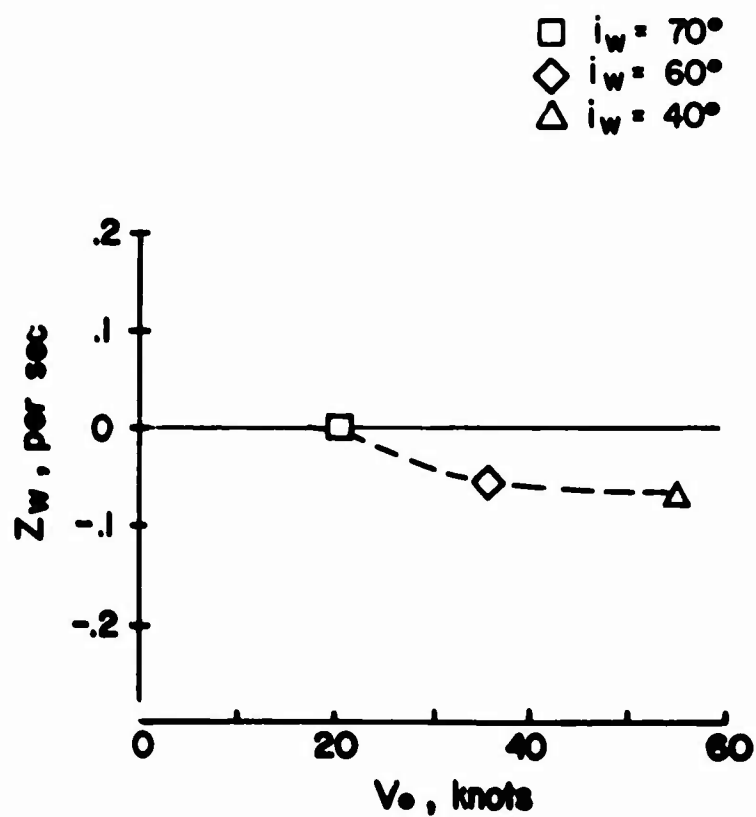


Figure 21d. Full-Scale Stability Derivatives for Altitude/Gross Weight Correspondence Given in Figure 22.  
(9-Percent C. G. ,  $k_y = 10.3$  ft,  $\delta_f$  and  $i_t$  Shown in Figure 6, See Table III for Scaling)

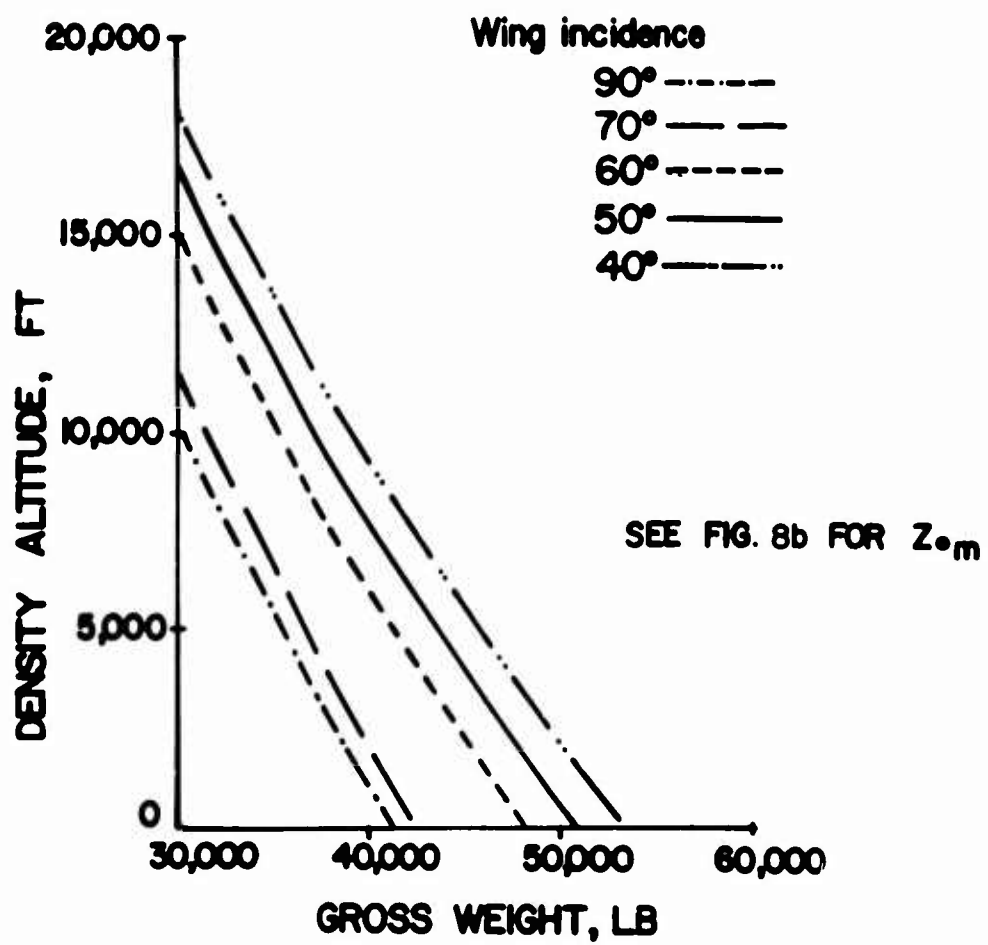


Figure 22. Density Altitude/Gross Weight Correspondence for Stability Derivatives.

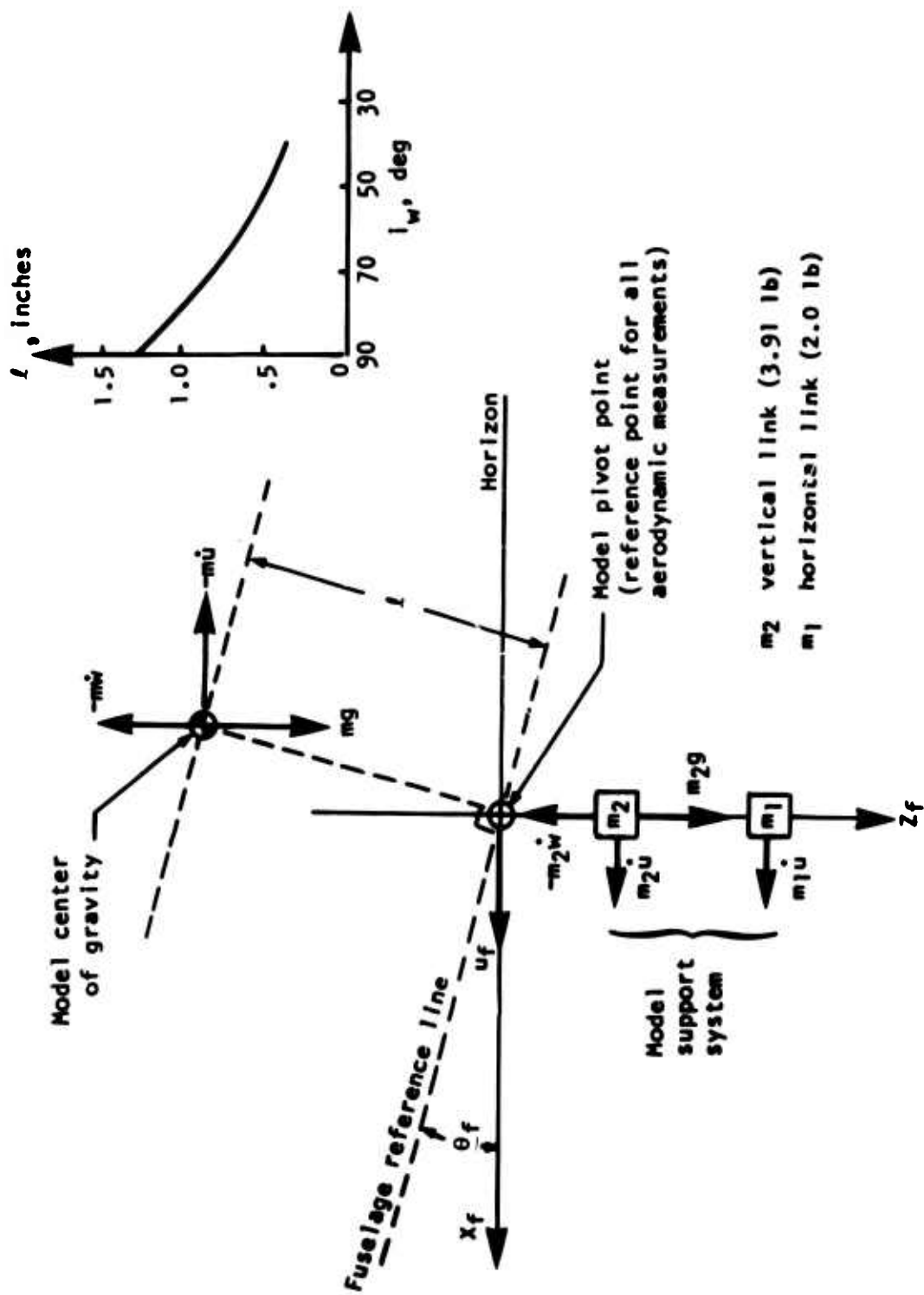


Figure 23. Space-Fixed Axis System.

Unclassified

Security Classification

DOCUMENT CONTROL DATA - R&D		
(Security classification of title, body of abstract and indexing annotation must be entered when the overall report is classified)		
1 ORIGINATING ACTIVITY (Corporate author)		2a REPORT SECURITY CLASSIFICATION
Department of Aerospace and Mechanical Sciences Princeton University		Unclassified
		2b GROUP
3 REPORT TITLE		
An Experimental Investigation of the Longitudinal Dynamic Stability Characteristics of a Four-Propeller Tilt-Wing VTOL Model		
4 DESCRIPTIVE NOTES (Type of report and inclusive dates)		
5 AUTHOR(S) (Last name, first name, initial)		
Curtiss, H. C., Jr. Putman, W. F. Lebacqz, J. V.		
6 REPORT DATE	7a TOTAL NO OF PAGES	7b NO OF REFS
September 1967	123	19
8a CONTRACT OR GRANT NO	9a ORIGINATOR'S REPORT NUMBER(S)	
DA 44-177-AMC-8(T)	USAAVLABS Technical Report 66-80	
8b PROJECT NO	9b OTHER REPORT NO(S) (Any other numbers that may be assigned this report)	
1PI25901A14233	Princeton Univ. Aero. & Mech. Sci. Report Number 774	
10 AVAILABILITY / LIMITATION NOTICES		
Distribution of this document is unlimited.		
11 SUPPLEMENTARY NOTES		12 SPONSORING MILITARY ACTIVITY
		U.S. Army Aviation Materiel Laboratories Fort Eustis, Virginia
13 ABSTRACT		
<p>The results of experiments conducted to evaluate the longitudinal stability characteristics of a 1/10 scale dynamic model of a four-propeller tilt-wing VTOL transport are presented and discussed. The Princeton Dynamic Model Track was used to measure the static stability and the transient response of the model at wing incidences from 90° to 40°. The results are interpreted in terms of full-scale aircraft characteristics. All data are presented for a C.G. position of 90% MAC (the most forward C.G. position of the aircraft is 15% MAC) and the horizontal tail and flap program differ from those presently used on the aircraft. The transient motions at wing incidences above 70° were similar and dominated by high speed stability and low angular damping resulting in an unstable oscillation of approximately a 9-second period for the full-scale aircraft. The responses at wing incidences below 70° were more complex due to a rapid decrease in the speed stability from a large positive value above 70° to a negative value at 60°. The values of the speed stability for the aircraft determined by a detailed analysis of the data in the neighborhood of 60° wing incidence differ from those obtained from a preliminary analysis of the data by the LTV Aerospace Corporation. Typically, at wing incidences between 60° and 40° the linearized static stability derivatives <math>M_u</math> and <math>M_\alpha</math> were small, nonlinearities were evident, and the small amplitude linearized motion was dominated by a divergence. At 40° wing incidence, indications were that the dynamic motions were becoming stable.</p>		

DD FORM 1473

Unclassified

Security Classification

14 KEY WORDS	LINK A		LINK B		LINK C	
	ROLE	WT	ROLE	WT	ROLE	WT
Airplanes, VTO  Stability, Longitudinal  Airplanes, Tilt-wing						

**INSTRUCTIONS**

**1. ORIGINATING ACTIVITY:** Enter the name and address of the contractor, subcontractor, grantee, Department of Defense activity or other organization (*corporate author*) issuing the report.

**2a. REPORT SECURITY CLASSIFICATION:** Enter the overall security classification of the report. Indicate whether "Restricted Data" is included. Marking is to be in accordance with appropriate security regulations.

**2b. GROUP:** Automatic downgrading is specified in DoD Directive S200.10 and Armed Forces Industrial Manual. Enter the group number. Also, when applicable, show that optional markings have been used for Group 3 and Group 4 as authorized.

**3. REPORT TITLE:** Enter the complete report title in all capital letters. Titles in all cases should be unclassified. If a meaningful title cannot be selected without classification, show title classification in all capitals in parenthesis immediately following the title.

**4. DESCRIPTIVE NOTES:** If appropriate, enter the type of report, e.g., interim, progress, summary, annual, or final. Give the inclusive dates when a specific reporting period is covered.

**5. AUTHOR(S):** Enter the name(s) of author(s) as shown on or in the report. Enter last name, first name, middle initial. If military, show rank and branch of service. The name of the principal author is an absolute minimum requirement.

**6. REPORT DATE:** Enter the date of the report as day, month, year, or month, year. If more than one date appears on the report, use date of publication.

**7a. TOTAL NUMBER OF PAGES:** The total page count should follow normal pagination procedure, i.e., enter the number of pages containing information.

**7b. NUMBER OF REFERENCES:** Enter the total number of references cited in the report.

**8a. CONTRACT OR GRANT NUMBER:** If appropriate, enter the applicable number of the contract or grant under which the report was written.

**8b, 8c, & 8d. PROJECT NUMBER:** Enter the appropriate military department identification, such as project number, subproject number, system numbers, task number, etc.

**9a. ORIGINATOR'S REPORT NUMBER(S):** Enter the official report number by which the document will be identified and controlled by the originating activity. This number must be unique to this report.

**9b. OTHER REPORT NUMBER(S):** If the report has been assigned any other report numbers (*either by the originator or by the sponsor*), also enter this number(s).

**10. AVAILABILITY/LIMITATION NOTICES:** Enter any limitations on further dissemination of the report, other than those imposed by security classification, using standard statements such as:

(1) "Qualified requesters may obtain copies of this report from DDC."

(2) "Foreign announcement and dissemination of this report by DDC is not authorized."

(3) "U. S. Government agencies may obtain copies of this report directly from DDC. Other qualified DDC users shall request through \_\_\_\_\_."

(4) "U. S. military agencies may obtain copies of this report directly from DDC. Other qualified users shall request through \_\_\_\_\_."

(5) "All distribution of this report is controlled. Qualified DDC users shall request through \_\_\_\_\_."

If the report has been furnished to the Office of Technical Services, Department of Commerce, for sale to the public, indicate this fact and enter the price, if known.

**11. SUPPLEMENTARY NOTES:** Use for additional explanatory notes.

**12. SPONSORING MILITARY ACTIVITY:** Enter the name of the departmental project office or laboratory sponsoring (*paying for*) the research and development. Include address.

**13. ABSTRACT:** Enter an abstract giving a brief and factual summary of the document indicative of the report, even though it may also appear elsewhere in the body of the technical report. If additional space is required, a continuation sheet shall be attached.

It is highly desirable that the abstract of classified reports be unclassified. Each paragraph of the abstract shall end with an indication of the military security classification of the information in the paragraph, represented as (TS), (S), (C), or (U).

There is no limitation on the length of the abstract. However, the suggested length is from 150 to 225 words.

**14. KEY WORDS:** Key words are technically meaningful terms or short phrases that characterize a report and may be used as index entries for cataloging the report. Key words must be selected so that no security classification is required. Identifiers, such as equipment model designation, trade name, military project code name, geographic location, may be used as key words but will be followed by an indication of technical context. The assignment of links, rules, and weights is optional.